



UNIVERSITY OF PISA

Engineering PhD School “Leonardo da Vinci”

PhD Course in

*“Applied Electromagnetism in Electrical and Biomedical Engineering,
Electronics, Smart Sensors, Nano-Technologies”*

PhD Thesis

Adaptive Antennas for Mobile Terminals of Wireless Communication Links

ING/INF-02

Advisors:

Prof. Paolo NEPA

Author:

Andrea BARONI

2016

*Experience is what you get
When you didn't get what you wanted*

Randy Pausch

Contents

Contents.....	1
List of Figures	3
Publications	6
Introduction	8
1 A wearable Self Tuning Network for Emergency Rescue Operations.....	9
1.1 Introduction	9
1.2 Working Environment and General Requirement	10
1.3 State of Art Overview.....	13
1.4 Hardware Description.....	16
1.5 Software Architecture.....	25
1.6 Test and Measurement results	31
1.6.1 System Calibration	31
1.6.2 System Validation	33
1.7 Conclusion.....	38
2 Wearable Active Sierpinski Fractal Antenna for Off-Body Communication	39
2.1 Introduction	39
2.2 Motivations.....	40
2.3 State of Art	41
2.4 Antenna Design	45
2.4.1 Fractal Geometry Design	45
2.4.2 Active Control Circuit.....	48
2.4.3 E-Textile Technology	49
2.5 Measured Result.....	51

2.6	Conclusion.....	55
3	A reconfigurable layout for a self-structuring lifejacket-integrated antenna of a SAR system.....	56
3.1	Introduction	56
3.2	State of art Overview.....	57
3.3	Antenna Design	59
3.4	Simulation Results.....	61
3.5	Conclusion.....	64
4	Smart mAritime saTellite terminal for mUltimedia seRvices and conteNts (SATURN) system .	65
4.1	Introduction	65
4.2	Motivations.....	66
4.3	SATURN Project Outline.....	67
4.4	SATURN Terminal	68
4.4.1	Forward Link Chain (DVB-SH signal reception)	68
4.4.2	Return Link Chain (E-SSA signal Transmission)	69
4.4.3	Test Environment Setup.....	70
4.5	Test Execution.....	73
4.5.1	Radiation Pattern Estimation.....	73
4.5.2	Forward Link Measurement Evaluation.....	74
4.5.3	Return Link Measurement Evaluation	77
4.5.4	SATURN Services Evaluation.....	79
4.6	Conclusion.....	82
	Conclusions	83
	Bibliography	84

List of Figures

Figure 1 - Cospas Sarsat System Overview.....	10
Figure 2 - Measured Reflection Coefficient on the Smith Chart for different movements of the wearer...	12
Figure 3 - Cospas Sarsat Antennas: (a) design proposed in [6] and (b) design proposed in [8].....	13
Figure 4 - Tuning Network: (a) design proposed in [11], (b) design proposed in [13] and (c) design proposed in [15].....	14
Figure 5 - Type of impedance matching circuit: (a) design proposed in [17] and (b) design proposed in [22]	15
Figure 6 - Closed-Loop Self-Tuning Network Concept.	16
Figure 7 - Directional Coupler: (a) the ZFDC-20-5 for the direct wave sensing and (b) the ZFDC-10-5-S for the reflected wave sensing	16
Figure 8 - Internal Section of the MicroController Block.	17
Figure 9 - AD8302 Evaluation Board.....	17
Figure 10 - Functional Block Diagram of the AD8302.....	18
Figure 11 - Output Characteristics of the AD8302: (a) Output Voltage VS Magnitude Ratio and (b) Output Voltage VS Phase Difference.	18
Figure 12 - Arduino UNO Board.....	19
Figure 13 - AD5504 with its Evaluation Board.....	20
Figure 14 - Functional Block Diagram of the AD5504.	20
Figure 15 - Identified double lowpass-upward-L tuning network.	21
Figure 16 - Effect of the variations of the two variable capacitors.....	22
Figure 17 - Capacitance VS Reverse Voltage for the Varicap Diode.....	22
Figure 18 - Schematic design of the identified tuning impedance circuit.	23
Figure 19 - Simulated Matching domain by the realized network.....	23
Figure 20 - Schematic overview of the antenna with the self-tuning network integrated inside the floatation device.	24
Figure 21 - Software Architecture implemented on the Microcontroller of the Self-Tuning Antenna.....	26
Figure 22 - Description of the Default Algorithm.	27
Figure 23 - Description of the Amplitude-based Backup Algorithm.....	28
Figure 24 - Description of the Phase-Based Backup Algorithm.....	29
Figure 25 - Model Considered for the Prototype Calibration.....	31
Figure 26 - Measurement Setup for the System Calibration.....	31
Figure 27 - Measured VS Simulated input/output characteristics of the prototype: (a) absolute value characteristic and (b) phase characterization.	32

Figure 28 - Measured CDF of the Reflection Coefficient when the antenna was worn by a volunteer: (a) meandered Dipole and (b) Bow-Tie antenna	34
Figure 29 - Measured CDF of the Reflection Coefficient when the antenna in proximity of water: (a) meandered Dipole and (b) Bow-Tie antenna	34
Figure 30 - Measurement of the Reflection Coefficient when the antenna was worn by a volunteer during failure emulation: (a) absolute value and (b) phase value.	35
Figure 31 - Detail of the measured reflection coefficient during the automated tuning procedure using the default algorithm.	36
Figure 32 - Detail of the measured reflection coefficient during the automated tuning procedure using the backup algorithm#2 (Only phase information available to the microcontroller).....	36
Figure 33 - Combination of the fractal shape, the active control circuit and the textile technology to realize an UHF reconfigurable textile wearable antenna.....	40
Figure 34 - Antenna design proposed in [37]	41
Figure 35 - Different design solution for a wearable antenna: (a) multiband antenna proposed in [38], (b) dual polarized antenna proposed in [44], (c) circularly polarized antenna proposed in [47], (d) solution with an Electromagnetic Band Gap proposed in [50].....	42
Figure 36 - Stress test carried out for a wearable antenna: (a) bending in [49], (b) washing in [55], (c) harsh environment with water or ice in [57], and (d) shotgun blast in [58].....	42
Figure 37 - Wearable antenna with active circuitry: (a) Beamforming circuit proposed in [63] and (b) antenna with an energy harvesting solar panel integrated [67].....	43
Figure 38 - Wearable antenna design adapted for a specific purpose: (a) maximization of the radiation pattern along the human body proposed in [69], (b) maximization of the intra-body communication link in [72], (c) array disposition to achieve a long off body link in [76] and (d) deployment in the Ka band [78].44	44
Figure 39 - Different stages of the Sierpinski triangle fractal, obtained by iterating the algorithm of triangle subtraction	45
Figure 40 - Selected candidates shapes to be the final shape of the textile antenna	45
Figure 41 - Side view of the geometry for the simulations of the different antenna shapes proximity of the human body	46
Figure 42 - Simulated Reflection Coefficient for different Sierpinski fractal shapes in free space.....	47
Figure 43 - Resonance frequency versus distance from the human chest, for different Sierpinski fractal antenna shapes.....	47
Figure 44 - Final modification of the Sierpinski fractal antenna	47
Figure 45 - Schematic view of the tuning circuit.....	48
Figure 46 - Simulated Matching Domain for the realized circuit: (a) 868MHz and (b) 915MHz	49
Figure 47 - Realized Active Control Circuit.....	49
Figure 48 - Fabrication Process of the wearable antenna: (a) from a conductive sheet, (b) the shape of the antenna is obtained. (c) a special glue is used on the back of the obtained shape. (d) the shape is glued to a textile aramid substrate.....	50
Figure 49 - Measured Reflection Coefficient optimized for the frequency of 868MHz and 915MHz.....	51
Figure 50 - 3D measured radiation pattern in the ISM bands: (a) 868MHz and (b) 915MHz.....	51
Figure 51 - Principal plane considered in the measurement of the radiating pattern.....	52
Figure 52 - Radiating Pattern at 868MHz on the principal planes: (a) $\varphi=0^\circ$ and (b) $\varphi=180^\circ$	52
Figure 53 - Radiating Pattern at 915MHz on the principal planes: (a) $\varphi=0^\circ$ and (b) $\varphi=180^\circ$	52
Figure 54 - Measurement setup for the “Power Transmission” Test.....	53
Figure 55 - Standard Horn antenna deployed for the measurement in the anechoic chamber.....	53

Figure 56 - Gain VS Frequency of the Standard Gain Horn.....	53
Figure 57 - Prototype adapted to 868MHz	54
Figure 58 - Cumulative Density function for the realized prototype while the wearer were performing random movements for both 868MHz and 915MHz ISM frequencies.	54
Figure 59 - Typical configuration described in [82].....	57
Figure 60 - Different design for being integrated on a car: (a) integration on the car top [88]and (b) in the back window [90].....	57
Figure 61 - Different configuration for a Self-Structuring antenna: (a) interconnection of wire performed by switches [93], and (b) shorting pins insertion controlled by switches [94]	58
Figure 62 - Integration of the Self-Structuring antenna on the floating element of a commercial life-jacket	59
Figure 63 - Design of the Self-Structuring antenna: (a) antenna geometry, (b) principal outer branch and (c) principal inner branch.	59
Figure 64 - Simulated S_{11} for the two principal configurations shown in Figure 63	60
Figure 65 - Working principle of the Self-Structuring antenna	60
Figure 66 - Different immersion condition considered for the simulated layout: (a) antenna foundering, (b) lateral rotation and (c) frontal rotation.	61
Figure 67 - Simulated S_{11} for different floating antenna positions with respect to water level: (a) antenna sinking; (b) lateral rotation and (c) frontal rotation..	62
Figure 68 - Simulated Radiation Pattern for the self-structuring layout: (a) antenna sinking; (b) lateral rotation and (c) frontal rotation	63
Figure 69 - SATURN End-to-End Communication System.....	67
Figure 70 - SATURN End-to-End Communication System.....	68
Figure 71 - SATURN Antenna.....	68
Figure 72 - DVB-SH Tuner	69
Figure 73 - SATURN Plotter.....	69
Figure 74 - Different inclination angles for a vessel	70
Figure 75 - Roll Angle Profile.....	71
Figure 76 - Pitch Angle Profile	71
Figure 77 - Yaw Angle Profile	71
Figure 78 - SATURN Prototype.....	72
Figure 79 - Measured C/N level	74
Figure 80 - Forward Link Chain block scheme.....	74
Figure 81 - ESR5(20) measured in more than an hour	76
Figure 82 - Packet reception for the Beam Switching Time measurement. The blue dots represent the packets lost during the reception	76
Figure 83 - Return Link Chain block scheme.....	77
Figure 84 - Example Of Sea Weather Update Correctly Displayed on the SATURN Plotter	79
Figure 85 - Example of Sea Alarm Message Correctly sent to the Hub	80

Publications

International Journals

1. **Baroni, A.**; Nepa, P.; Rogier, H.; , "*A Wearable Self-Tuning Antenna for Emergency Rescue Operations*" in *Microwaves, Antennas & Propagation, IET*, To be appear

International Conferences

2. Buffi, A.; **Baroni, A.**; Nepa P.; , "Experimental Validation of Phase-Based Localization of UHF-RFID tags moving on a Conveyor Belt" *Antennas and Propagation Society International Symposium (APSURSI)*, 2013 IEEE
3. **Baroni, A.**; Baroni, A.; Pannozzo, M., Zamberlan, D., Andrenacci, M., and Silvestri, F.; , "*Performance Assessment of the Smart mAritime saTellite terminal for mUltimedia seRvices and conteNts (SATURN) system* ", 7th Advanced Satellite Multimedia System Conference – 13th Signal processing for Space Communications Workshop, Livorno, Italy, September, 2014
4. **Baroni, A.**; Nepa, P.; Rogier, H.; , "*A reconfigurable layout for a self-structuring lifejacket-integrated antenna of a SAR system*, " *Antennas and Propagation Society International Symposium (APSURSI)*, Vancouver, Canada July 2015 IEEE
5. **Baroni, A.**; Nepa, P.; , "*Auto Tuning Network for Cospas Sarsat Application*" 1st URSI Atlantic Radio Science Conference (URSI AT-RASC), Gran Canaria, Spain, May 2015 IEEE

6. **Baroni, A.**; Rogier, H.; Nepa, P.; , "*Wearable Active Sierpinski Fractal Antenna for Off-Body Communication*" Electromagnetics in Advanced Applications (ICEAA), 2014 International Conference on, Torino, Italy, 2015 IEEE

National Conferences

7. Buffi, A.; Baroni, A.; Caso, R.; D'Alessandro, A.; **Baroni, A.**, and Nepa, P. "*Research Activities On UHF RFID Systems At The University Of Pisa - Research Unit*," *Proceedings of XX RiNEm*, Padova, Italy, September 2014
8. **Baroni, A.**; Nepa, P.; , "*Wearable Auto-Tuning Antenna for COSPAS-SARSAT Rescue Applications*," *Proceedings of XX RiNEm*, Padova, Italy, September, 2014

Introduction

Adaptive antennas represent a special class of antennas able to perform dynamic modifications on the radiating parameters according to a proper algorithm. These radiating parameters (input impedance and radiation pattern) can be modified for different purposes. As an example, the control of the input impedance allows the selection of a particular working frequency in multi bands applications. The control of the input impedance can be also used in wearable devices. Sure enough, such devices are exposed to user movements, dealing with compression, stretching, and bending. These deformations can cause alteration in the current distributions on the topology causing a detuning in the frequency response. Another parameter that can be controlled in an adaptive antenna is the radiation pattern. Changes in the active beam can be exploited to receive or transmit signal toward a particular direction.

In this context, the author studied and designed different solution of adaptive antenna system.

In a first part, the development of a self-tuning network able to dynamically compensate the reflection coefficient detuning is depicted. The designed system has been realized to be integrated on the floating element of a life jacket. The realized prototype is fully compliant with the Cospas Sarsat Satellite System at the UHF frequency of 406MHz.

In a second part, a Wearable Active Sierpinski Fractal Antenna for Off-Body Communication is proposed. The antenna has been directly integrated onto garment using the e-textile technology. The realized system is able to work at the ISM frequencies of the 868MHz and 915MHz thanks to a proper feeding structure. The dual frequency textile antenna has been proposed by the research group at the Information Engineering Department of the Ghent University (Ghent, Belgium), where the author spent seven months as a Visiting Scholar.

In the third chapter, a layout for a self-structuring antenna for Search and Rescue application is proposed. The layout is intended to allow dynamic changes in the radiating shape in order to guarantee the satellite link in maritime environment for Search and Rescue applications.

At the end, the main measured performance results of the SATURN (Smart mAritime saTellite terminal for mUltimedia seRvices and conteNts) system are summarized. The SATURN project aimed to design and develop a maritime user terminal for small leisure boats (up to 20m of length). Such a terminal has an adaptive antenna able to change the radiation pattern of the antenna according to the actual position of the vessel with respect to a geostationary satellite allowing navigators to receive contents through a DVB-SH channel and to transmit small amount of data via an ETSI S-MIM return channel (based on the Enhanced Spread Spectrum protocol) in the S-Band. The system performance has been measured in a real environment, emulating the sea condition by means of an ad-hoc designed Motion Simulator.

1 A wearable Self Tuning Network for Emergency Rescue Operations

1.1 Introduction

In this chapter, the design, the hardware implementation and the characterization of a self-tuning antenna is presented.

The realized prototype is intended to be compliant with the Cospas-Sarsat Satellite Emergency System for the UHF frequency of 406MHz and it is intended to be integrated as a personal locator beacon on a commercial life jacket.

The realized prototype is able to perform automatic tuning of the antenna under time-varying environmental conditions due to human body movements and sea water proximity. The impedance tuning is performed by tracking the instantaneous value of the reflection coefficient and by modifying an appropriate impedance matching network according to a real-time adaptive algorithm. A resilient default/backup software architecture has been designed to ensure that tuning guarantees a return loss higher than 14dB for the personal locator beacon in most of impedance mismatching conditions.

This chapter will begin with a brief analysis of the working environment and a description of the Cospas Sarsat Satellite system. After the identification of the general requirement, the hardware implementation and the software architecture will be analysed. The realized prototype has been validated with the antenna directly worn by a volunteer in different working condition. The reflection coefficient, treated as a random parameter, has been collected to create its Cumulative Density Function with the antenna in different environment.

1.2 Working Environment and General Requirement

The International Cospas-Sarsat Programme [1] is a satellite-based search and rescue (SAR) distress alert detection and information distribution system, best known for detecting and locating emergency beacons activated by aircraft, ships and backcountry hikers in distress (Figure 1). The International Cospas-Sarsat Programme provides an accurate, timely, and reliable distress alert and location data to help search and rescue authorities assist persons in distress. During an emergency situation, a Cospas-Sarsat radio-beacon transmits a distress signal to a constellation of satellites (LEOSAR and GEOSAR). Specifically, a 406 MHz personal locator beacon emits a 5-Watt half-second burst approximately every 50 seconds [2]. The carrier frequency is phase-modulated with a digital message. This emergency message is then forwarded to a Ground Receiving Station, which informs a Rescue Coordinator Centre for the final rescue operations.

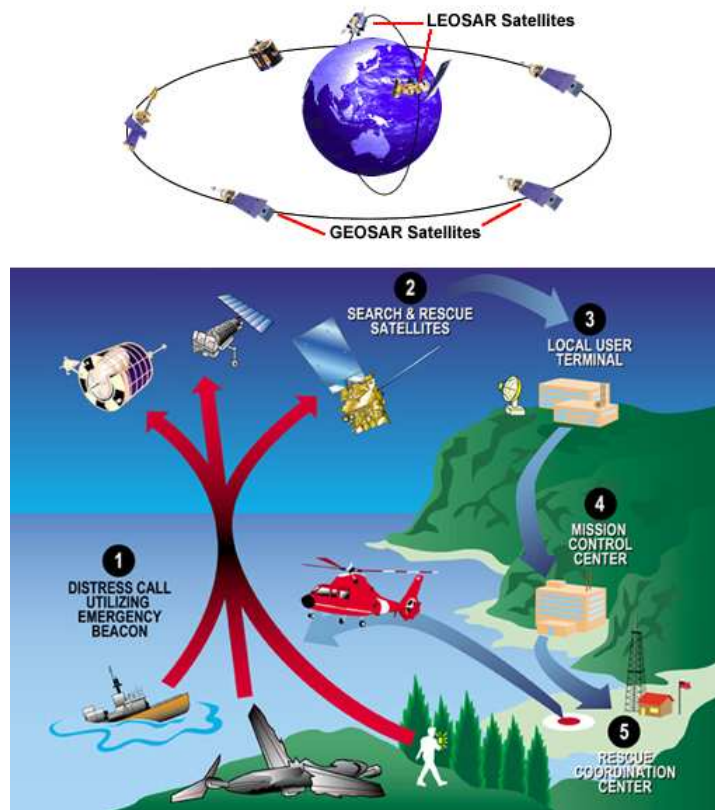


Figure 1 - Cospas Sarsat System Overview

The integration of such a system directly inside a commercial life-jacket increases the chances of survival of a human in an emergency scenario. However, when a personal locator beacon with a radiating element is located near to a human body, re-orientation and movements of the wearer may continuously modify the operating conditions of the transmit antenna due to random variations of the relative position of the antenna with respect to the human body [3]-[5]. Moreover, in a maritime scenario, the presence of the sea water may affect the principal radiating parameters (input impedance and radiation pattern) of a wearable antenna [6]. Detuning of the antenna may cause a serious impedance mismatch and load pulling in the power amplifier (PA), resulting in a significant portion of

the 5-Watt transmitter output signal being reflected back to the generator. Besides a serious reduction of the system efficiency, this reflected power may damage the source circuit. Special measures may be taken to protect the generator, such as the use of circulators, but this increases size and cost of the system and it reduces the power efficiency and, hence, the autonomy of the search and rescue system.

In this part, we propose a novel self-tuning Cospas-Sarsat antenna that adaptively and in real time compensates potential detuning to maintain the Reflection Coefficient below the -14dB threshold, while still guaranteeing an antenna gain between -3dBi and 4dBi over 90% of the region defined by all azimuth angles and by elevation angles greater than 5° and less than 60°, as required by the Cospas-Sarsat specification document [7]. The self-tuning network automatically reconfigures itself, by tracking the antenna impedance variations caused by the movements of the wearer. The proposed solution estimates the mismatch level by measuring both the absolute value and the phase of the actual reflection coefficient. Continuous impedance matching regulation is performed by using a simple circuit based on varicap diodes. Robust minimization of impedance mismatch is performed by a resilient default/backup software architecture solution. In normal operating conditions, an adaptive algorithm performs impedance matching based on both absolute value and phase of the reflection coefficient. However, when one of these quantities becomes unavailable, the microcontroller still ensures impedance matching by switching to one of two different backup algorithms that minimize the impedance mismatch based on one parameter only. Such a failsafe implementation improves the overall reliability of the system in an emergency situation. The self-tuning system guarantees that vital information is received by the Cospas-Sarsat satellites during a rescue operation, by maintaining antenna matching, gain and autonomy during the required complete 24 hours timeframe. The alternative solution, which consists of deploying an isolator before the antenna, to protect the PA by absorbing the reflected power, will reduce the system autonomy and the antenna gain. As an example, a worst case reflection coefficient of -4.1dB, as observed in the experiments performed graphically depicted in Figure 2, will require that almost 2W of power (being 39% of the power delivered by the PA) is absorbed by the isolator load, reducing the antenna gain by 2.1dB and limiting the system autonomy to 15hours and 16 minutes instead of 24hours, if the same battery is applied.

Results will be presented for different working environment. Sure enough, the final system will be worn by a volunteer performing random movement and will be located close by salt water (salinity level of 35‰) in a recipient that is slightly moved in a continuous manner, to emulate variation of the sea surface, caused, for example, by the sea waves. To obtain a better view on the design challenge, Table 1 presents some worst-case results for the different scenarios. When the antenna is deployed on the water, the reflection coefficient can assume values up to -4.1dB. In this case, 39% of the total output power is lost due to reflections whereas only 61% is available for antenna radiation. If we do not compensate for this mismatch, a power of several watts will have to be dissipated somewhere in the transmit chain (for example, by a bulky and costly drop-in isolator), reducing the antenna total gain and the system autonomy. Therefore, we prefer to compensate for the mismatch by proposing an appropriate tuning network.

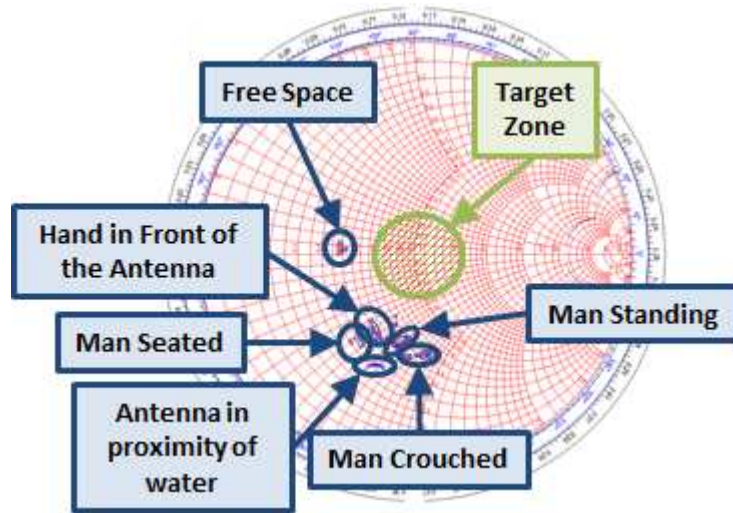


Figure 2 - Measured Reflection Coefficient on the Smith Chart for different movements of the wearer

TABLE I
WORST-CASE REFLECTION COEFFICIENT, ANTENNA TOTAL GAIN REDUCTION AND POWER REFLECTED DUE TO ANTENNA MISMATCH, FOR DIFFERENT ANTENNA OPERATING CONDITIONS, ASSUMING 5W INJECTED POWER

Position of the antenna	Reflection Coefficient	Total Gain Reduction	Max reflected power
Free Space	-8.7 dB	0.63 dB	0.674 W (13%)
Hand in front of the antenna	-6.1 dB	1.22 dB	1.227 W (24%)
Man Standing	-6.8 dB	1.02 dB	1.045 W (21%)
Man Seated	-5.7 dB	1.36 dB	1.346 W (27%)
Man Crouched	-6.0 dB	1.26 dB	1.256 W (25%)
Water Proximity	-4.1dB	2.13dB	1.945 W (39%)

1.3 State of Art Overview

On the one hand, different kinds of wearable antenna integrated on commercial life-jacket (Figure 3) have been presented over the past years for the Cospas-Sarsat system at the UHF frequency of 406MHz [6], [8].

However, these designs do not fully consider the effect of variations in the antenna's operating conditions due to the wearer re-orientation and movement. On the other hand, closed-loop self-tuning impedance networks were investigated for other applications [9]-[10].

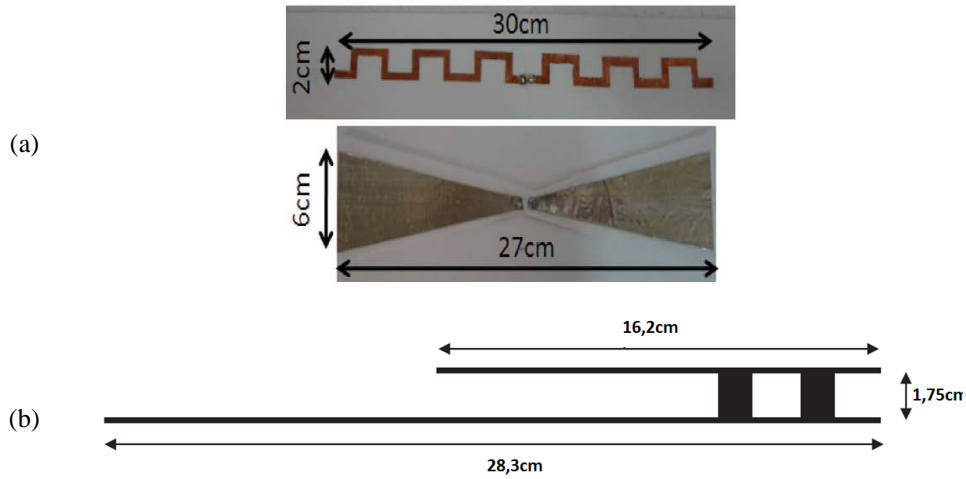
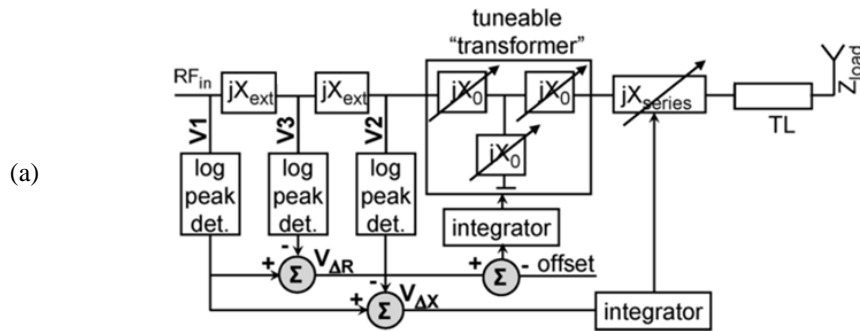


Figure 3 - Cospas Sarsat Antennas: (a) design proposed in [6] and (b) design proposed in [8]

In open literature, different designs of self-tuning circuit are reported (Figure 4). A first characterization aspect is related to the collection of the feedback data. One potential solution consists in measuring current or voltage values at different points of the circuit [11]-[12]. An alternative possibility is to sense the signals before and after the impedance matching network to determine the impedance mismatching level [13]. Other designs rely on directional couplers to monitor the direct and reflected waves [14]-[16], from which the reflection coefficient may be calculated.



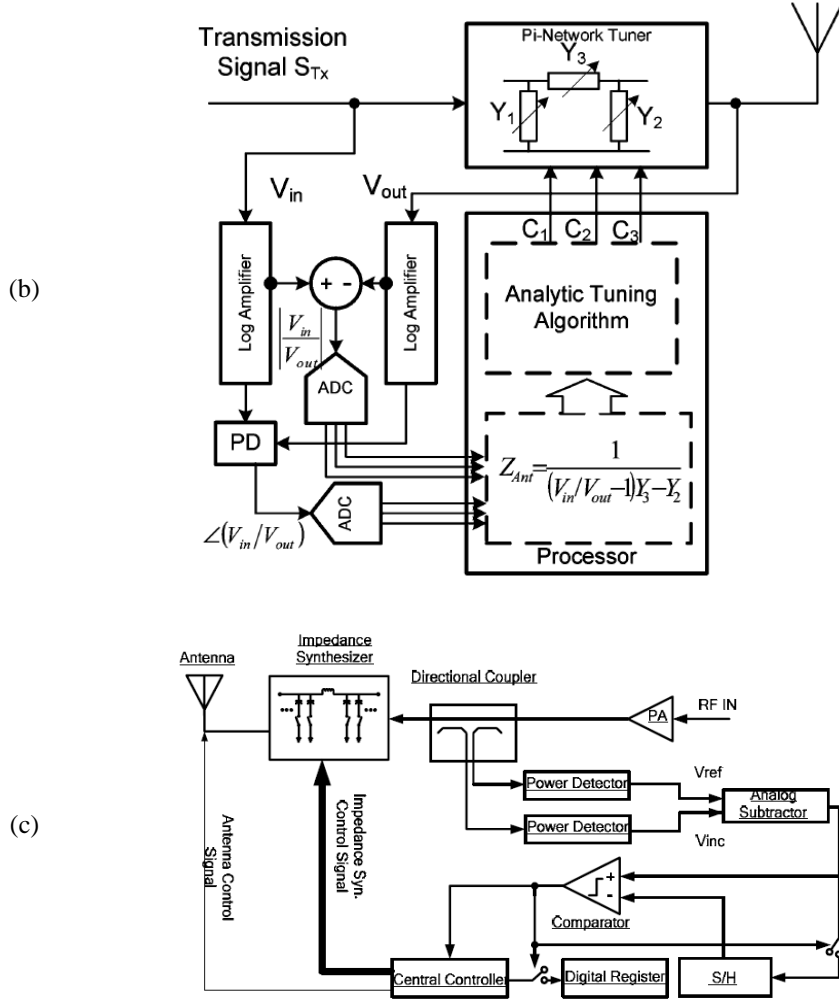


Figure 4 - Tuning Network: (a) design proposed in [11], (b) design proposed in [13] and (c) design proposed in [15]

The adaptive algorithm that modifies the impedance matching network must be customized to the type of impedance matching circuit deployed (Figure 5). Some papers [17]-[18] propose a discrete impedance matching network, consisting of a bank of capacitors or inductors, together with global optimization algorithms such as the genetic algorithm, the simulated annealing algorithm or the ant colony optimization algorithm [19]. However, this setup occupies a lot of space, which may not be available on a commercial life-jacket. To miniaturize the electronic circuit, MEMS technology is applied in [20]-[21]. Nevertheless, this technology does not result in a low cost solution and its use in stub-based or transmission-line-based MEMS matching networks is impractical at the Cospas-Sarsat frequencies, as even miniaturization by the use of slow-wave structures leads matching circuit footprints in the order of the wavelength. In other applications, the use of varicap diodes [22]-[24] has resulted in low cost and compact reconfigurable solutions. For tunable capacitors, a lookup table may be used to predict the optimal capacitor value [25]. However, such an approach does not take into account the tolerance on every component in the matching network. Therefore, in this thesis, a

dedicated software architecture has been developed.

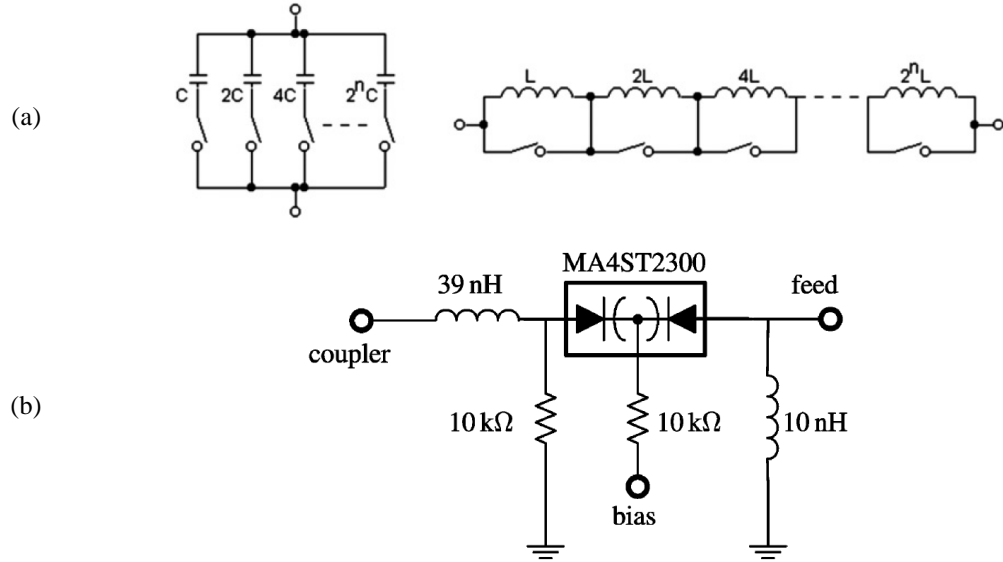


Figure 5 - Type of impedance matching circuit: (a) design proposed in [17] and (b) design proposed in [22]

1.4 Hardware Description

A self-tuning network is a closed loop system, basically composed by three macro elements as depicted in Figure 6. It is a component that will be inserted between the signal generator and the radiating element responsible to adjust the input impedance of the antenna according to a particular algorithm.

Starting from the Signal Generator, the first inserted element is the Signal Parameter Extraction. This element is responsible to catch information regarding the functioning condition of the overall system. Collected information are then sent to the second element, called Microcontroller Section. In this block the extracted parameters are elaborated in order to select the correct action to be done on the third block, the Impedance Matching Network. Variations on the internal parameters of this part correspond in variations in the input impedance of the antenna.

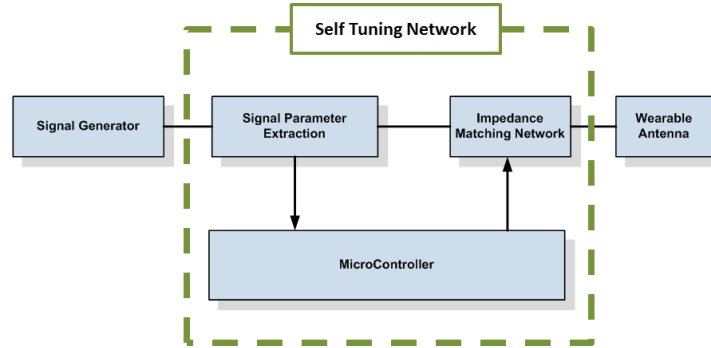


Figure 6 - Closed-Loop Self-Tuning Network Concept.

The first block of the Self Tuning Network is the Signal Parameter Extraction. Since the input impedance has been selected as the parameter under investigation, this block is responsible to provide the direct and the reflected wave to the Microcontroller Section.

The latter quantities can be sensed from the RF signal by means of two different three-port directional couplers. Thanks to their high directivity combined with a low insertion loss, the ZFDC-20-5 [26] and the ZFDC-10-5 [27] are the components that have been chosen. They can be deployed to frequency up to 2GHz, making this circuit available to work at different frequency. The main parameters of the selected directional couplers (Figure 7) are reported in Table 2.



Figure 7 - Directional Coupler: (a) the ZFDC-20-5 for the direct wave sensing and (b) the ZFDC-10-5-S for the reflected wave sensing

TABLE 2
MAIN PARAMETER OF THE DEPLOYED DIRECTIONAL COUPLERS

	ZFDC-20-5-S	ZFDC-10-5-S
Frequency Range	0.1 to 2000MHz	1 to 2000MHz
Insertion Loss	0.69dB	1.19dB
Coupling	19.85dB	10.77dB
Directivity	30.03dB	31.82dB

The second element of the Self Tuning Network is the Microcontroller Section. This section has been divided into three different parts according to three different purposes that should be fulfilled in this section (Figure 8). The first needed step is to transform the direct and the reflected wave into the reflection coefficient, thereafter the action to be done on the impedance matching network should be decided. The last step is to physically operate on the circuit to apply the required modifications.

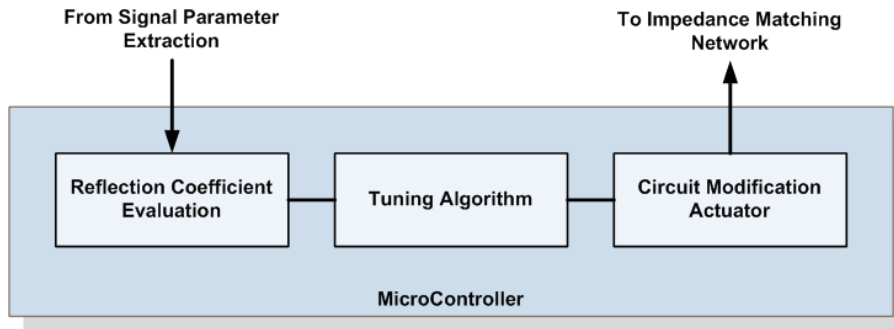


Figure 8 - Internal Section of the MicroController Block.

The component deployed for measuring the Reflection Coefficient is the integrated circuit AD8302 realized by Analog Devices [28] and shown with its own evaluation board in Figure 9. The integrated circuit presents two input pins where the direct and the reflected wave would be applied. Measured phase and gain are available as output in form of voltage signal.

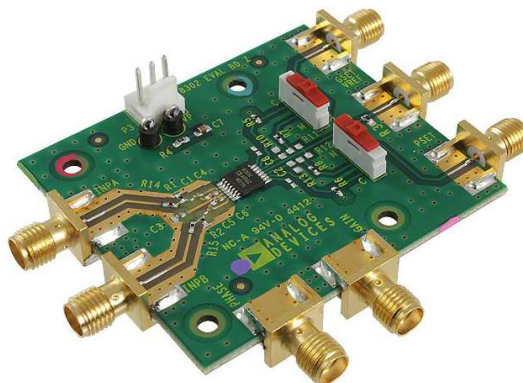


Figure 9 - AD8302 Evaluation Board

The AD8302 is comprised of two closely matched logarithmic amplifiers (Figure 10) that accept input power from -60dBm up to 0dBm in a 50Ω system. By taking the difference of their outputs, the magnitude ratio of the two input signals is available. It also contains a phase detector to measure the phase difference of the two input signals. Its output characteristics are shown in Figure 11, whereas its principal features are collected in Table 3.

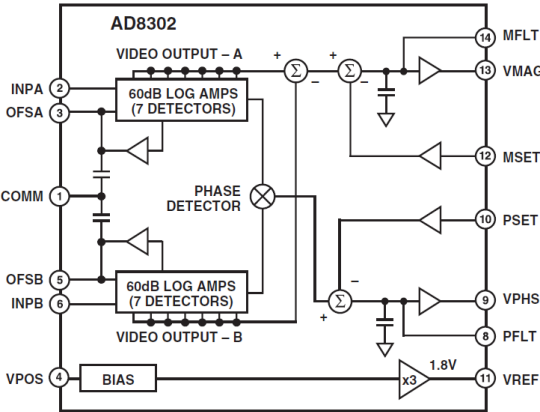


Figure 10 - Functional Block Diagram of the AD8302

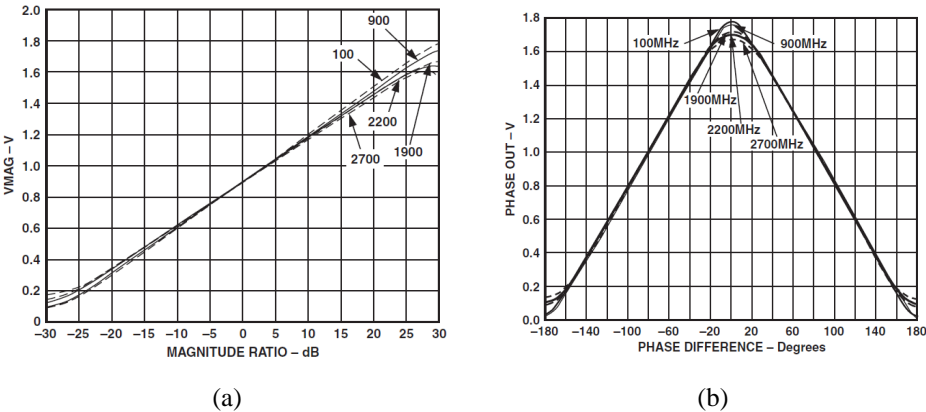


Figure 11 - Output Characteristics of the AD8302: (a) Output Voltage VS Magnitude Ratio and (b) Output Voltage VS Phase Difference.

TABLE 3
 MAIN PARAMETER OF THE AD8302
 Main Features

Frequency Range	Up to 2.7GHz
Input Range	From -60dBm to 0dBm
Power Supply	2.7 – 5.5 V
Applications	

RF/IF PA Linearization		
Precise RF Power Control		
Remote System Monitoring and Diagnostic		
Return Loss/VSWR Measurements		
Log Ratio Function for AC Signal		
Output Characteristics		
Magnitude Output	$\pm 30\text{dB}$	30mV/dB
Phase Output	$0^\circ\text{-}180^\circ$	10mV/dB

Measured Reflection Coefficient is then given in input to the Tuning Algorithm running on the Microcontroller (Second section of Figure 8) to achieve impedance matching.

The ATmega328P, mounted on an Arduino UNO board (Figure 12), is the chosen microcontroller [29]. It has 14 digital input/output pins (of which 6 can be used as PWM outputs), 6 analog inputs, a 16 MHz quartz crystal and a USB connection. It is enough to connect it to a computer with a USB cable or power it with an AC-to-DC adapter or battery to get started. Its main characteristics are summarized in Table 4.

Adjustments of the input impedance are made on the base of the Software architecture described in Section 1.5.

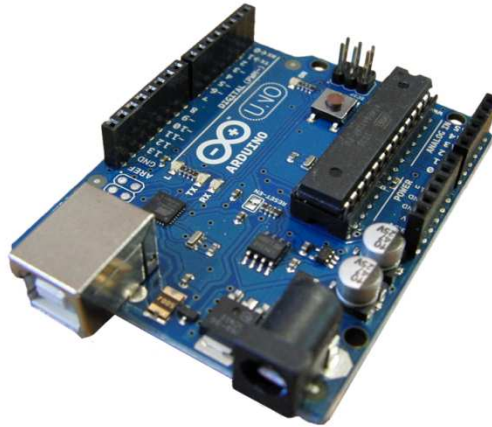


Figure 12 - Arduino UNO Board

TABLE 4
MAIN PARAMETER OF THE ARDUINO UNO
Main Features

Based on	ATMega328P
Operating Voltage	5V
Digital I/O pins	14
Analog Input Pins	6
Clock Speed	16MHz
Size	6.86cm x 5.34cm

Input Pins Characteristics P	
Voltage Range	0V – max 5V
Bit Discretization	10
Maximum Reading Rate	10kSample per Second

The third component deployed in the Microcontroller Section is the Circuit Modification Actuator. This component is needed in order to link the digital world of the Microcontroller with the analogic world of the varicap diodes that have been chosen for the being the variable element of the circuit as described later on this section.

To fulfil this task the AD5504 [30] has been selected. This Integrated Circuit, which is shown in Figure 13 with its evaluation board, is a quad-channel, 12-bit, serial input, digital-to-analog converter with on-chip high voltage output amplifiers and an integrated precision reference. The AD5504 has a high speed serial interface, and can handle clock speeds up to 16.667MHz. In Figure 14, its functional block diagram is reported. This component became useless when using a microcontroller with analogic output (i.e. the Arduino Due).

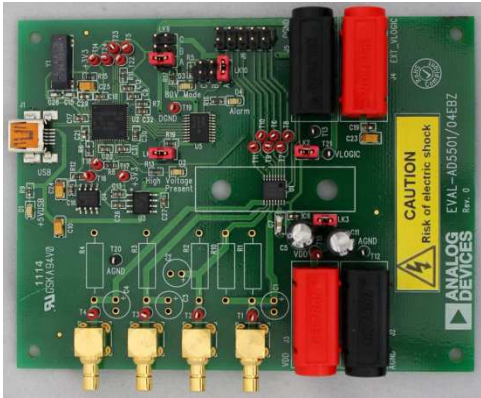


Figure 13 - AD5504 with its Evaluation Board.

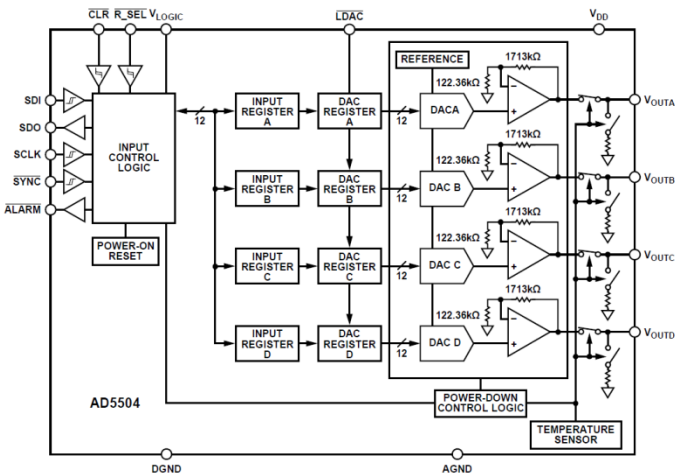


Figure 14 - Functional Block Diagram of the AD5504.

The last component of the self-tuning circuit previously depicted in Figure 6 is the impedance matching network.

To fix its topology and circuit component values, first the potential variations in reflection coefficient were quantified by measuring the reflection coefficients of a Meandered Dipole Cospas-Sarsat Antenna [6], when worn by a volunteer performing random movements and when floating on salt water (salinity level of 35‰) in a recipient that was slightly moved in a continuous manner, to emulate variations of the sea surface, caused, for example, by the sea waves as previously shown in Figure 2. On the base of the measured data, a double lowpass-upward-L tuning network (Figure 15) and its component values (Table 5) have been identified.

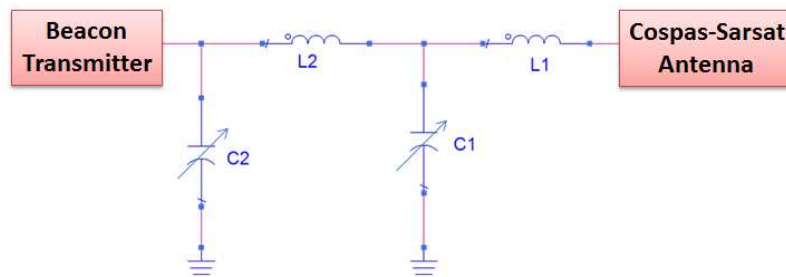


Figure 15 - Identified double lowpass-upward-L tuning network.

TABLE 5
VALUE OF THE TUNING CIRCUIT COMPONENTS

Component Name	Component Value
L1	29nH
C1	From 7pF to 20pF
L2	19.6nH
C2	From 2 to 30pF

The working principles of the designed circuit can be summarized as follow.

On the one hand, shunt capacitor C_2 only modifies the load susceptance; therefore it only allows movements along conductance circles on the Smith Chart. On the other hand, shunt capacitor C_1 affects both real and imaginary part of the reflection coefficient. Therefore, with this component we may select a different conductance circle (Figure 16).

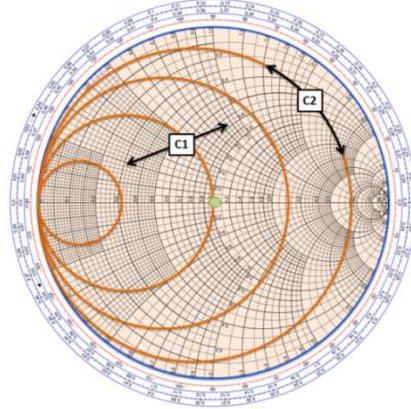


Figure 16 - Effect of the variations of the two variable capacitors

To implement the final circuit, first the tuning elements are selected. The MMBV105GLT1G [31] varicap diodes exhibit a junction capacitance ranging from 4pF to 18pF, when a reverse voltage of 12 Volt and 0.5 Volt is applied, respectively as shown in Figure 17.

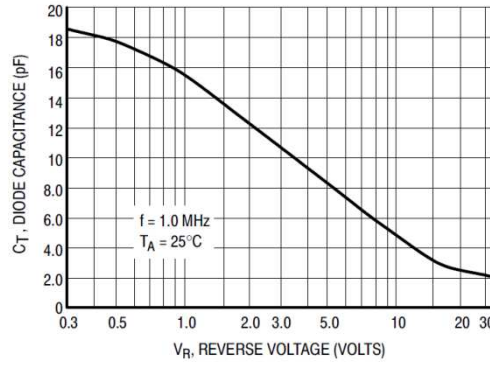


Figure 17 - Capacitance VS Reverse Voltage for the Varicap Diode.

To cover the complete capacitance range put forward in Table 5, some modifications of the circuit topology in Figure 15 are needed. The variable range of the capacitor C_1 equals 7-20pF. This range may be covered by a series connection of a single varicap diode and a single shunt 2pF bias capacitor, shifting the dynamic available range to 6pF-20pF. As for C_2 , to cover the simulated dynamic range of 30pF, three varicap diodes are deployed together with a shunt inductor of 15nH, to shift the dynamic capacitance range from 12pF-54pF to 2pF-44pF. Finally, a set of choke inductors and DC blocks are added to block the radio-frequency (RF) signal towards the microcontroller and to isolate the DC commands sent to different varicap diodes, respectively. Above considerations result in the impedance matching circuit shown in Figure 18. The tuning range of the final network is shown in Figure 19.

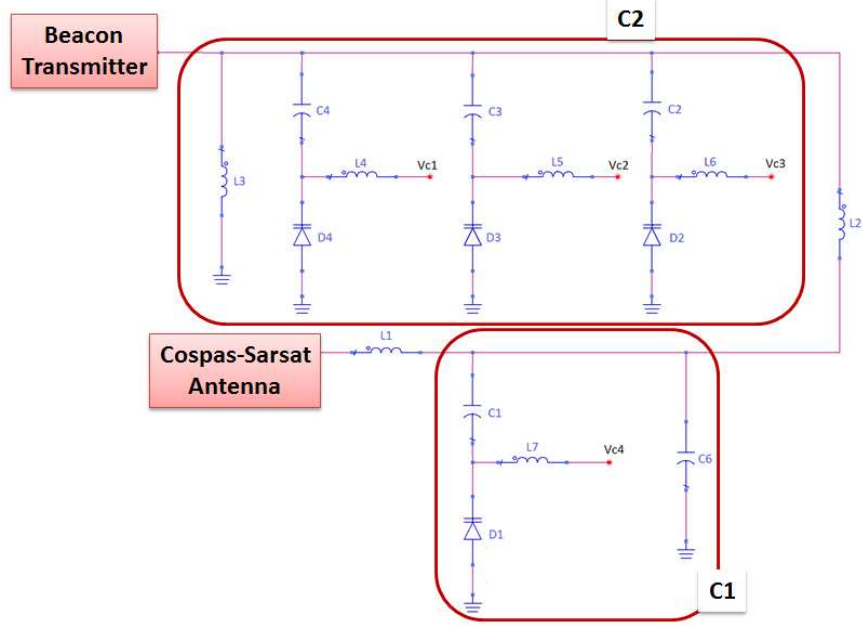


Figure 18 - Schematic design of the identified tuning impedance circuit.

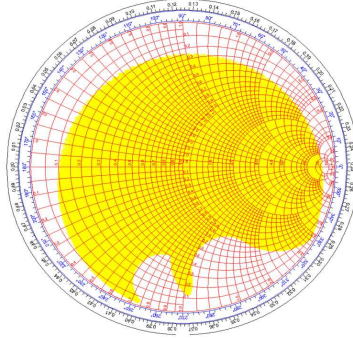


Figure 19 - Simulated Matching domain by the realized network.

The final structure of the self-tuning network is the result of a comprehensive analysis procedure where the best network topology and components were selected in terms of small dimensions and low cost, to keep the overall size and the price as small as possible. Therefore, in the impedance matching network, only passive SMD components with unit cost lower than 0.5€ have been deployed. The selected varicap diodes cost 0.22€ per piece. Special attention should be devoted to the directional coupler. Many suitable off-the-shelf couplers, such as the MACP-011013 [32], are available at a price in the order of 1€ per component. Moreover, in the final integration, the microcontroller and the gain/phase detector used for the antenna section can be shared with the Cospas-Sarsat transmitter to reduce the price even further. All these considerations limit the cost of the impedance matching network to a small fraction of the overall module, taking into account that a commercial life-jacket has a price of around 20\$ and the average cost of a commercial Cospas-Sarsat transmitter is around 200\$.

The integration of the self-tuning network into the floatation device of a commercial life-jacket is shown in Figure 20. The antenna is located on the upper side of the floating element whereas the self-

tuning network is integrated inside the floating element. Tests have been conducted to verify the behaviour of the self-tuning network when deployed near the radiating element. These tests have demonstrated that the proximity of the antenna does not affect the impedance matching procedure.

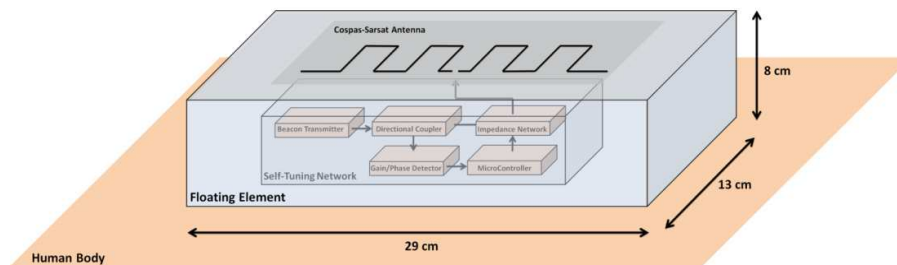


Figure 20 - Schematic overview of the antenna with the self-tuning network integrated inside the floatation device.

1.5 Software Architecture

The software architecture is composed by all the software elements that have been developed in order to make the system fully working. It is principally composed of two different parts. One part is composed by the tuning algorithms and the second part is composed by all the accessory parts that permit to the microcontroller to interact with the external world (i.e. SPI communication with the ADC, Serial communication with the PC).

The tuning algorithms form the functional core of the system, as they act on the impedance matching network to minimize the impedance mismatch of the narrowband Cospas-Sarsat antenna. Therefore, they rely on the incident and reflected waves between antenna and tuning element, which are monitored in real time. The control unit iterates until the best matching solution is achieved along a tuning trajectory controlled by the optimization algorithm, starting from an arbitrary point in the two-dimensional impedance plane.

A lookup-table mechanism could be applied to calculate the exact values of the varicap diodes. However, this method has been discarded, mainly due to component tolerances and temperature-dependent variations in the physical components employed in the impedance matching network, which may affect the correctness of impedance matching based on fixed lookup table values. Hence, optimal impedance matching cannot be achieved by a static approach. Therefore, a dynamic adaptation strategy was adopted.

A robust failsafe software architecture that relies on three different kinds of algorithms has been implemented (Figure 21). All of them were programmed on the microcontroller and tested. A default algorithm achieves impedance matching based on all the physical quantities that can be provided by the gain/phase detector, being both the absolute value and the phase of the reflection coefficient. In addition, two backup algorithms are available in case of some malfunction of either the gain/phase detector, or when deploying off-the-shelf components able to provide only one of the two mentioned quantities to the microcontroller. In that case, they perform the impedance matching by relying on only one physical quantity measured by the gain/phase detector, being either the amplitude or the phase of the reflection coefficient. Hence, when the microcontroller detects that either the amplitude or the phase measurement is unavailable or its data are unreliable, it switches to the most appropriate algorithm to still ensure impedance matching.

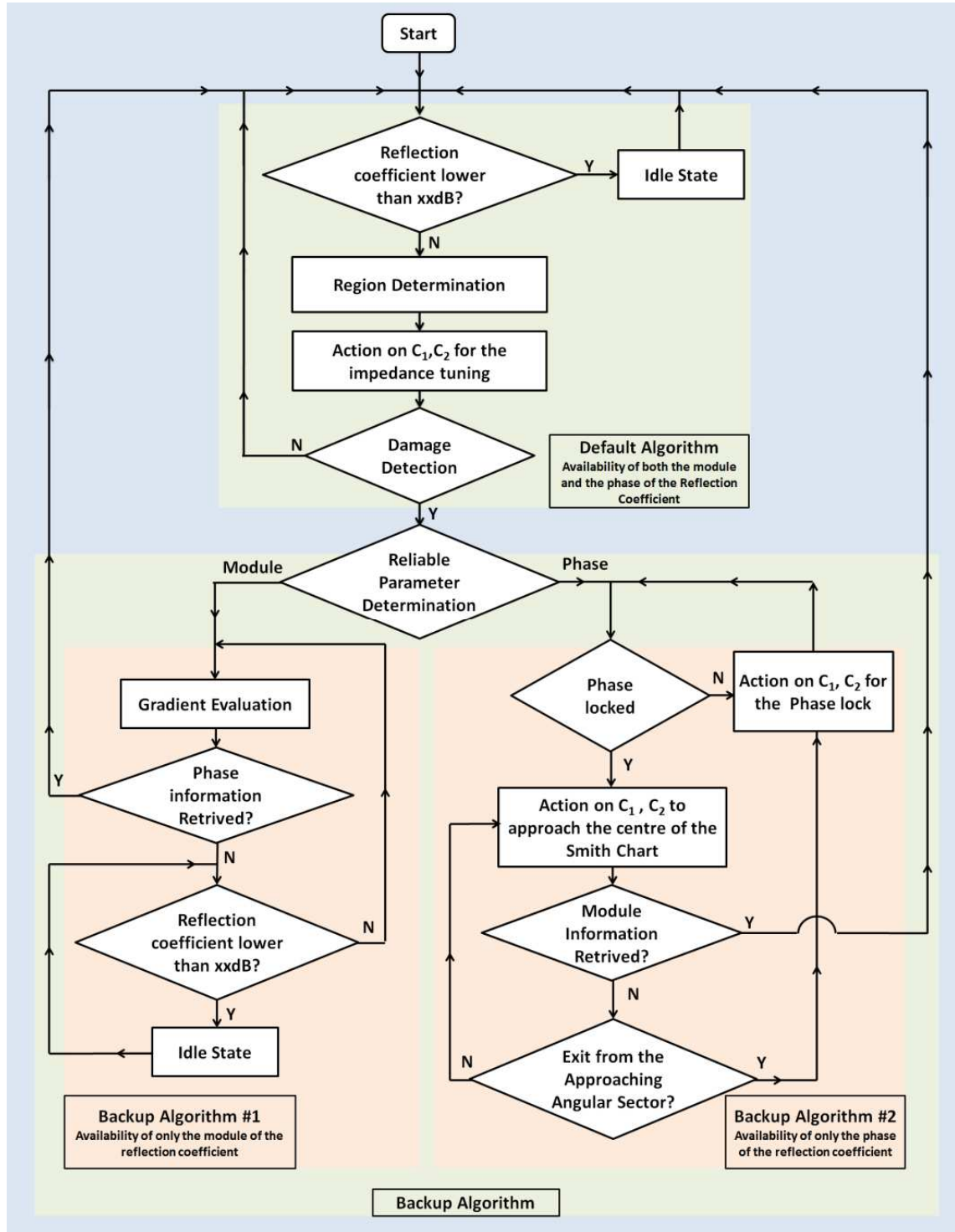


Figure 21 - Software Architecture implemented on the Microcontroller of the Self-Tuning Antenna.

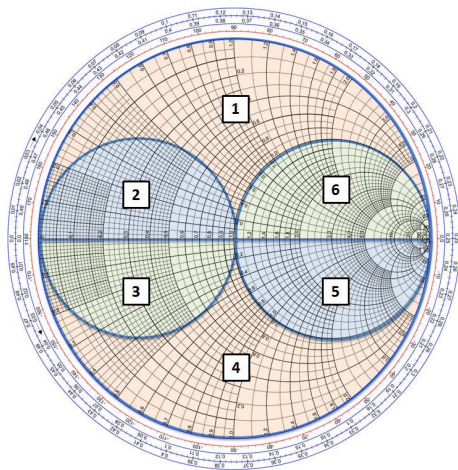
In the default algorithm the entire Smith Chart is subdivided into 6 different regions (Figure 22), based on the real (larger or smaller than 1) and imaginary parts (positive or negative) of the normalized impedance and on the real part of the admittance (greater or lower than 1). The knowledge of both the amplitude and the phase of the reflection coefficient permits to identify the region in which the reflection coefficient is located.

Adaptations performed on the two variable capacitors depend on the particular region on the Smith Chart in which the reflection coefficient is located. Real-time tuning is achieved by modifying the variable components according to the actions described in Table 6 .

TABLE 6
ACTION ON THE TWO VARIABLE CAPACITORS FOR THE DEFAULT ALGORITHM

Region	C ₁ Action	C ₂ Action
1	Decrease Capacitance	Decrease Capacitance
2	Increase Capacitance	Decrease Capacitance
3	Increase Capacitance	Increase Capacitance
4	Decrease Capacitance	Increase Capacitance
5	Decrease Capacitance	Increase Capacitance
6	Decrease Capacitance	Decrease Capacitance

This process (determining the correct region and adapting the variable components) is repeated until optimal matching is reached. The availability of the magnitude of the real-time reflection coefficient as a feedback signal also permits to define a stopping criterion. For instance, we may aim for a magnitude of the reflection coefficient that is lower than -15dB. Once the magnitude threshold is reached, the microcontroller can be set to standby mode, decreasing its energy consumption and enlarging the system autonomy.



Default algorithm

Input data: Reflection coefficient amplitude and phase.

Summary: The Smith Chart is subdivided into 6 regions. According to the specific location of the reflection coefficient, the variable components in the impedance matching network are adapted as described in Table 6.

Figure 22 - Description of the Default Algorithm.

The first backup algorithm only relies on the measured magnitude of the reflection coefficient to

achieve impedance matching. The absolute value of the reflection coefficient depends on both the impedance of the antenna and the impedance matching circuit. On the one hand, variations on the antenna impedance matching cannot be controlled, as they depend on the working environment and on the wearer movements. On the other hand, the state of the tuning network can be controlled by the microcontroller. Therefore, the minimization is performed by exploiting its local gradient with respect to the two variable elements C_1 and C_2 (Figure 23). The estimation of the local gradient is performed by measuring the partial derivative components along the single dimension (both C_1 and C_2). Also in this case, the knowledge of the magnitude of the reflection coefficient is used to define a stopping criterion.

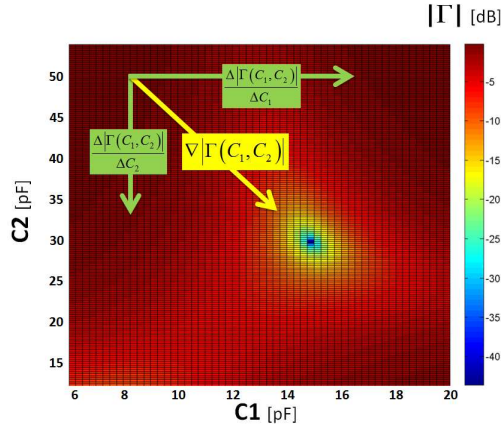


Figure 23 - Description of the Amplitude-based Backup Algorithm.

Backup Algorithm #1

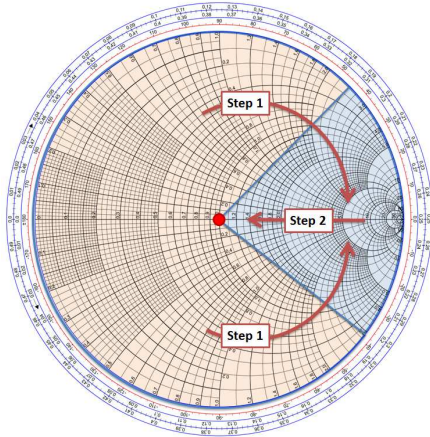
Input data: Reflection coefficient amplitude.

Summary: The minimization of the reflection coefficient is performed based on its local gradient in the (C_1, C_2) plane.

The second backup algorithm only relies on the reflection coefficient's phase as feedback. As no knowledge is available about the quantity to be minimized, being the magnitude, special care should be taken when performing the impedance matching. The developed algorithm is based on a two-step process, which first modifies the reflection coefficient's phase, bringing it into a phase-lock region, after which reflection coefficient's amplitude can be minimized. Indeed, at the system set up, the observed phase value may be considered a random parameter, uniformly distributed between 0 and 2π . A first step consists of removing this random value by setting it to a predetermined value through proper modification of the two variable elements (Figure 24). Next, the two variable varicap diodes are varied to reach the centre of the Smith Chart. The two capacitors are adapted in a similar way as for the default algorithm, summarized in Figure 16. The first step requires the modification of C_1 and C_2 to reach the phase-lock region. Shunt capacitor C_1 is so modified to select the proper conductance circles in which the reflection coefficient could move by varying the shunt capacitor C_2 . This region is defined as the sector of the Smith Chart between -45° and 45° . A phase lock region located in the left half-plane has been discarded, because we cannot define a unique set of actions on capacitor C_1 to approach the centre of the Smith Chart from this area. Specifically, the value C_1 should be reduced if the reflection coefficient is located outside of the unitary value circle, and it should be increased if the reflection coefficient is located inside the unitary value circle. From within the phase-lock region, we can reach the centre of the Smith Chart, by first reducing C_1 , while adapting C_2 to maintain phase lock.

The lack of the magnitude of the reflection coefficient as input data for the algorithm has an impact also on the definition of a stopping criterion. When fixing the angular sector for the phase lock on the Smith Chart, we must consider that, when approaching the centre in the second phase of the algorithm, the closer the actual reflection coefficient comes to the centre of the Smith Chart, the easier it is to exit from the above-defined angular sector. Therefore, nearest neighbour check is performed to

evaluate the proximity to the centre of the Smith Chart. The width of sector angle and the step variation on the capacitance represent a trade-off between convergence speed and precision for the impedance matching.



Backup Algorithm #2

Input data: Reflection coefficient phase

Summary: The minimization process proceeds in two different phases. In the first step, the reflection coefficient value is led into the phase-lock region, being an angular region on the Smith Chart. In the subsequent step, the reflection coefficient is reduced towards the centre of the Smith Chart. The definition of an angular region is needed to be able to control the proximity of the reflection to the centre of the Smith Chart, given that amplitude information is unavailable.

Figure 24 - Description of the Phase-Based Backup Algorithm.

The list of all the software routine developed for the final software architecture with a short description is here reported.

- **Void setup ()**
The setup() function is called when the Arduino sketch starts. It is used to initialize variables, pin modes, using libraries, etc. The setup function will only run once, after each power up or reset of the Arduino board.
- **Void loop ()**
After the execution of the setup() function, which initializes and sets the initial values, the loop() function loops consecutively to actively control the Arduino board.
- **void init_Serial ()**
The init_Serial() function is used to initialize the serial port between the Arduino and a PC. Using the Serial port is it possible to fetch data from the Self Tuning network in order to be measure the performance of the system.
- **void init_dac ()**
The init_dac() function is responsible to the initialization of the external Digital to Analog Converter. It sets the communication pins and other transmitting parameter.
- **void algorithm ()**
Algorithm() is the core of the system, this part is responsible to decide the action to be done in the impedance matching making the matching dynamically possible.
- **void init_variable ()**
Init_variable() is used to initialize all the system variable that would be used during the execution of the program
- **void change_C1 (float control1)**

Change_C1(float control1) function changes the reverse voltage of the varicap diode C1 applying the modification stated by the float variable control1 by calling the function write_DAC().

- void change_C2 (float comando2)
Change_C2(float control2) function changes the reverse voltage of the varicap diode C2 applying the modification stated by the float variable control2.
- void write_Control_Register ()
write_Control_Register () function is executed at the beginning of the software execution and set the working functioning of the external DAC
- write_DAC (int num_dac,int num_out)
write_DAC (int num_dac,int num_out) function write on the “num_dac” output of the external DAC the specific value. It writes the corresponding register inside the external DAC register.
- void Conversion (int number_value)
Conversion (int number_value) converts an integer value in a binary value on 12 bit.
- void Read_Input()
Read_input() reads the value from the AD8302 and transform them in integer number correct by the bias estimated during the calibration process
- void init_ADC()
The init_ADC() function initializes the ADC internal in the Arduino by settings the transmitting rate.
- void check_step()
The check_step() function is used to accelerate the convergence progress by dynamically changing the output voltage step value used to change the reverse voltage. A smaller step size is used while approaching to the center of the chart.
In case of use of only phase algorithm, the step value is set to the minimum value.

1.6 Test and Measurement results

1.6.1 System Calibration

A first consideration should be done on the calibration process once the system has been built. Sure enough the gain/phase detector doesn't make a direct measure of the reflection coefficient but it evaluates a biased quantities. This is caused, for example, by the deployed Directional Couplers that don't present the same coupling factor and have an insertion loss different from zero. Moreover, the cable length needs to be considered since the direct and the reflected wave don't experience the same path inside the self-tuning network as summarized in Figure 25.

The transmitter sent a beacon signal P_{IN} , this signal pass through the first directional coupler. The signal is coupled by a coupling factor C_1 to form the direct wave available to the AD8302. After the first directional coupler, the signal passes through the other directional coupler being attenuated by its insertion loss and the cable loss. Hence P_D is the power that reaches the load. Part of this signal will be reflected according to the actual reflection coefficient and will be collected by the second directional coupler to represent the reflected wave.

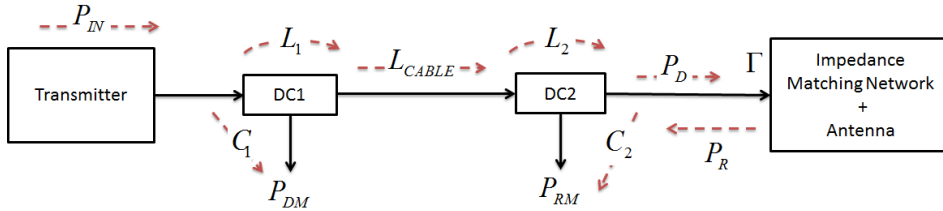


Figure 25 - Model Considered for the Prototype Calibration

The identified bias values have been evaluated experimentally using the measurement setup depicted in Figure 26, when the output impedance where modified by a reactive variable load. The measured and the theoretical input/output characteristics are shown in Figure 27, while the measured bias correction values are reported in Table 7.

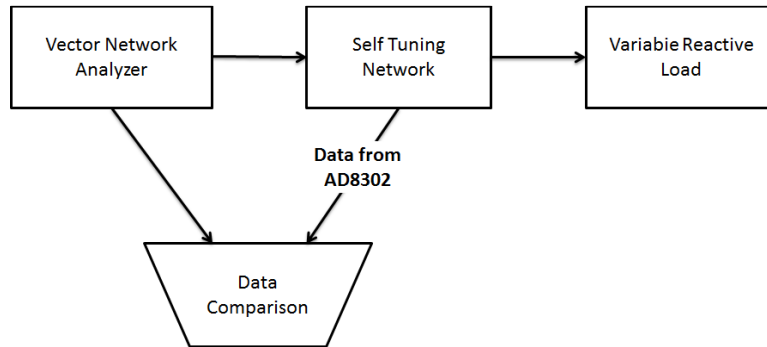


Figure 26 - Measurement Setup for the System Calibration

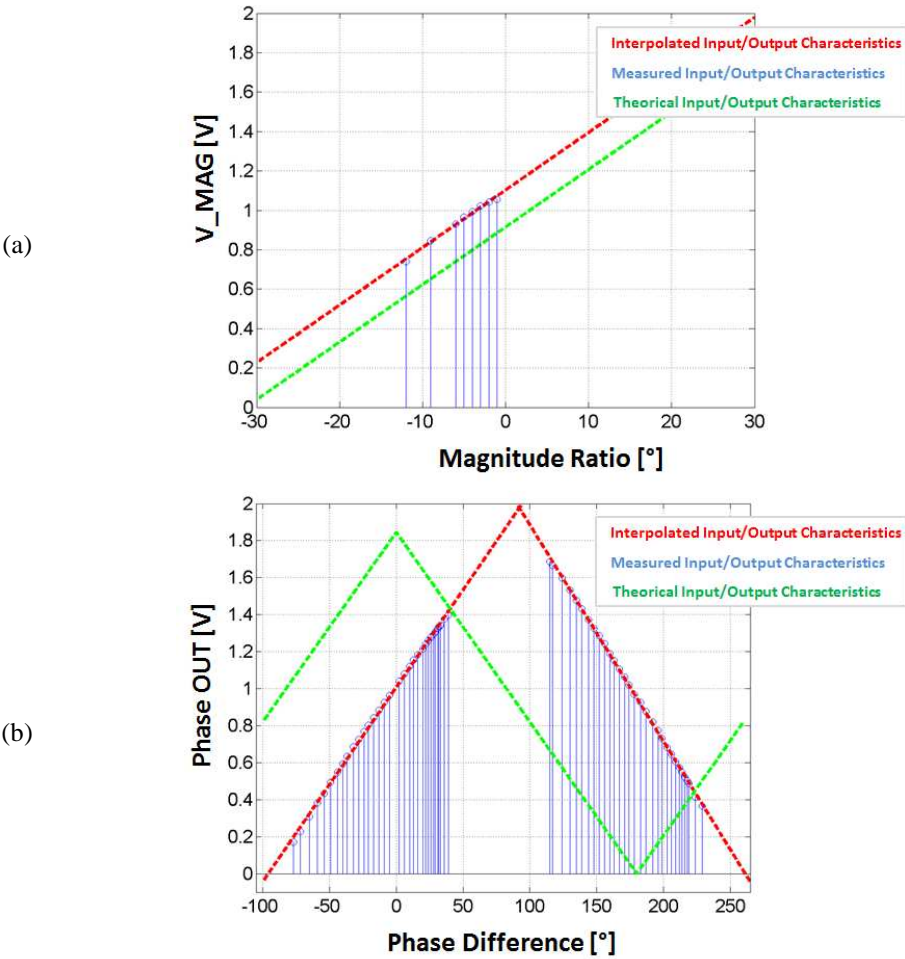


Figure 27 - Measured VS Simulated input/output characteristics of the prototype: (a) absolute value characteristic and (b) phase characterization.

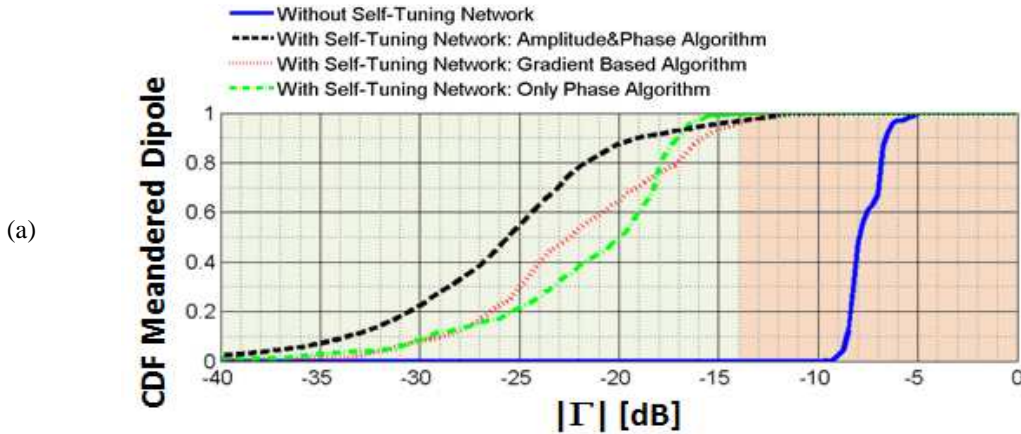
TABLE 7
BIAS CORRECTION VALUE

Absolute Value	+6.44dB
Phase	-79°

1.6.2 System Validation

To validate and test the realized prototype, a wearable Cospas-Sarsat meandered dipole antenna and a wearable Cospas-Sarsat bow-tie antennas [6] have been connected to a Cospas Sarsat user terminal. The main characteristics observed during the validation of the system prototype are the insertion loss of the impedance matching network and the input impedance of the transmitting element. On the one hand, the loss analysis is important because large losses cause a significant performance degradation of the overall system, limiting the benefits of the self-tuning network. On the other hand, the reduction of the reflected power at the antenna input improves the probability of successful transmission by the distress beacon during an emergency situation.

During the tests, the Cospas-Sarsat system prototype was worn by a volunteer who performed a series of random movements. Improvements in terms of reflection coefficient are evaluated by comparing the measured antenna reflection coefficient with and without the self-tuning network for all three developed algorithms. 600 samples of the reflection coefficient were collected for 5 minutes. The cumulative density functions (CDF) of the collected data are shown in Figure 28 and Figure 29, for different cases. The improvements introduced by the self-tuning network are visible in terms of a reduced mean value of the reflection coefficient, decreasing from -8.4dB (in case of the meandered dipole) and -9.5dB (for the Bowtie antenna) to below -20dB for all the algorithms and for both antennas. Figure 28 and Figure 29 clearly show that, by applying self-tuning, the reflection coefficient now meets the specification of being below the reference value of -14dB in almost all circumstances. Indeed, when the meandered antenna is worn by a volunteer, the matching requirement is never satisfied without matching network, whereas with tuning circuit the requirements are fulfilled during 95% of the time. For the bowtie antenna worn by a person, the reflection coefficient is lower than -14dB for the 87% of the time (11% without the tuning network) for any of the three algorithms. Similar results were obtained when the antenna is deployed in proximity of water. Starting from a situation in which the -14dB criterion was not fulfilled at all, the impedance matching network reduces the Reflection coefficient to below the -14dB threshold in more than 95% of the time, for both antennas and with all three deployed algorithms.



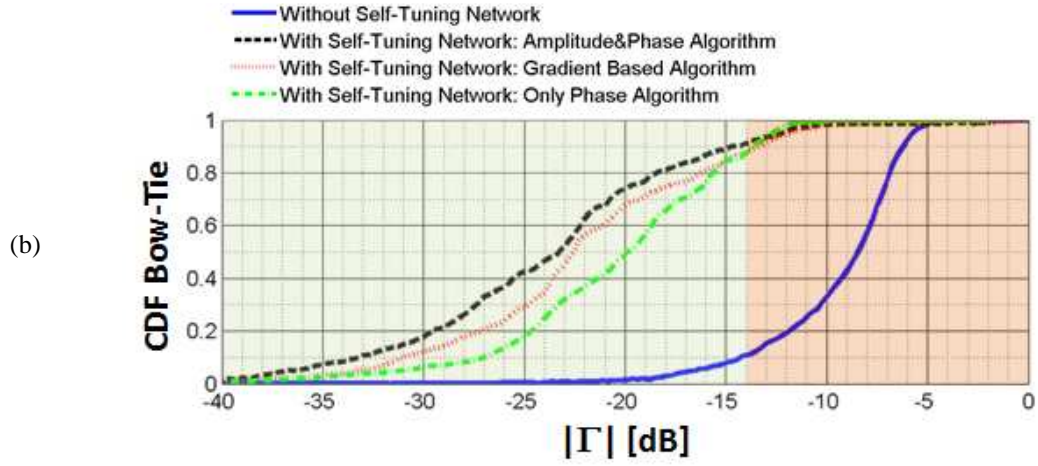


Figure 28 - Measured CDF of the Reflection Coefficient when the antenna was worn by a volunteer: (a) meandered Dipole and (b) Bow-Tie antenna

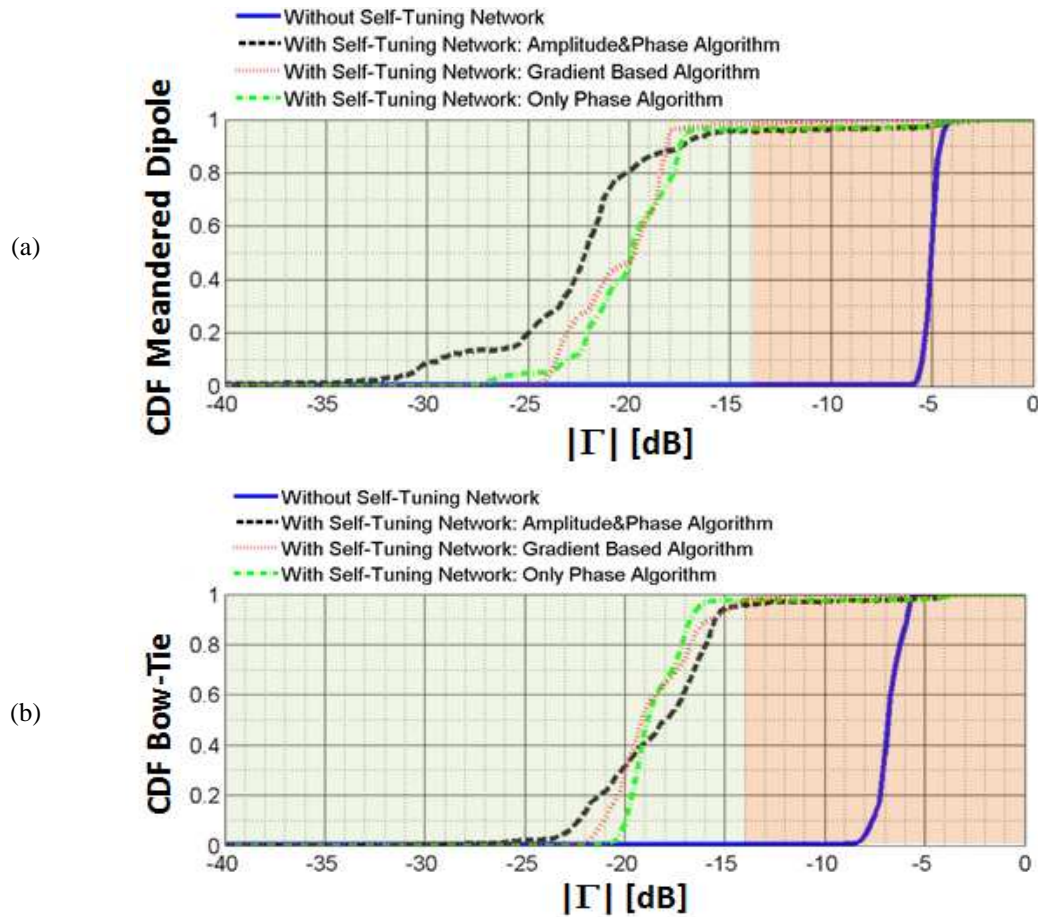


Figure 29 - Measured CDF of the Reflection Coefficient when the antenna is in proximity of water: (a) meandered Dipole and (b) Bow-Tie antenna

In order to validate the resilience of the realized software architecture, several tests were conducted while the input data (amplitude and phase of the reflection coefficient) were dynamically made available or unavailable to the microcontroller by a software enabling system. With these tests, the ability of the software architecture to switch between default and backups algorithms has been proved.

Different combinations of available input data have been tried in different tests. In Figure 30, an example of collected data over a time span of 60 seconds is shown. At the system start-up, both absolute value and phase of the reflection coefficient were available as input data to the microcontroller. During this time frame, the default algorithm was applied to achieve the impedance matching. Later on, the phase link was interrupted for 12 seconds before being restored, causing the microcontroller to switch from the default algorithm to backup algorithm #1, and back. The switch between the default algorithm and the backup algorithm #2 was tested in the last part, by interrupting the magnitude link information. The latter was interrupted for 12 seconds before being restored. With these actions, all the possible paths shown in the flow chart in Figure 21 have been explored.

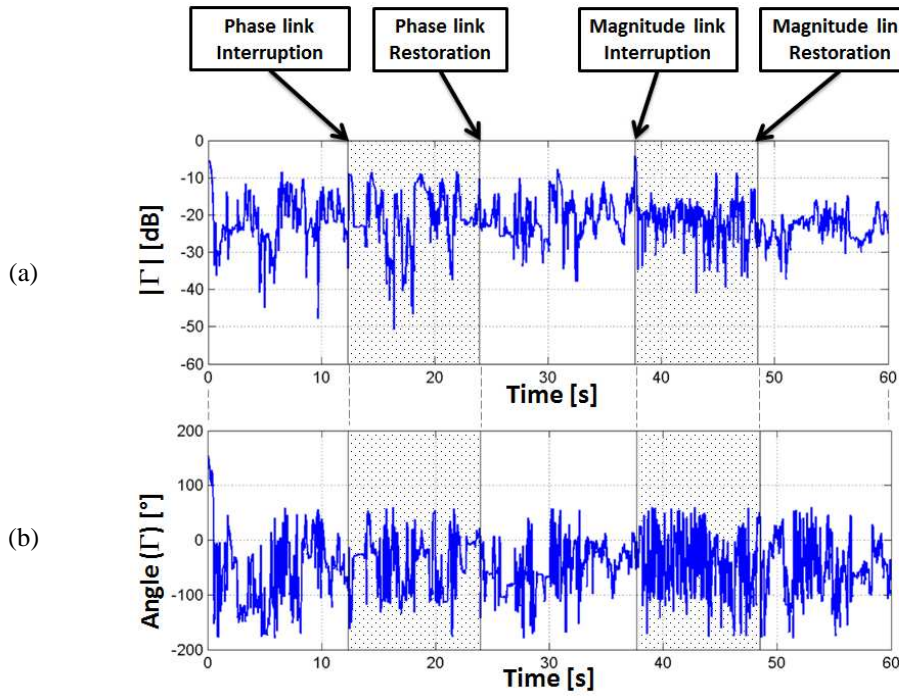


Figure 30 - Measurement of the Reflection Coefficient when the antenna was worn by a volunteer during failure emulation: (a) absolute value and (b) phase value.

With this time domain analysis, the reaction of the software architecture in response of changes in the physical circuit is demonstrated. Moreover, a deeper time domain analysis permits to appreciate and to better understand the working principles of the different algorithms.

Indeed, by enlarging the time scale at the system start-up and observing the first output data of the reflection coefficient on the Smith Chart it is possible to appreciate the adaptation process of the default algorithm (Figure 31). In this case, at the system start-up the reflection coefficient is located in the region #2. By adapting both variable capacitors, we first lead the reflection coefficient to the

unitary admittance circle (where capacitor C_1 is responsible for compensating for the real part of the admittance), which is then directed to the centre of the Smith Chart (by varying capacitor C_2 to compensate for the imaginary part of the admittance).

We now discuss backup algorithm #2, which only uses the phase of the reflection coefficient for the impedance matching. By concentrating on the measurements performed around time instant 38s, we can observe the two initial steps previously described. The developed algorithm requires a preliminary phase, where the phase of the reflection coefficient is led to a phase-lock value, followed by the main phase, where the reflection coefficient is moved towards the centre along the lock angle. This characteristic can be observed in Figure 32. In the dashed part, the microcontroller is leading the phase towards the lock value, whereas in the dotted part the reflection coefficient is lead towards the centre of the Smith Chart along the lock-value phase.

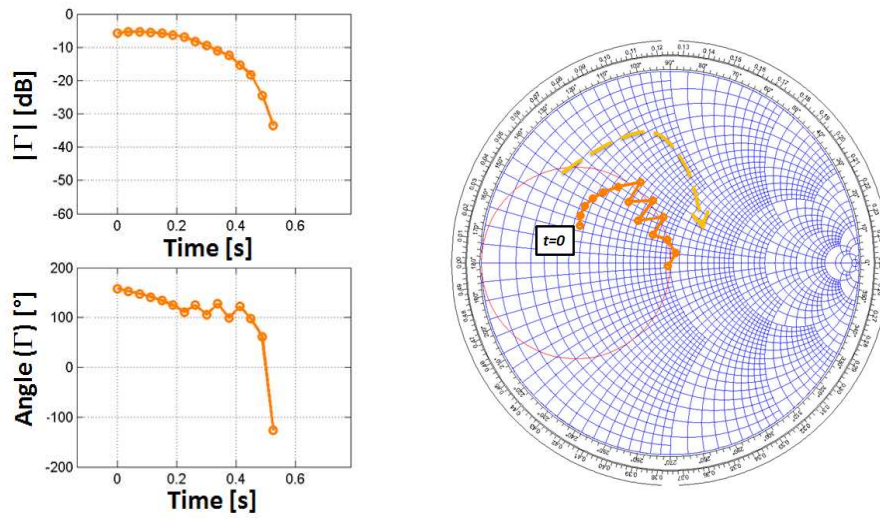


Figure 31 - Detail of the measured reflection coefficient during the automated tuning procedure using the default algorithm.

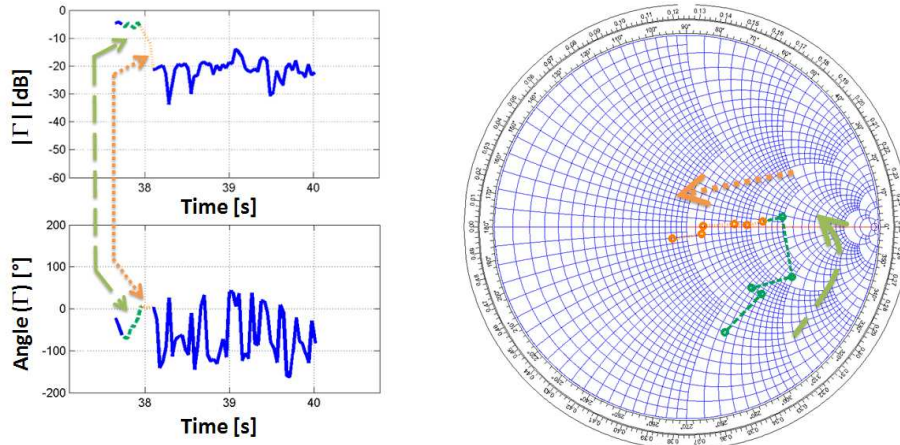


Figure 32 - Detail of the measured reflection coefficient during the automated tuning procedure using the backup algorithm#2
(Only phase information available to the microcontroller)

All algorithms exhibit a convergence time that basically depends on the initial position of the reflection coefficient in the Smith Chart. Yet, algorithms and antennas we tested, converged to a reflection coefficient below -14dB within a time frame of 300ms. After matching is obtained, the system is able to maintain the reflection coefficient value below -14 dB during more than 99% of the time within a 5 minutes' time span, when the antenna was worn by a volunteer performing random movements, as depicted in Fig.13. Also in those cases in which the reflection coefficient increases to values above -14dB, due to the wearer's movements, all algorithms adapt and achieve matching again in a few 100ms. The measured convergence time and response time is considered adequate for being applied to a Cospas-Sarsat system when a half-second burst is transmitted approximately every 50 seconds. Based on the collected results, the first burst could be transmitted after half a second from the system start-up, in order to ensure that the system achieves matching after being initiated. For the following bursts, the probability of having transmission during an antenna mismatch condition is lower than 1%. To enlarge the life span of the system even more, the self-tuning network could be switched off and turned on only a few seconds before signal burst transmission.

The measured insertion loss is around 1.9dB. This value is mainly attributed to the applied wideband directional couplers, which have a total insertion loss of 1.8dB. The use of dedicated narrowband direction couplers could reduce the total insertion loss of the self-tuning circuit, thereby improving the overall circuit efficiency.

1.7 Conclusion

A self-tuning network for a wearable Cospas-Sarsat transmitting system has been designed, built and tested. The realized low-cost self-tuning network is able to estimate the actual reflection coefficient and to tune a dedicated impedance network accordingly by a dedicated robust software architecture. The system increases the probability of correct distress beacon signal transmission in harsh operating conditions by ensuring that the Cospas-Sarsat requirements remain satisfied at all time. The tuning network relies on varicap diodes, whose capacities are modified in real-time based on the antenna's measured reflection coefficient. The matching process is executed by adaptively controlling the tuning network parameters. Three different algorithms were implemented that rely on different feedback information from the gain/phase detector. Although all three algorithms can individually perform the impedance matching, the realized default/backup software architecture improves the reliability of the wearable device when deployed in an emergency situation. Moreover, the generic software architecture implementing the backup algorithms described in this chapter can be applied in conjunction with many low-cost off-the-shelf components that do not provide both the amplitude and phase of the reflection coefficient, but only one of the mentioned quantities. The system may be connected to different wearable Cospas-Sarsat antennas, making it suitable for integration into a commercial life-jacket. It has been experimentally shown that detuning of antenna's resonance frequency due to the antenna-body interaction and the wearer's natural movements can be effectively compensated, limiting the antenna's reflection coefficient to below -14dB, as requested by the Cospas Sarsat specification.

2 Wearable Active Sierpinski Fractal Antenna for Off-Body Communication

2.1 Introduction

In this chapter, the design, realization and validation of a low cost, easy to realize, light-weight, compact UHF reconfigurable textile wearable antenna for direct integration into garment is presented. The antenna implements off-body communication in the 868MHz and 915MHz Industrial, Scientific and Medical (ISM) bands. The wearable Sierpinski fractal bow-tie antenna is tuned to the appropriate operating frequency by a dynamic reconfigurable impedance matching network. Varicap diodes dynamically adapt the antenna feed structure to set the correct antenna resonance frequency at all time. In the process, the adaptive feed network compensates for detuning of the RF system due to interaction between the antenna and the human body.

A prototype of the antenna with the adaptive feed structure has been realized and tested when the system was worn by a volunteer. Tests have been performed with a volunteer performing several random movements to replicate a dynamic situation for both frequency bands of operation.

This chapter is organized as follow. First the motivations behind the needed of developing a so called wearable antenna will be discussed. After a brief general description of the actual state of the art, the design and the antenna concept will be presented. Measured performance results will be shown in terms of reflection coefficient and in terms of radiation pattern, thanks to the collaboration with the Department of Information Technology (INTEC) of the Ghent University, Belgium [33]. Finally, several conclusions will be drawn.

2.2 Motivations

During the past years, the interest for wearable devices has rapidly grown. Wearable devices are now used in several applications, such as in search and rescue operations [34], in military missions, in e-health monitoring, in mobile computing and for public safety purposes [35].

To achieve market penetration, wearable devices must be low cost components enabling unobtrusive integration. To fulfil these requirements, if a wireless communication link is required, particular attention should be devoted to the realization of the wearable device's RF section.

Sure enough, when designing an antenna directly integrated on garment using the textile technology, several precautions should be taken into account. A textile antenna should respect both specific electromagnetic requirement and specific mechanical requirement.

In addition to the traditional requirement of resonance frequency, bandwidth, overall efficiency and radiation pattern, a textile antenna needs to respect also several mechanical requirements due to the integration directly on textile surface. A good wearable antenna must both be comfortable to wear and perform well in the communication link. The structure must be flexible, and thick or rigid padding must be avoided. If the antenna is large, it also has to be breathable. The antenna must withstand washing and wear, and should be resistant to moisture. In order to be truly wearable, the antenna must have a low profile, which means that it should conform to the body and not protrude from the clothing. As a part of the communication link, the antenna should be as efficient as possible, and meet the specifications for the impedance and radiation properties. Most importantly, the link must operate reliably, especially in life-saving applications.

To fulfil all of these requirements, a fractal shape, an active control circuit and the textile technology have been combined.

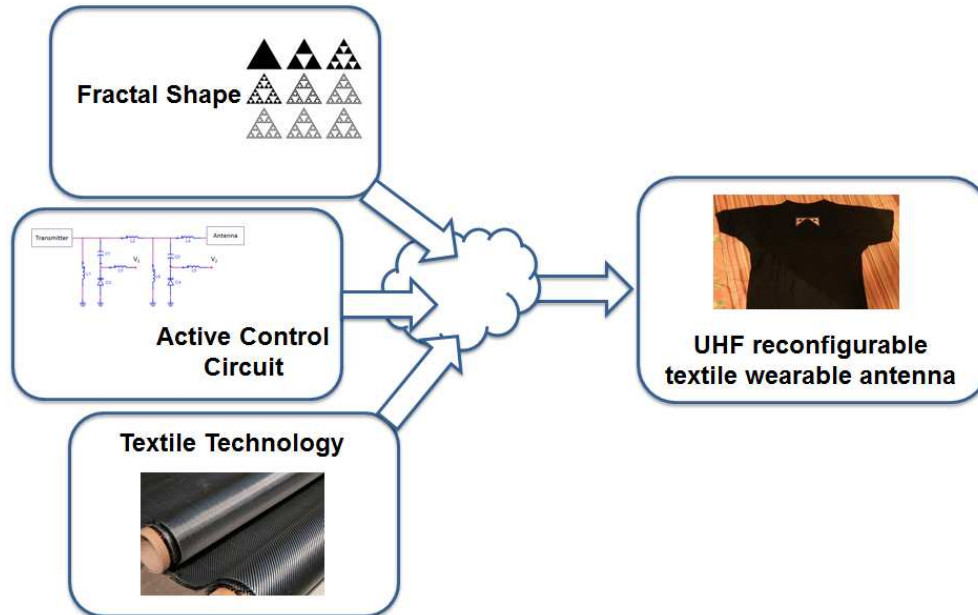


Figure 33 - Combination of the fractal shape, the active control circuit and the textile technology to realize an UHF reconfigurable textile wearable antenna.

2.3 State of Art

The area of textile antenna research is an active one, many researchers are drawn to the potential of textile antennas for wearable systems and a plethora of designs can be found in literature. This section summarized the main research efforts and advancements made in antenna textile development [36].

A first reported “all textile antenna” was presented in 2003 [37] and has a microstrip patch topology build up using a fleece substrate and knitted copper fabric (Figure 34). It operates in the 2.45GHz Industrial and Scientific (ISM) band and it is intended for Bluetooth or wireless LAN applications. Since then, the research efforts in the field of textile have significantly broadened to cover all the aspects of design.

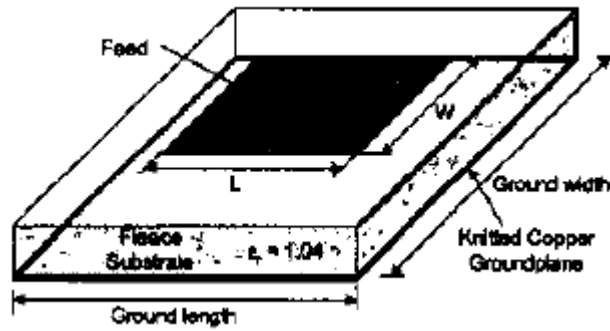
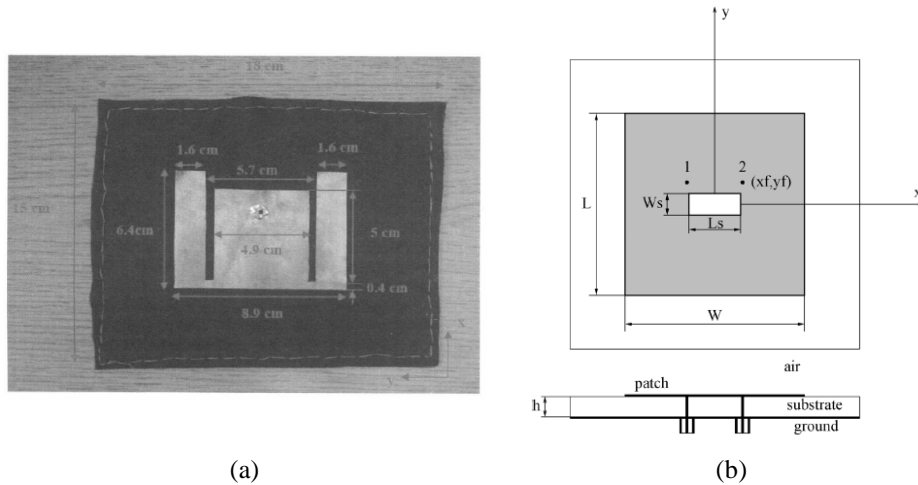


Figure 34 - Antenna design proposed in [37]

The first antennas typically exhibited single band operation, but in the meantime researchers have conceived designs with multiband [38]-[41], and ultra-wideband functionality [42], [43]. Vertical polarization is often reported, but dual polarized [44]-[46] and circularly polarized designs [47], [48] dedicated for on-body use also exist. Some design focus on topologies with small dimensions, [49] or use Electromagnetic band Gap (EBG) structures, [50] to improve body antenna isolation. Some of these proposed solutions are shown in Figure 35.



(a)

(b)

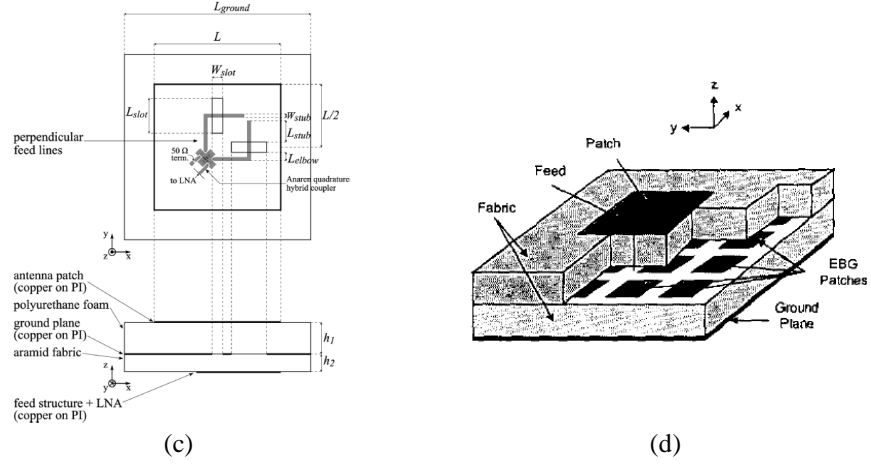


Figure 35 - Different design solution for a wearable antenna: (a) multiband antenna proposed in [38], (b) dual polarized antenna proposed in [44], (c) circularly polarized antenna proposed in [47], (d) solution with an Electromagnetic Band Gap proposed in [50]

Different studies have also specifically done on external influences that might pose problems for decent antenna operation (Figure 36) such as the presence of human body,[51], bending, [52], [53], washing [54], [55], environment condition (humidity [56], harsh environment [57], shot gun blast [58]), when integrated into and covered by textile layer, [59]-[61], and their sensitivity to fabrication tolerances [62].

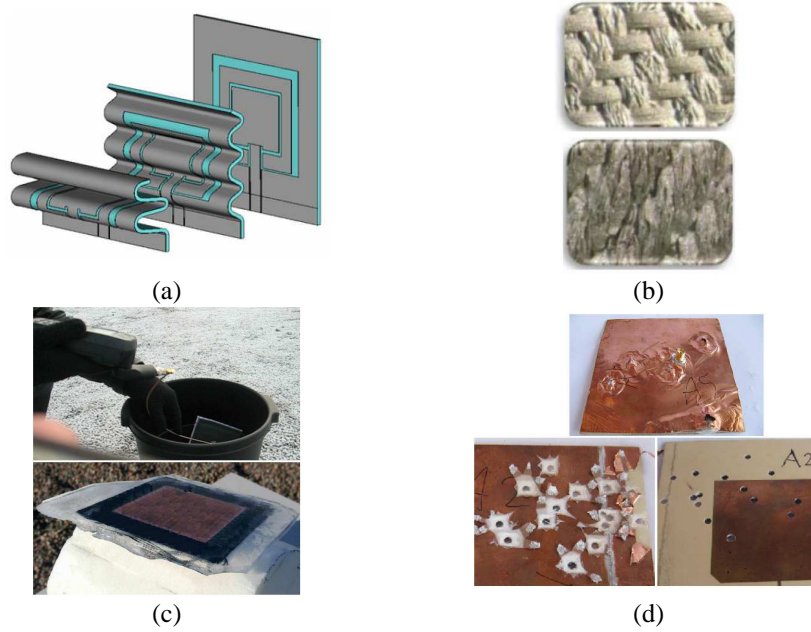


Figure 36 - Stress test carried out for a wearable antenna: (a) bending in [49], (b) washing in [55], (c) harsh environment with water or ice in [57], and (d) shotgun blast in [58].

Since a stand-alone antenna is of not much use, strategies to integrate active circuitry with textile design have been researched (Figure 37). In [63]-[66] electronics parts are integrated behind the ground plane of a patch antenna by using a very thin polyimide layer as a carrier for the electronics, or [67] where a solar cell is mounted on an antenna for energy harvesting.

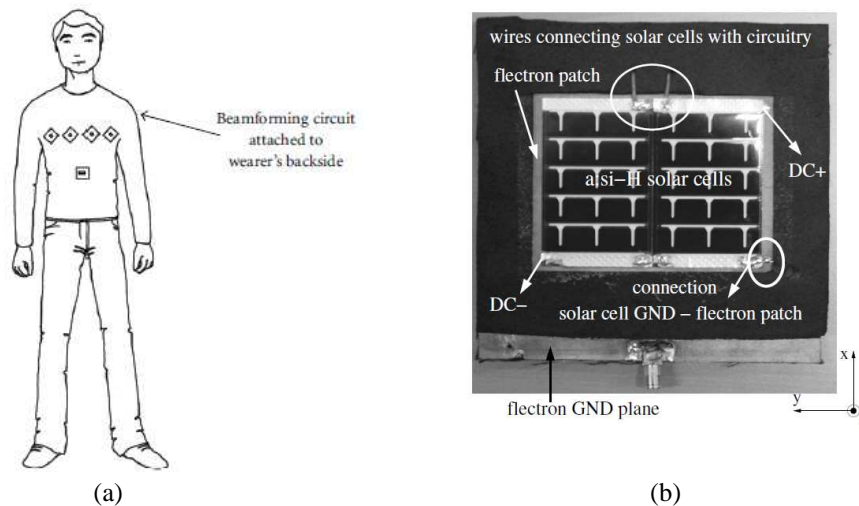


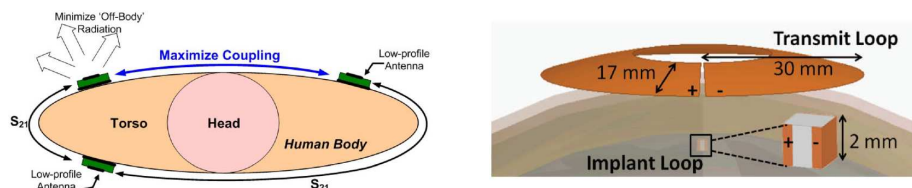
Figure 37 - Wearable antenna with active circuitry: (a) Beamforming circuit proposed in [63] and (b) antenna with an energy harvesting solar panel integrated [67]

Most textile antennas that can be found in literature have been optimized for specific purposes as shown in

Figure 38. As an example, the radiation pattern can be direct away from the wearer, and thus they are excellently suited for what is called off body communication: data transmission from a body worn device, to wireless system not physically connected to the wearer. Some antenna designs realize radiation patterns with maxima along the human body. These designs [68]-[70] are excellently suited for transmission between nodes on the human body. In other studies designs were developed to improve the communication link to implant devices, such as in [71]-[73].

Textile antenna can also be used in array formation to achieve better communication link, or longer range [74]-[77].

The operating frequency of most of the discussed designs is lower than 6GHz, mainly focusing on the 2.45GHz band or the frequency bands allocated to Global Satellite Navigation System (GNSS) (such as Galileo, GPS), but antennas for the 60GHz band have also proposed [78]. Yet they tend to suffer from poor efficiency, mainly caused by the reduced conductivity at these high frequencies and roughness of the e-textiles.



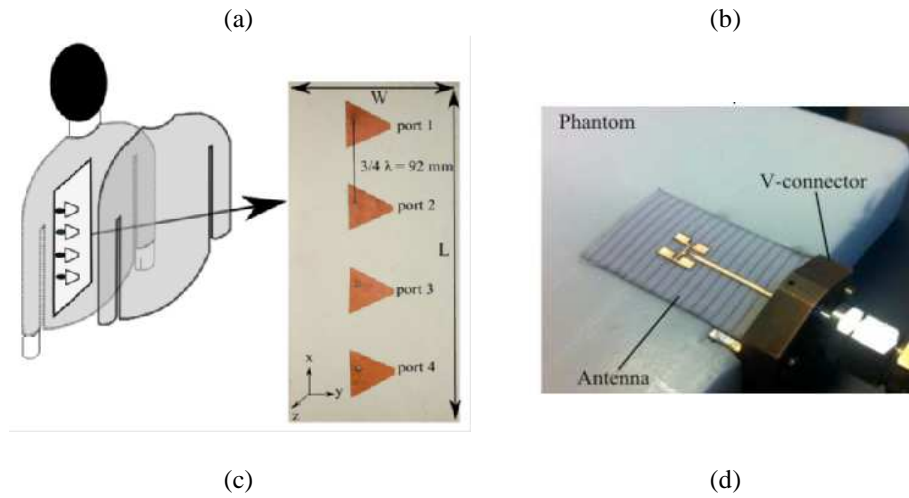


Figure 38 - Wearable antenna design adapted for a specific purpose: (a) maximization of the radiation pattern along the human body proposed in [69], (b) maximization of the intra-body communication link in [72], (c) array disposition to achieve a long off body link in [76] and (d) deployment in the Ka band [78].

The designs discussed so far have all been implemented in micro strip line or coplanar waveguide topologies. These two implementation techniques have the advantage that they are low profile, easily realizable on textile materials, and that designs can be realized in such a way that they have good body-antenna isolation, which is vital for robust, energy efficiency, and safe textile antenna operation.

2.4 Antenna Design

This section is divided into three different subsection aims to described the three fundamental blocks that have been briefly introduced in section 2.2. These three blocks are the Fractal Geometry design of the antenna, the active electronic circuit and the e-textile technology. These three different blocks create the *Active Sierpinski Fractal Antenna for Off-Body Communication*.

The fractal shape has been used to miniaturize the antenna. The adoption of a tuning network allows the selection of the operating frequency and permits to compensate the reflection coefficient detuning due to its proximity to the human body. Finally, the e-textile technology has permitted the integration on the garments.

2.4.1 Fractal Geometry Design

The Sierpinski triangle is a fractal shape created by a polish mathematician in 1916. A Sierpinski triangle can be created by the application of a recursive algorithm on a triangular shape. The first step is to subtract a central inverted triangle from the main triangle, yielding three identical sub-triangles (Figure 39). The same subtraction procedure can be repeated on the remaining triangles to progressively obtain a higher number of triangles. In every iteration, all the obtained triangles keep the same structure as the initial triangle, but scaled by a factor of two. Thanks to this property, the Sierpinski fractal is a self-similar structure [79]. In our design, we have adopted this fractal owing to its affinity to a bow-tie antenna.



Figure 39 - Different stages of the Sierpinski triangle fractal, obtained by iterating the algorithm of triangle subtraction

First, several simulations were performed to determine the optimal number of iterations of the Sierpinski fractal to satisfy the requirements listed in 2.2.

Simulations were limited to the first three orders of the fractal shape, starting from a bowtie antenna optimized for 868 MHz (Figure 40), both in free space and in proximity of the human body, which was modelled following the guidelines described in [80] and the geometry depicted in Figure 41. The principal simulating parameter deployed for the simulations are collected in Table 8.

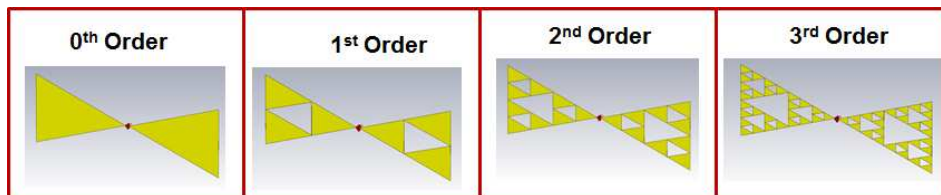


Figure 40 - Selected candidates shapes to be the final shape of the textile antenna

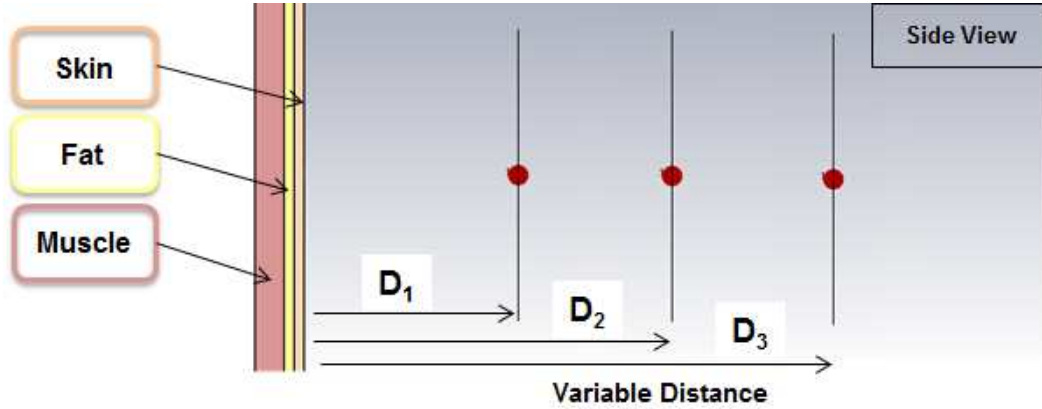


Figure 41 - Side view of the geometry for the simulations of the different antenna shapes proximity of the human body

TABLE 8
PRINCIPAL SIMULATION PARAMETERS

Tissue	Thickness [mm]	Conductivity [S/m]	Relative Permittivity	Loss Tangent
Skin	3	1.60	42.8	0.27
Fat	3	0.11	5.3	0.14
Muscle	6	1.74	52.7	0.24

Several simulations have been performed in order to establish the final shape of the radiating element.

On the one hand, simulations performed in free space highlight that no significant variation in the resonant frequency is found when changing the antenna geometry, as shown in Figure 42. On the other hand, simulations performed in proximity of the human body (Figure 43) demonstrates that the use of a fractal shape enables miniaturization of the antenna, given the decrease in resonance frequency for higher fractal orders.

The final topology was selected based on a trade-off between the realization complexity and degree of miniaturization. The first and second order iterations realize the largest miniaturization. However, the first-order geometry has a lower complexity compared to the second-order shape, as only one triangle should be removed from the initial bowtie shape. Moreover, the first order iteration can also provide higher mechanical resilience compared to the second-order shape when the wearable device is subjected to different types of stress mechanisms (such as bending, ironing or washing). In these conditions, the thinnest parts of the antenna (being the vertex of each internal triangle) represent a threat to mechanical robustness. By limiting these weak points, the overall resilience can be improved.

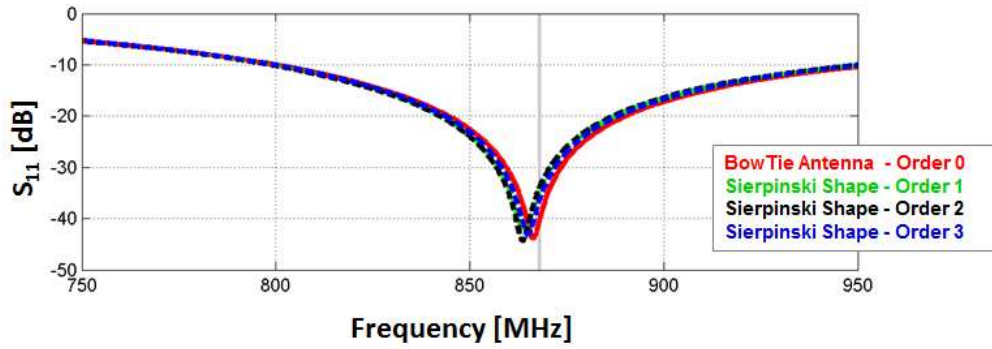


Figure 42 - Simulated Reflection Coefficient for different Sierpinski fractal shapes in free space

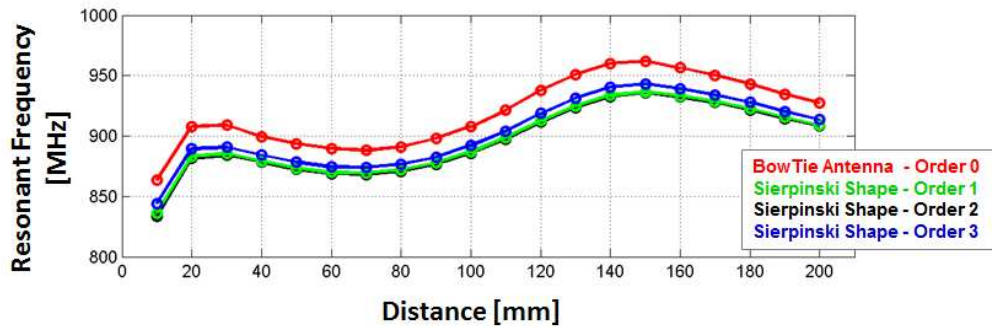


Figure 43 - Resonance frequency versus distance from the human chest, for different Sierpinski fractal antenna shapes

Finally, the shape of the antenna was modified to make room for the tuning circuit described in 2.4.2 without changing the overall occupied area. Therefore, the triangles composing the antenna were slightly moved, going from an acute shape (the light orange part in Figure 44) to a rectangular shape (the dark orange part in Figure 44). Simulations performed on this final shape meet the design requirements previously described.

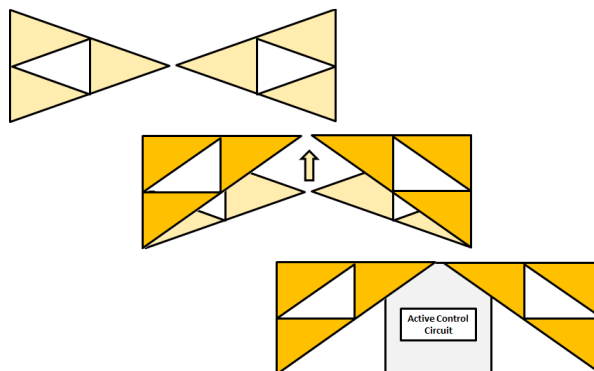


Figure 44 - Final modification of the Sierpinski fractal antenna

2.4.2 Active Control Circuit

The second ingredient of the “Wearable Active Sierpinski Fractal Antenna for Off-Body Communication” recipe is the active control circuit.

This element is responsible to control the detuning of the antenna due to the presence of the human body and its movements. It is also responsible to change the resonant frequency of the antenna, making it working for both the desired ISM frequency of 868 MHz and 915 MHz.

The final schematic of the active circuit is depicted in Figure 45. The selection between the two operating frequencies of 868 MHz and 915 MHz is performed by a proper modification of the reverse voltage applied to the two varicap diodes.

The realized circuit, with the component value listed in Table 9, is shown in Figure 47.

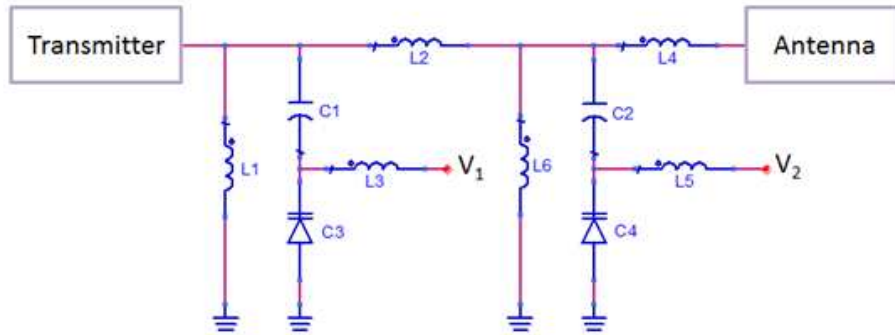


Figure 45 - Schematic view of the tuning circuit

TABLE 9
COMPONENT VALUES APPLIED IN THE TUNING CIRCUIT.

Parameter	Value
L1	33nH
L2	10nH
L3	1uH
L4	13.8nH
L5	1μH
L6	10nH
C1	47μF
C2	47μF

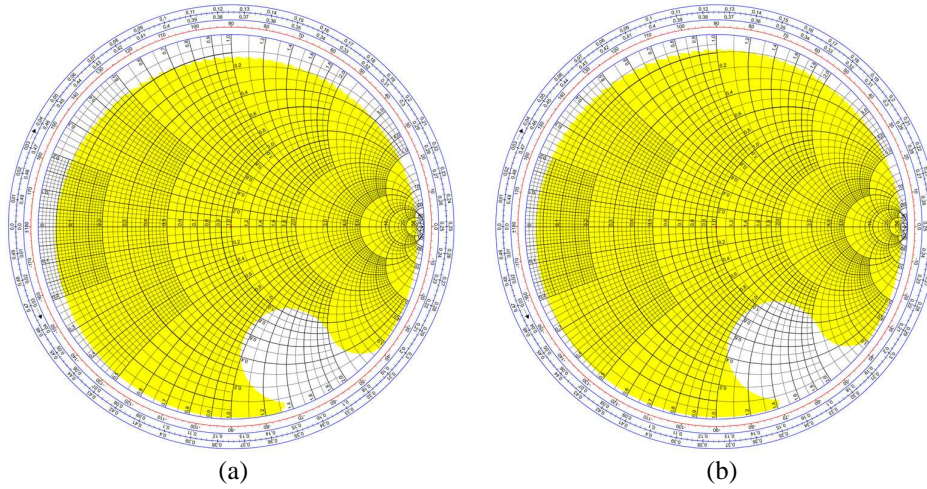


Figure 46 - Simulated Matching Domain for the realized circuit: (a) 868MHz and (b) 915MHz

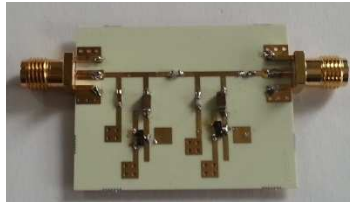


Figure 47 - Realized Active Control Circuit

2.4.3 E-Textile Technology

E-textile technology allows the direct integration of the radiating element on garments.

The fabrication process is depicted in Figure 48. The antenna is obtained by first cutting the shape of the radiating element from a conductive fabric sheet (Figure 48a Figure 48b). Then, the final shape obtained (Figure 48c) is glued to a textile substrate made by aramid with a special glue robust to washing and bending stress.

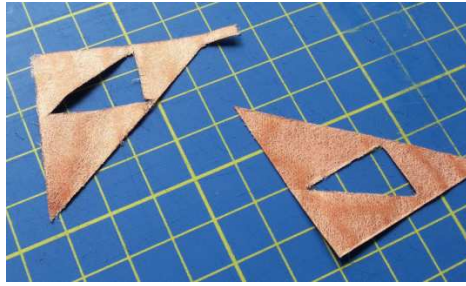
An SMA connector is then soldered on the back of the radiating element to connect it to the other part of the prototype and the measurement instruments.



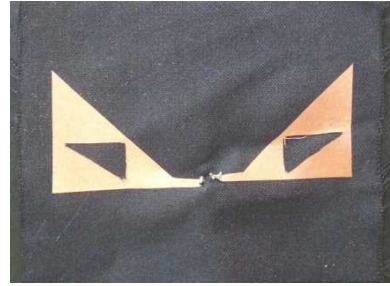
(a)



(b)



(c)



(d)

Figure 48 - Fabrication Process of the wearable antenna: (a) from a conductive sheet, (b) the shape of the antenna is obtained. (c) a special glue is used on the back of the obtained shape. (d) the shape is glued to a textile aramid substrate.

2.5 Measured Result

In this section the measured results performed on the final prototype are presented. Tests have been performed in order to verify that the realized prototype is able to work at the two different ISM frequencies of 868MHz and 915MHz. The system should be also able to compensate the detuning of the radiating element due to the coupling with the human body.

Measurement has been done on the reflection coefficient for both operating frequencies (Figure 49).

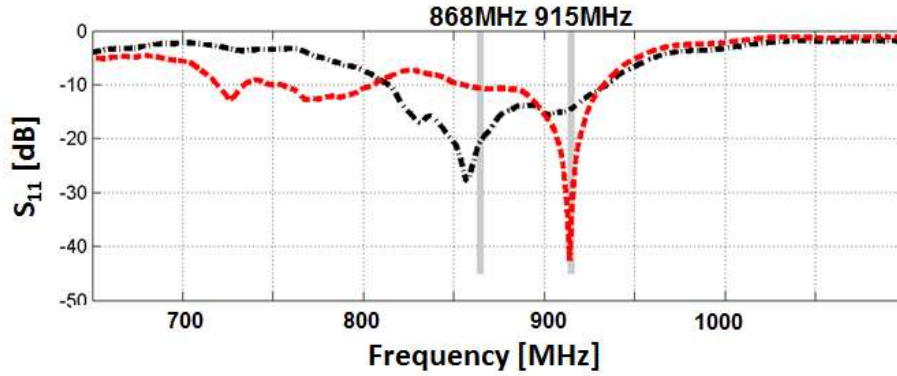


Figure 49 - Measured Reflection Coefficient optimized for the frequency of 868MHz and 915MHz.

Also the radiation pattern has been measured for both identified frequencies using the anechoic chamber at the University of Ghent. Measured 3D radiation pattern is shown in Figure 50 for both frequency (868MHz and 915MHz).

Comparisons between simulated and measured results on the two fundamental planes (Figure 51) are reported in Figure 52 and Figure 53.

Along the plane $\phi = 0^\circ$, the directivity pattern is similar to a section of a doughnut shape, typical of a bowtie antenna. On the contrary, along the plane ϕ constant at 90° the radiating pattern loses its symmetric structure, and there is a preferred radiation direction towards the supply port (toward the top in Figure 51). This asymmetry is introduced by the non-symmetrical design of the antenna, and by the feeding structure. This should be taken into account when deciding on the orientation of the realized antenna after deployment on the body.

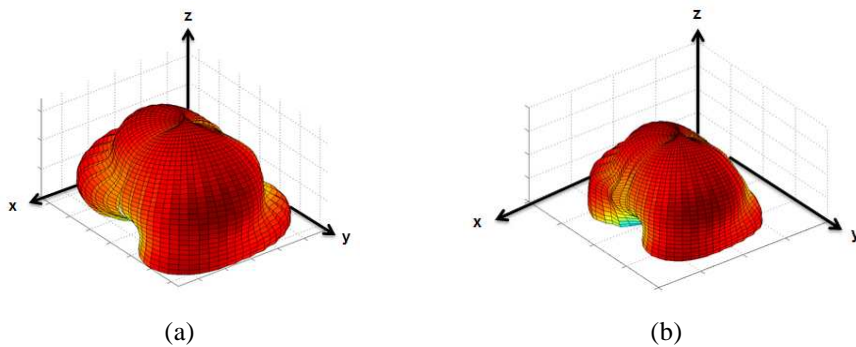


Figure 50 - 3D measured radiation pattern in the ISM bands: (a) 868MHz and (b) 915MHz

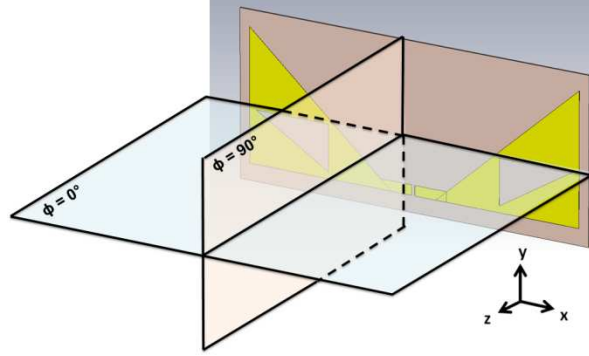


Figure 51 - Principal plane considered in the measurement of the radiating pattern

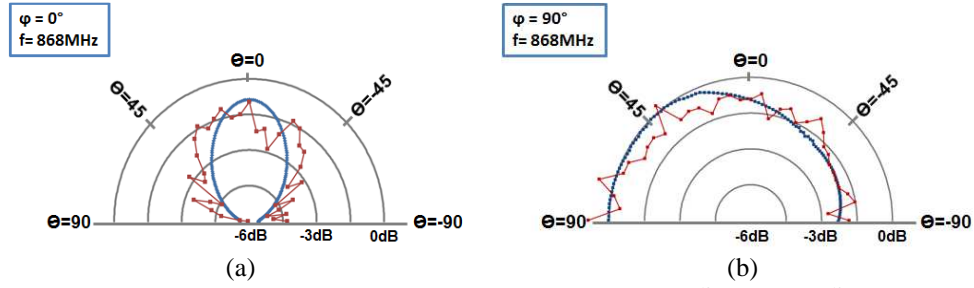


Figure 52 - Radiating Pattern at 868MHz on the principal planes: (a) $\varphi=0^\circ$ and (b) $\varphi=180^\circ$

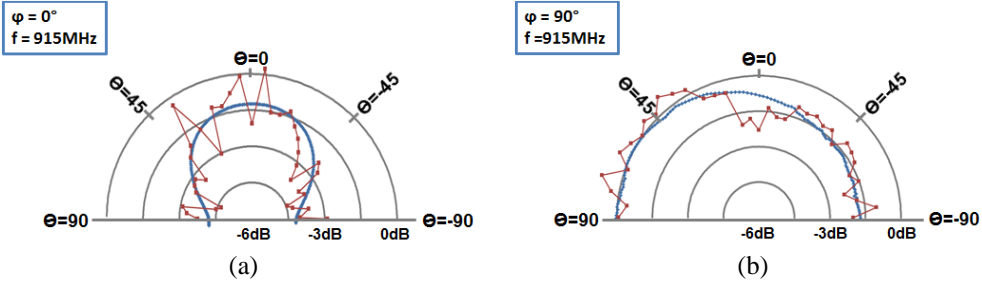


Figure 53 - Radiating Pattern at 915MHz on the principal planes: (a) $\varphi=0^\circ$ and (b) $\varphi=180^\circ$

The wearable prototype has been also compared with a standard bow tie antenna in terms of received power. The measurement setup is shown in Figure 54. A 10dBm signal were injected and were transmitted toward a standard horn antenna (Figure 55) with a gain versus frequency characteristics depicted in Figure 56. The signal communication link was confined inside the anechoic chamber allowing the reduction of multipath components.

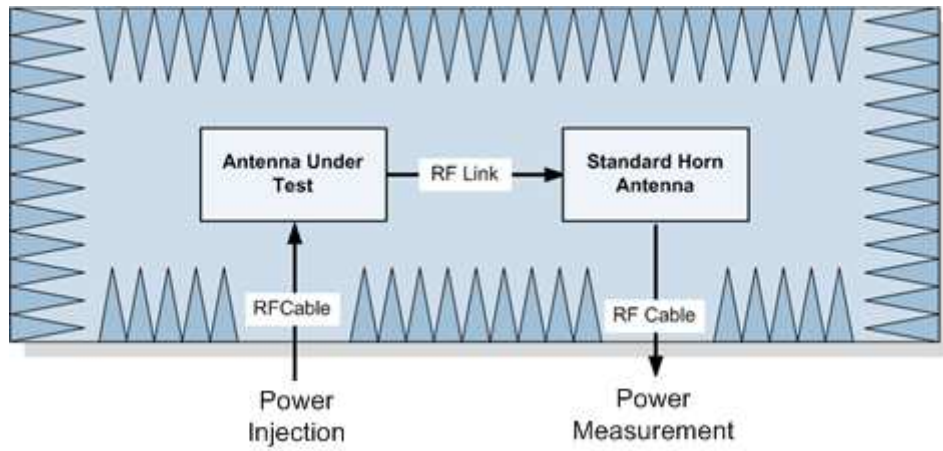


Figure 54 - Measurement setup for the "Power Transmission" Test

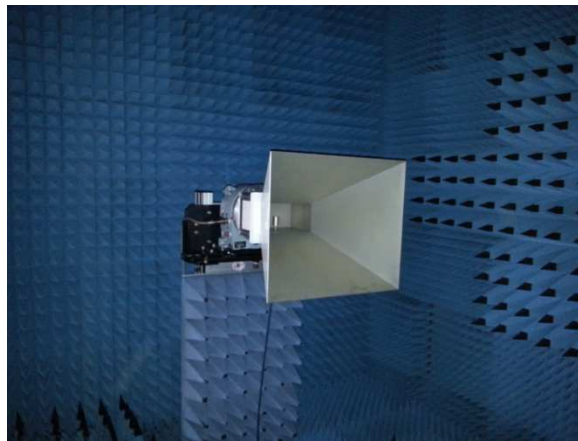


Figure 55 - Standard Horn antenna deployed for the measurement in the anechoic chamber

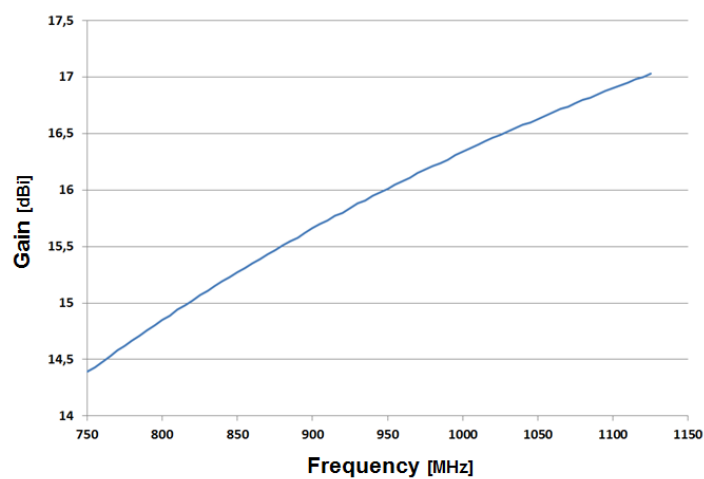


Figure 56 - Gain VS Frequency of the Standard Gain Horn

Measured results are reported in Figure 57. The wearable prototype presents the same performance in terms of received power (so the same gain) of a standard physical bowtie antenna. The gap between the two lines represents the losses introduced by the tuning circuit.

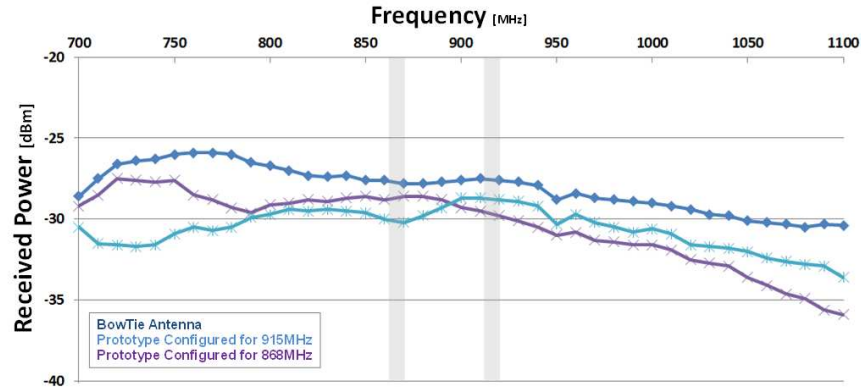


Figure 57 - Prototype adapted to 868MHz

The dynamic compensation for the detuning of the antenna at the two different frequencies while the wearer was performing random movement has been also tested. The reflection coefficient, collected for a time span of 5 minutes, has been treated as a random parameter and its Cumulative Density Function has been evaluated and shown in Figure 58. Measured results demonstrate that the designed system is able to dynamically compensate the variation in the Reflection Coefficient due to the presence and the movement of the wearer.

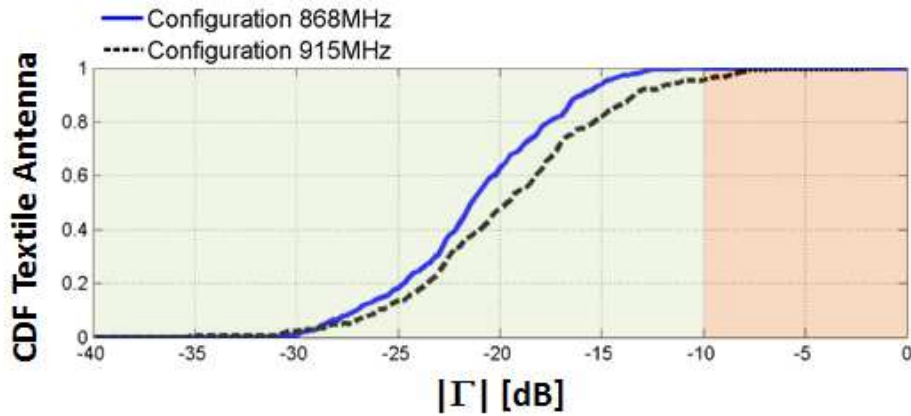


Figure 58 - Cumulative Density function for the realized prototype while the wearer were performing random movements for both 868MHz and 915MHz ISM frequencies.

2.6 Conclusion

A wearable antenna for off-body communications has been designed and realized. Starting from a bowtie structure, a first-order Sierpinski fractal antenna has been proposed in order to meet the requirement of low cost integration and reliability of the wireless link. The antenna's reflection coefficient and the radiating pattern were carefully studied by simulations and measurements. The realized adaptive feeding network controls the resonance frequency of the antenna, enabling operation in both the 868MHz and the 915MHz frequency bands. This selection of the operating frequency is achieved by a feeding structure that dynamically changes the input impedance. The feeding structure is also able to compensate for variations in radiating characteristics of the radiating element due to the presence of the human body.

3 A reconfigurable layout for a self-structuring lifejacket-integrated antenna of a SAR system

3.1 Introduction

In this chapter, a reconfigurable layout to implement a self-structuring wearable antenna for a Search and Rescue system terminal (Cospas-Sarsat at 406MHz) is presented. The proposed antenna layout is intended to be integrated on a commercial life jacket for use in a maritime environment. The shape of the antenna can be dynamically reconfigured by means of RF switches to ensure the best possible transmission conditions, in terms of overall antenna efficiency, even if part of the antenna goes under the sea level. The shape of the components of the self-structuring antenna has been optimized for different antenna positions with respect to the water level and immersion angles.

After a first analysis of the actual state of the art for self-structuring design, the design, the working principles and the simulated results of the identified layout will be described.

3.2 State of art Overview

A self-structuring antenna is a particular type of antenna made of a combination of wires or strips interconnected by controllable switches. This setup enables dynamic changes in the radiating shape to ensure the best of all possible transmission conditions (in terms of overall antenna efficiency). The selection of a particular radiating shape is based on real-time monitoring of the working condition (i.e. measurement of the actual Reflection Coefficient) through a proper algorithm implemented on a microcontroller [81].

Changes in the radiating structure are made in order to regulate the input impedance of the antenna [82], the radiation pattern [83], the polarization [84], [85] or the radar cross section [86], [87].

The typical structure of a self-structuring antenna is shown in Figure 59.

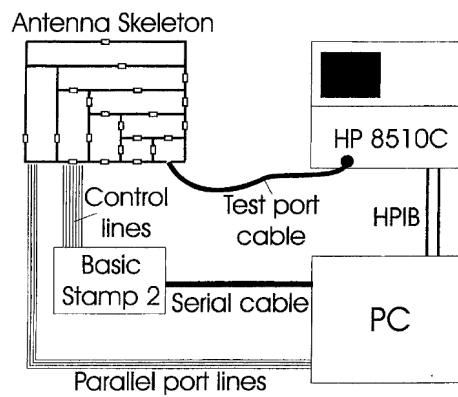
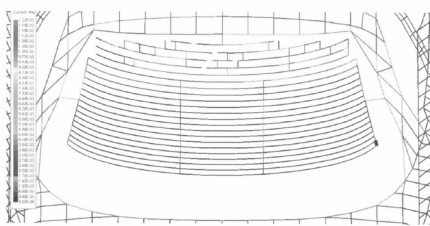
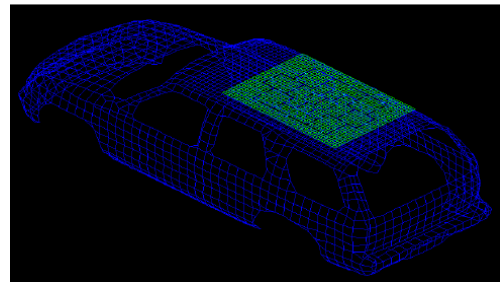


Figure 59 - Typical configuration described in [82]

A self-structuring structure can find applications in different fields [88]. These solutions, (shown in Figure 60) can be also used for TV signal reception [89] or for car Radio signal reception [90], [91]. Other existing applications include multiband devices [92].



(a)



(b)

Figure 60 - Different design for being integrated on a car: (a) integration on the car top [88] and (b) in the back window [90]

The typical configuration of a self-structuring antenna is the simple interconnection of wires made by switch [93]. Switches can also be used as shorting pin of a patch antenna as described in [94].

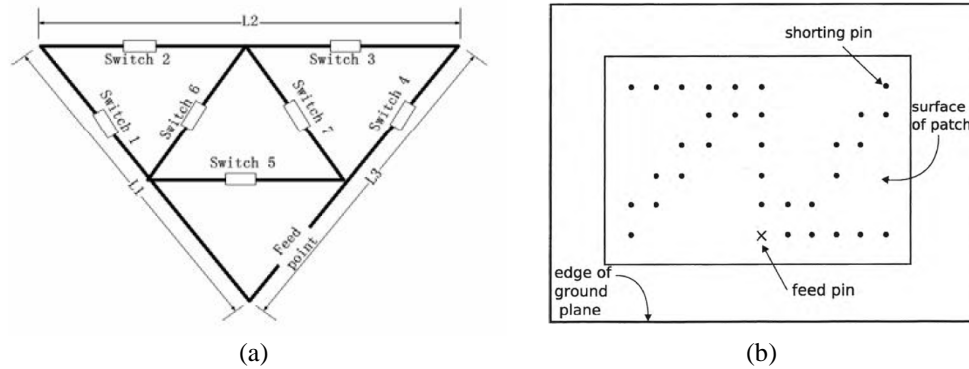


Figure 61 - Different configuration for a Self-Structuring antenna: (a) interconnection of wire performed by switches [93], and (b) shorting pins insertion controlled by switches [94]

The operative frequencies of existing self-structuring antenna include the UHF band [95], the LTE band [96], and the X band [97].

A fundamental role is also played by the algorithm deployed to select the appropriate shape of the radiating element. When the number of possible states is very high, general search algorithm are usually deployed. Algorithms proposed in the literature are the Simulated Annealing Algorithm, the Ant-Colony Optimization Algorithm, and the Genetic Algorithm in [98] or a Quantum-inspired Immune Memory Algorithm [99].

3.3 Antenna Design

The realized antenna has been designed to be integrated on a commercial lifejacket for maritime emergency operation. Therefore it should use as it best the floating element surface (13x29cm), guaranteeing the best radiating condition with a limited number of possible radiating configuration in order to perform a full optimization research with a commercial microcontroller. Shape modification is performed by a Microcontroller located into the floating element of a commercial life-jacket (Figure 62).

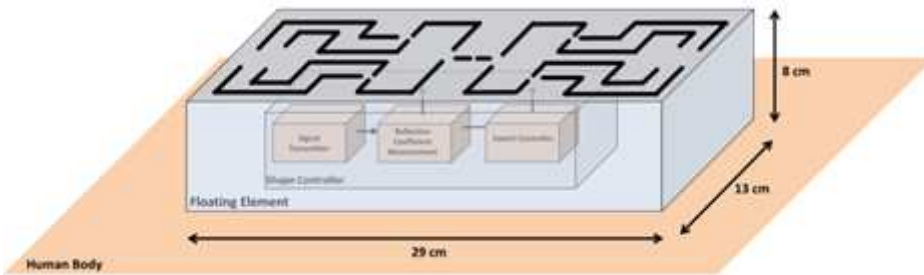


Figure 62 - Integration of the Self-Structuring antenna on the floating element of a commercial life-jacket

The topology of the proposed antenna is depicted in Figure 63. It is possible to recognize the shape of a dipole that has been folded in order to fill the entire available surface. The input port of the antenna is located at the centre of a commercial life jacket floating element (8 cm thick). Starting from the central point, the antenna follows a multi-branch meandered dipole design. The main branches are the inner branch (Figure 63b) and the outer branch (Figure 63c). Each copper strip is connected to the adjacent one by means of RF switches. At the end of every branch, some conducting elements could be added for fine tuning by applying single-pole single-throw switches. At all other locations, single-pole double-throw switches are used.

The basic idea behind the design is to use the principal switches in order to look for a configuration able to minimize in a coarse way the reflection coefficient. Once a first minimization is performed, a fine tuning is permits by the outer switches (the green ones in Figure 63)

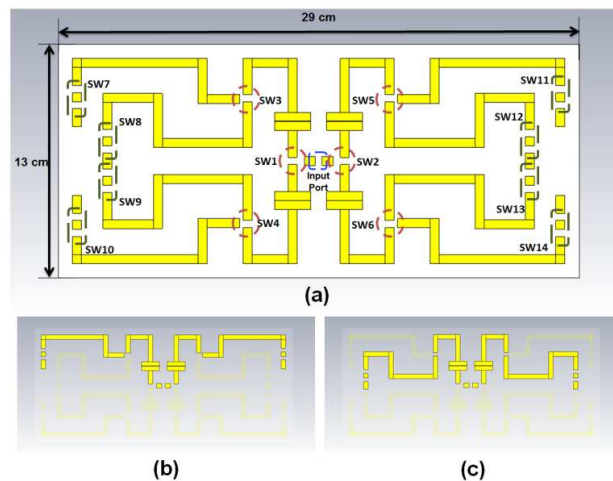


Figure 63 - Design of the Self-Structuring antenna: (a) antenna geometry, (b) principal outer branch and (c) principal inner branch.

The above antenna layout uses a large portion of the surface available on the off-the-shelf floating element (grey rectangle in Figure 63; size: 13x29cm). The number of possible radiating configurations has been limited to 10, in order to reduce the time required by an exhaustive search algorithm to determine the antenna shape with the best performance.

The two main identified configurations have been optimized for free space operation (Figure 64). Hereafter, they are denoted “Conf#1” and “Conf#2” for the outer and inner branch topology, respectively. The latter configurations have been used as a reference for validating the performance of the self-structuring antenna during a number of floating antenna orientations with respect to the water level.

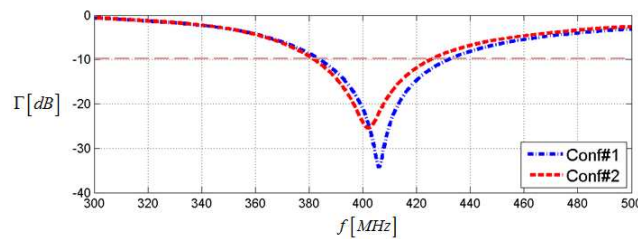


Figure 64 - Simulated S_{11} for the two principal configurations shown in Figure 63 in free space

The working principle of the antenna is depicted in Figure 65. At the beginning the antenna has a specific active radiating shape. Due to a movement of the wearer, it could happen that part of the antenna is lead below the water level causing a malfunctioning in the antenna. In this case the microcontroller detects that the active pattern is not the best one configuration by tracking the reflection coefficient. The radiating shape is dynamically changed in order to restore the optimum radiating conditions.

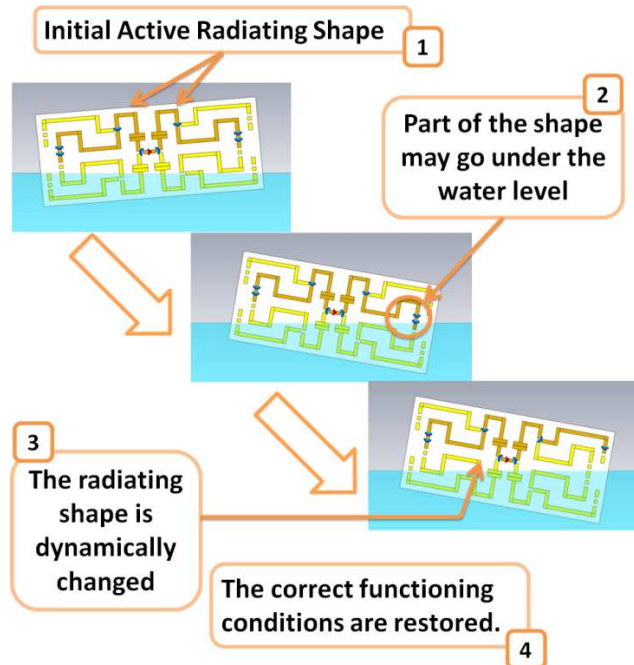


Figure 65 - Working principle of the designed Self-Structuring antenna

3.4 Simulation Results

Simulations have been conducted for different immersion distances d of that part of the floating element immersed into water in a foundering situation and for different rotation angles, when the floating element rotates around its orthogonal antenna axes (Figure 66).

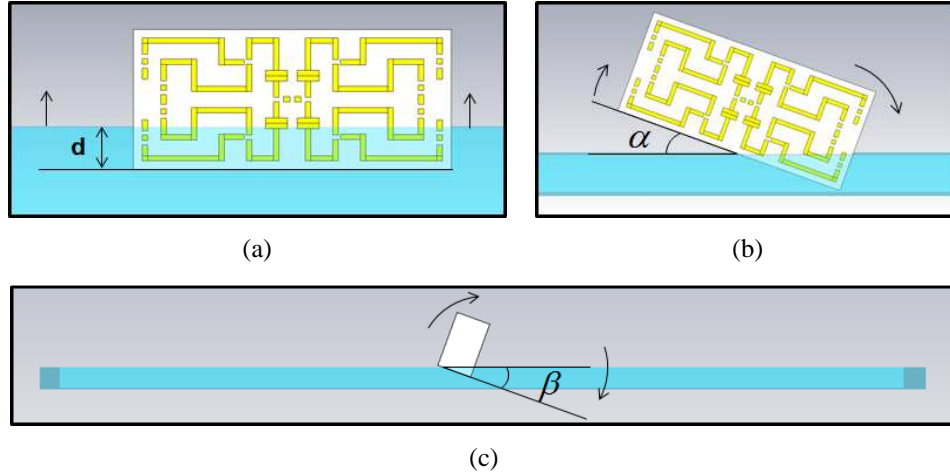
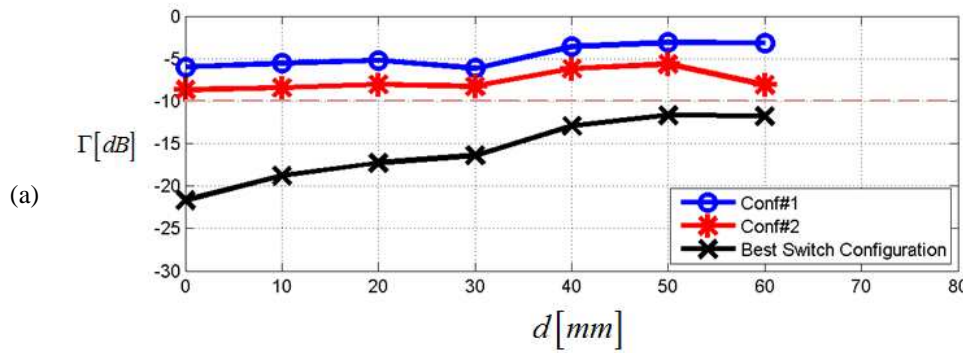


Figure 66 - Different immersion condition considered for the simulated layout: (a) antenna foundering, (b) lateral rotation and (c) frontal rotation.

For a set of values of d , α and β , the numerical results in Figure 67 show the minimum value for the reflection coefficient at 406MHz, which has been obtained by a proper selection of all switches state. It is apparent that the antenna re-configurability improves the S_{11} with respect to both nominal configurations Conf#1 and Conf#2. A correct transmission condition is guaranteed (Return loss greater than 10dB) even if the antenna sinks into the water by 6 cm (more than 45% of the antenna volume under the water), or when performing a lateral/frontal rotation up to 40°.



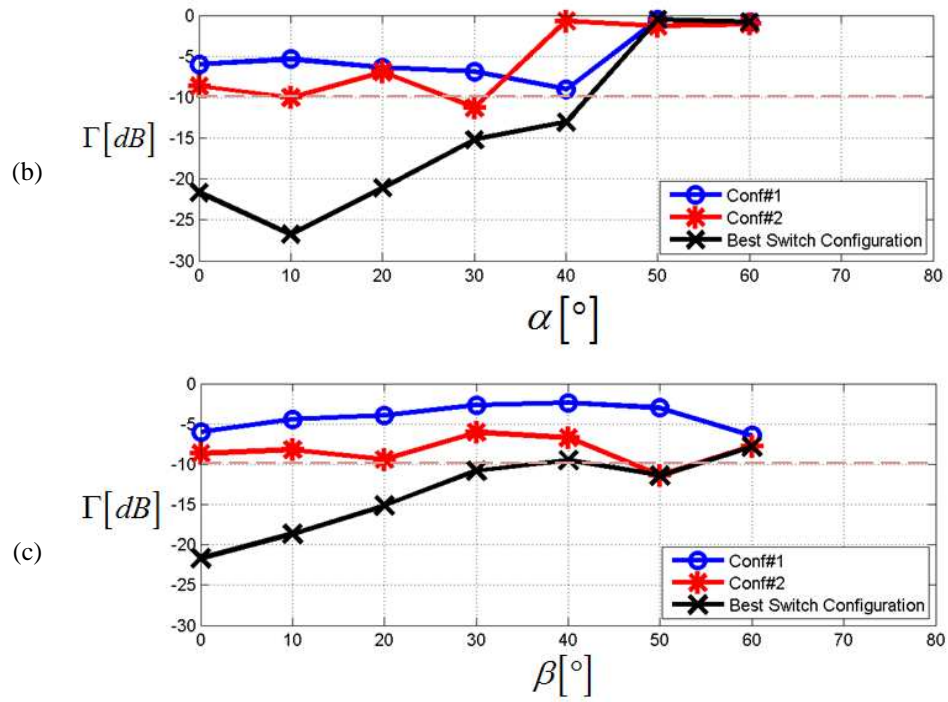
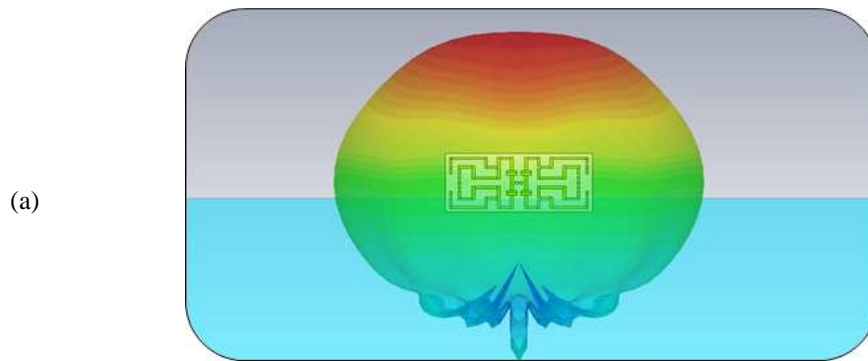


Figure 67 - Simulated S_{11} for different floating antenna positions with respect to water level: (a) antenna sinking; (b) lateral rotation and (c) frontal rotation.

Due to the presence of the water, the antenna radiation pattern looks like a relatively wide pattern pointing toward the zenith direction, regardless the switch combinations as shown in Figure 68.



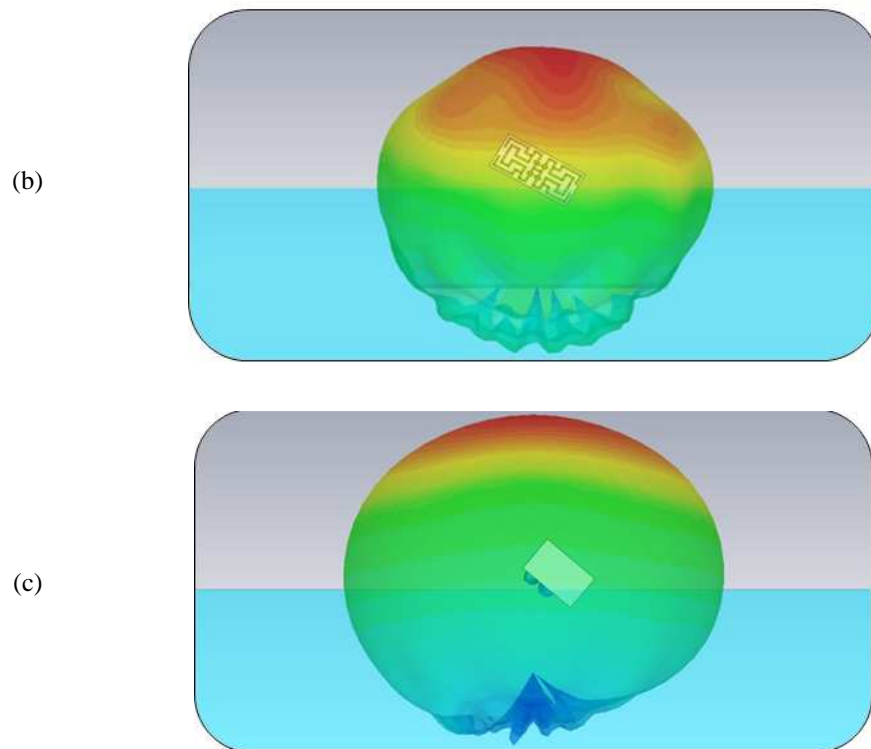


Figure 68 - Simulated Radiation Pattern for the self-structuring layout: (a) antenna sinking; (b) lateral rotation and (c) frontal rotation

3.5 Conclusion

The layout of a reconfigurable multi-branch meandered-like dipole has been proposed to implement a life-jacket integrated self-structuring antenna of a Cospas-Sarsat personal locator beacon. Numerical simulations have been performed with the antenna floating on the water. It has been shown that, through a proper switch configuration, it is possible to guarantee a return loss greater than 10dB even in extreme floating conditions. Due to the presence of the water, the antenna radiation pattern looks like a relatively wide pattern pointing toward the zenith direction, regardless the switch combination.

4 Smart mAritime saTellite terminal for mUltimedia seRvices and conteNts (SATURN) system

4.1 Introduction

In this part of the thesis, the main measured performance results of the SATURN system are presented. SATURN is an acronym that stands for *Smart mAritime saTellite terminal for mUltimedia seRvices and conteNts*. The SATURN project aimed to design and develop a maritime user terminal for small leisure boats (up to 20m of length). Such a terminal allows navigators for receiving contents through a DVB-SH channel and transmitting small amount of data via an ETSI S-MIM return channel (based on the Enhanced Spread Spectrum protocol) using the S-Band (2 GHz). The system performance has been measured in a real environment, emulating the sea-condition by means of an ad-hoc designed Motion Simulator

In 4.2 and in 4.3 the motivation behind the project and the project outline will be presented. In 4.4 the SATURN System prototype is describe. Tests results are shown and discussed in 4.5. Concluding remarks are drawn in 4.6.

4.2 Motivations

In recent years, the demand of multimedia services for vessels and small boats has increased. In particular, a wide demand for terminals that are able to receive and provide contents to users while sailing has been identified (e.g. the weather forecast for a specific area on request, the update of a map on request, the possibility to rent a berth in a harbour, viewing television channels). Such terminals require to be easily fitted on small boats in order to be used as a traditional plotter (i.e. a satellite navigator). In the current market there are specific devices suitable for small boats which can provide limited functionalities in the open sea. Indeed, some of such devices can communicate only with radio-base stations located on the coast. On the other hand, wireless connectivity in open sea is guaranteed by those terminals which exploit satellite link in the C-band or Ku-band (e.g. VSAT systems). However, such terminals represent a bulky and expensive solution for small boats, since their antennas are usually large high-gain array.

For these reasons, the SATURN (Smart mAritime saTellite terminal for mUltimedia seRvices and conteNts) project [100] aimed to design an innovative cost-effective maritime user terminal able to manage broadcast services (e.g. Radio and TV), geo-referenced information (e.g. weather forecasts, security information) and interactive services. The project was cofounded by the European Space Agency (ESA) in the framework of “Artes 5.2 Telecom–Technology, Non-competitive industry-initiated activities” and the Italian Space Agency (ASI). The Calero Advanced Technologies division of the Calero group coordinated the activities of the project; AvMap, ITLink (with some activities carried out from the University of Pisa), MBI and SpaceSYS were involved as sub-contractors. Moreover, Eutelsat Innovation Team endorsed the project and actively supported the tests.

The novelty of SATURN solution is the use of the satellite S-band (1980-2200 MHz) communication channel for providing interactive services on board, during the normal navigation far from the shore.

4.3 SATURN Project Outline

The project focused on the development of innovative technologies for satellite terminals to use in the maritime sector. The main features are:

- Bidirectional communication with one single antenna in half-duplex configuration, for receiving and transmitting over a satellite link;
- Smaller antenna than those conventionally used in satellite systems and handiness for being installed even on very small vessels;
- Fully interoperability with maritime plotters and personal devices such as smartphones, PCs, Tablets;
- Capability to receive audio/video streaming even in the open sea;
- Multimedia contents support;
- Intuitive web interface for an easy management of all the services;
- Capability to request and receive complete weather forecasts with more frequent updates than in other solutions;
- Capability to send distress alerts and messages compliant to the AIS standard;
- Attractive price;
- Capability to provide several services, including updating plotter maps while sailing, traffic monitoring, fleet management, sending and receiving text messages and e-mails.

A basic concept of the SATURN End-to-End Communication System has been schematized in

Figure 69. The EUTELSAT 10A satellite has been used during the project. The satellite was able to communicate with the SATURN system using the DVB-SH standard [101] (2170-2200 MHz) on the Forward Link, and using the ETSI S-MIM standard based on the E-SSA protocol [102]-[103] (1980-2010 MHz) on the Return Link.



Figure 69 - SATURN End-to-End Communication System.

4.4 SATURN Terminal

In this section, the SATURN Terminal is described as well as the specific setup used during the performance tests. In Figure 70 a schematic representation of the main components of the SATURN Terminal is shown. In particular, it is possible to identify a Forward Link Chain (oriented to the DVB-SH signal reception) and a Return Link Chain (oriented to the E-SSA signal transmission).

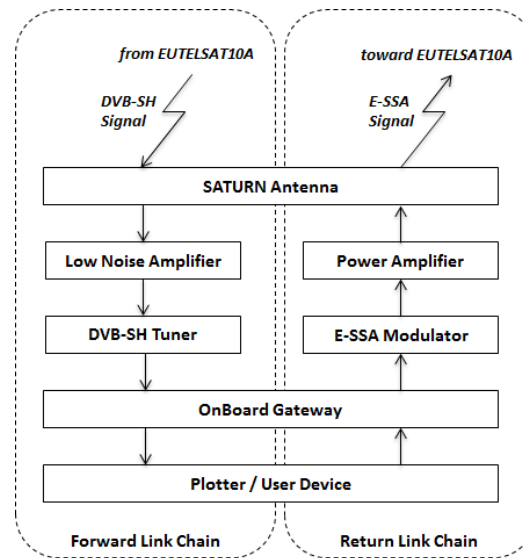


Figure 70 - SATURN End-to-End Communication System

4.4.1 Forward Link Chain (DVB-SH signal reception)

The Forward Link Chain is responsible for the DVB-SH signal reception. As shown in Figure 70, the main components are the SATURN Antenna, the Low Noise Amplifier (LNA), the DVB-SH Tuner, the SATURN Gateway and the SATURN Plotter (or the user-devices).

The SATURN Antenna (Figure 71) has been designed in the SATURN project framework. It consists of six 60-degrees-shifted circularly-polarized radiating elements connected to an Electromechanical Switch with a measured maximum gain of 8dB. A sensor suite (gyrocompass, inclinometer, GPS) provides real-time information about the ship position (instantaneous yaw angle, instantaneous pitch angle, instantaneous roll angles, and geographical position). By means of a real-time elaboration of such data it is possible to detect the particular radiating element which is better oriented toward the satellite and to activate it (a proper beam selection algorithm has been implemented in a microcontroller).



Figure 71 - SATURN Antenna

The received DVB-SH signal is then amplified through a Low Noise Amplifier (Gain of 30.8dB, Noise Figure of 0.6dB) and sent to the DVB-SH Tuner (DiBcom DiB29098S COFDM demodulator). The latter (Figure 72) is a high performance receiver of signals for mobile, portable and fixed devices. It is also compliant with other DVB standards (DVB-T [104] and DVB-H [105]).



Figure 72 - DVB-SH Tuner

The DVB-SH Tuner is connected to the SATURN Gateway through an USB Connection. Thus, the Gateway collects the contents and makes them available to the plotter or to a user device (e.g. iPad, iPhone, PC) by means of a Wi-Fi (2400-2485 MHz) connection.

The plotter is the end user front-end and it is responsible of providing several contents such as live weather forecast. It represents the last macro-component of the receiving chain, and it has been used for a qualitative evaluation of the implemented Pilot Application Services. In Figure 73 the SATURN Plotter is shown.



Figure 73 - SATURN Plotter

4.4.2 Return Link Chain (E-SSA signal Transmission)

The Return Link Chain is responsible for the E-SSA signal transmission toward the satellite. As shown in Figure 70, the main components are the SATURN Plotter, the E-SSA Transmitter, the Power Amplifier and the SATURN Antenna.

The user device or the plotter can be used by the customer for requesting contents (e.g. Premium Contents) or for sending a distress beacon (e.g. man over board, engine failure). The request is sent to the On-Board Gateway using a Wi-Fi network.

The On-Board Gateway is then connected, through an Ethernet Connection, to the E-SSA Modulator designed on a Software Define Radio (ETTUS USRP E-100[106]), which creates a pulse signal shaped as a square root raised cosine with a roll-off factor of 0.22.

The signal is then amplified by means of a Power Amplifier (Gain of 43.8dB) and sent to the SATURN Antenna.

4.4.3 Test Environment Setup

In the project, a proof-of-concept prototype terminal has been realized, aiming to evaluate the capability of such a system to provide a bidirectional satellite communication also during the navigation. For this reason, an ad-hoc rotating platform has been realized, named Motion Simulator, which is able to emulate the sea condition up to a sea-state 6. Such a platform is piloted by 3 different motors which control the different inclination angle (roll angle, pitch angle and yaw angle) that can be experimented on board of a small vessel (Figure 74). By means of a management software, it is possible to rotate the platform in a user-defined position or to emulate the ship oscillation due to the sea conditions.

In Figure 74 the three inclination angles are indicated. The roll angle indicates the rotation of a vessel around its “front to back” axis. Its maximum value depends on how well the wave energy couples with the hull. The pitch angle indicates the rotation of a vessel about its transverse (side-to-side) axis. The maximum pitch angle depends on the particular sea-state and on the ships length. The yaw angle represents the rotation of a vessel around its vertical axis. By using such a movement profile it is possible to simulate a sea route.

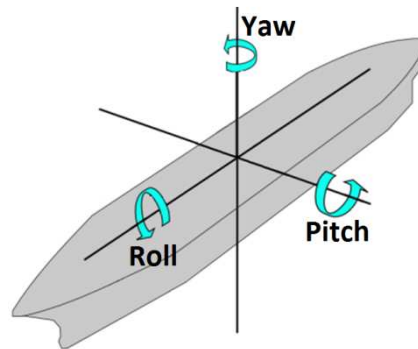


Figure 74 - Different inclination angles for a vessel

For the purpose of simulating the ship motion in different sea conditions, it has been assumed that the sea waves cause a sinusoidal motion of the ship (Figure 75 and Figure 76). The yaw movement profile has been defined by using a triangular signal input (Figure 77). The main parameters for the emulation of the sea-state 4 profile [107] are collected in Table 10.

TABLE 10
MAIN PARAMETER FOR THE EMULATION
OF THE SEA STATE 4 PROFILE

	Amplitude (A), [deg]	Period [s]
Roll Angle	20	7.1
Pitch Angle	5	3.5
Yaw Angle	180	600

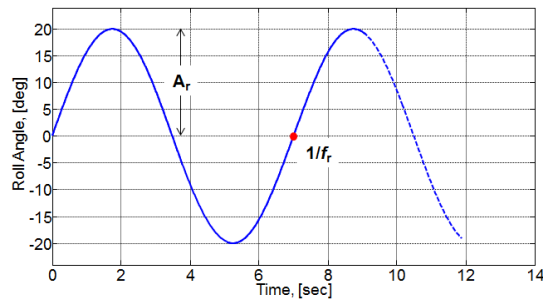


Figure 75 - Roll Angle Profile

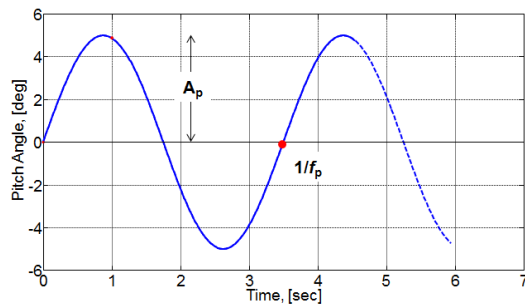


Figure 76 - Pitch Angle Profile

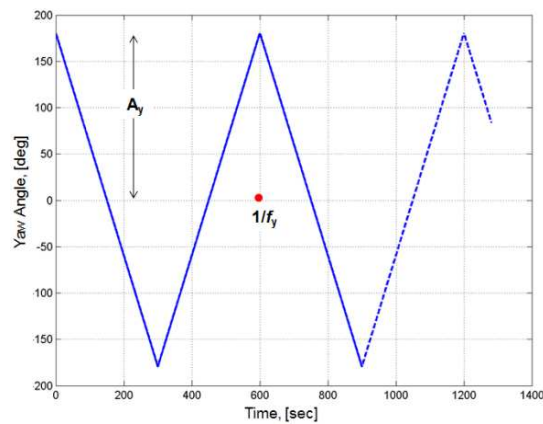


Figure 77 - Yaw Angle Profile

The set of angles used to pilot the three motors, can be recorded and written in a text file. Thus, they can be compared with the actual angles measured by the inclinometer of the sensor suite mounted on the SATURN Antenna. The comparison between the two set of angles provides information about the accuracy of the rotating platforms. Moreover, they can be related to other antenna parameters (i.e. C/N, received power level) in order to perform further tests.

In Figure 78 the SATURN prototype terminal realized in the project framework is depicted.

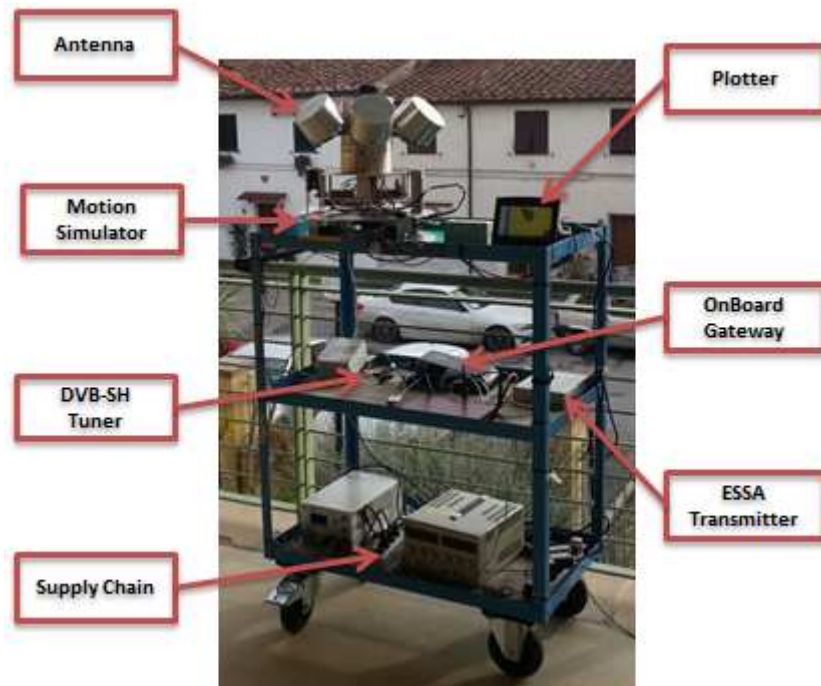


Figure 78 - SATURN Prototype

4.5 Test Execution

4.5.1 Radiation Pattern Estimation

As described in 4.4, the SATURN Antenna is composed by 6 elements, but only one is activated at a time. To cover all the 360° in azimuth (yaw angle), each element is characterized by a HPBW of about 60° , and they are spatially shifted of 60° . They have been properly optimized and tested in an anechoic chamber, both in terms of input impedance matching and radiation pattern. The overall antenna radiation pattern could be obtained only by overlapping all the six 3D radiation patterns.

However, the overall radiation pattern doesn't represent the actual antenna functioning. Indeed, one particular radiating element is activated at a time by the microcontroller on the basis of the measured angles (provided by the sensor suite). Thus, an error on the measured angles (mainly due to the inclinometer accuracy) could affect the beam selection criteria, and the value of the expected instantaneous received signal power.

In order to obtain a sort of operative radiation pattern of the antenna, the received Carrier-to-Noise ratio (C/N) has been measured by varying the yaw angle, during the DVB-SH signal reception. It is worth noting that by using a Spectrum Analyser it is possible to estimate the (C+N)/N value, instead of the exact C/N. However, when such a quantity assumes values higher than 2-3dB, a good approximation of the real C/N is reachable, which is also directly proportional to the real radiation pattern.

For this reason, when a rotation of the antenna along his vertical axis (yaw angle) is performed, six lobes should be visible corresponding to the 6 different radiating elements. Note that in this case the aim of the test was to verify if every radiating element were selected in a proper way (the selected element should be the one that is in the better oriented position towards the satellite). Thus every radiating element should be activated for a 60° span over the entire 360° lap. For this test, the roll and pitch angles have been fixed in order to guarantee that the maximum gain direction of the radiating elements was aligned toward the satellite (42° of elevation angle with respect to the horizon). The yaw angle has been varied between 0° and 360° with a step-angle of 3° .

In Figure 79, the estimated radiation pattern of the SATURN Antenna on the plane $\theta = 42^\circ$ (where θ is the elevation angle of the satellite with respect to the local horizon) is shown. It is possible to observe the 6 lobes which correspond to the different 6 radiating elements. As expected, every radiating element is activated for about 60° when the system is performing a complete rotation along his vertical axis (Table 11). It is worth noting that the beam width estimation accuracy strictly depends on the particular step-angle (in this test it was equal to 3°).

TABLE 11
ESTIMATED RADIATING ELEMENT BEAM WIDTH

Element Number	Beam Width
1	57°
2	57°
3	66°
4	60°
5	60°
6	60°

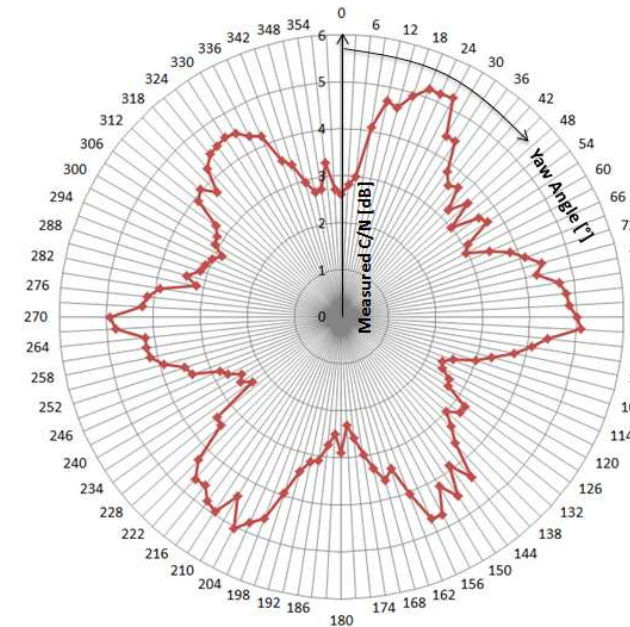


Figure 79 - Measured C/N level

4.5.2 Forward Link Measurement Evaluation

In order to evaluate the SATURN Terminal performance when receiving DVB-SH signal, several tests have been carried out. In particular, three main parameters have been taken into account, namely the Frame Loss Rate (FLR), the Erroneous Seconds Rate (ESR5(20)) and the Service Availability (SA). In Figure 80 a schematic representation of the SATURN System Forward Link Chain is shown, both considering the SATURN Terminal and the satellite Hub.

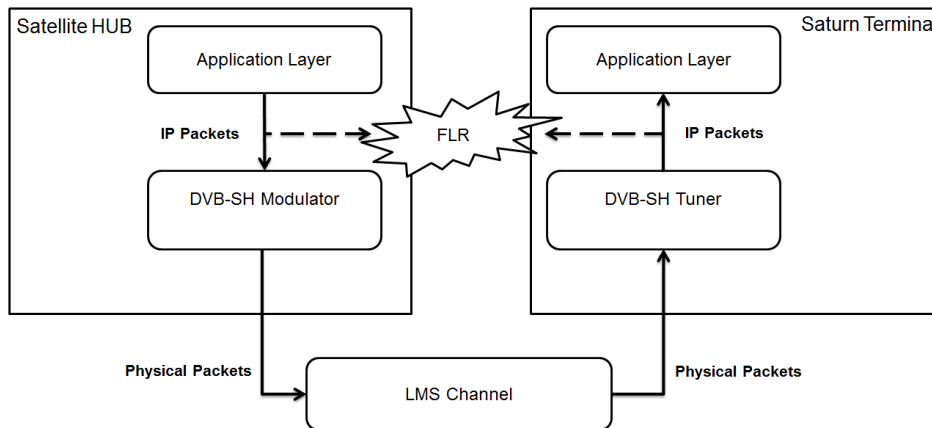


Figure 80 - Forward Link Chain block scheme

4.5.2.1 FLR Evaluation

The Frame Loss Ratio (FLR) represents the ratio of lost packets with respect to the total amount of the sent DVB-SH packets. Comparing the number of IP packets transmitted by the SATURN Terminal with the number of frames received by the Satellite Hub, it is possible to evaluate the frame loss rate of the SATURN system on the forward link. For this test, ad-hoc scripts have been realized, in order to set the number and the transmission rate of the packets sent by the Satellite Hub. Another script has been realized to collect the received packets at the SATURN Terminal side.

This test has been carried out in several working conditions:

- Antenna fixed in maximum gain position, which represents the Terminal best working condition;
- Antenna fixed in minimum gain position, which represents the Terminal worst working condition;
- Antenna moving along a sea-state 4 profile, which represents a normal condition during the navigation in the Mediterranean Sea

In Table 12 all the results are collected.

TABLE 12
MEASURED FLR ON THE FORWARD LINK

Condition	Results
Max Gain condition	Lower than $o(10^{-3})$
Min Gain condition	Lower than $o(10^{-3})$
Sea State 4 Profile	26×10^{-3}

When the antenna was in a fixed position (both in maximum and in minimum gain position), an FLR of an order lower than 10^{-3} has been measured. These results demonstrate that the SATURN Terminal receiving chain has been properly designed.

On the other hand, the measured FLR increases by emulating the sea-state 4. The frame losses are mainly due to the switches between an element to the other one. Indeed, during the transition from one element to another, the LNA is switched-off and no packets could be received by the system.

4.5.2.2 Erroneous Seconds Rate 5(20) and Service Availability

The Erroneous Seconds Rate 5(20) (ESR5(20)) is a parameter used for the assessment of DVB-T Transmission quality and it is strictly related to the correct reception of a streaming signal (Audio/Video) [108]. The ESR5(20) assumes value equal to 1 if there is at least one erroneous second in a time window of 20 seconds (5% of Erroneous Second Ratio over a time window of 20 seconds corresponds to one erroneous second). Otherwise, ESR5(20) is set to 0. In Figure 81 the ESR5(20) measured in a time interval greater than 1 hour is shown.

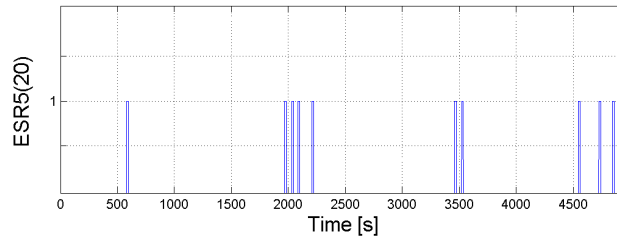


Figure 81 - ESR5(20) measured in more than an hour

Starting from the measured ESR5(20) it is possible to evaluate the Service Availability, defined as the total time in which the ESR5(20) is fulfilled with respect to the total time of the measurement. As experienced in [109], the test should be considered pass if the Service Availability is higher than 95%. In the test shown in Figure 81, a Service Availability of 96.8% has been obtained.

4.5.2.3 Beam Switching Time

The Beam Switching Time (BST) is the time interval needed for changing the active radiating element. In this time interval both the interruption of the forward link reception and the signal streaming synchronization recovering are included.

During this test the antenna was moved around its vertical axis (only yaw angle), while a stream of packets were transmitted to the SATURN Terminal. Measuring this parameter, it is possible to implement an appropriate FEC protection for avoiding packet losses during the radiating element switch.

To measure the BST, packets were sent with a rate of 10pkt/sec (time precision of 0.1 seconds). Data have been collected over a transmission of 500 seconds (Figure 82). It has been observed that the packet were lost in in burst of 6/7 packets. Considering the transmission rate used for this test, it is possible to state that the BST value is included between 0.6 and 0.7 seconds. Thus, a FEC protection with a length of 1 second would be enough to avoid packet losses caused by the beam switching on the forward link.

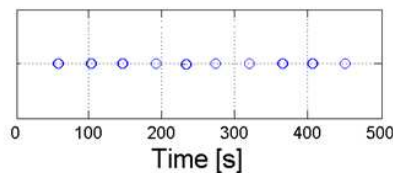


Figure 82 - Packet reception for the Beam Switching Time measurement. The blue dots represent the packets lost during the reception

4.5.3 Return Link Measurement Evaluation

In Figure 83 a schematic representation of the SATURN System Forward Link Chain is shown, both considering the SATURN Terminal and the satellite Hub.

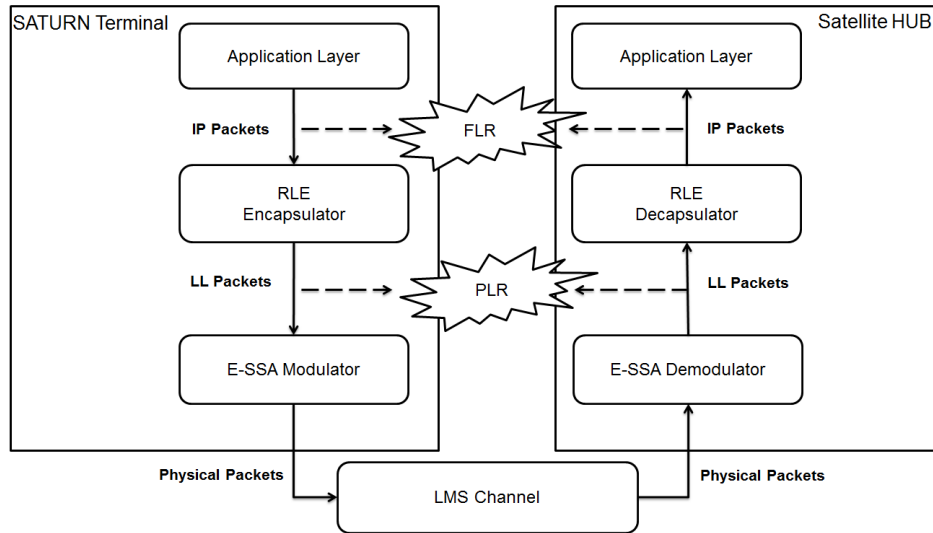


Figure 83 - Return Link Chain block scheme

The tests on the Return Link focused on the evaluation of the capability of the SATURN system of transmitting messages toward the satellite, by looking at the correct reception at the Satellite Hub in Rambouillet (France). In these tests, the Frame loss rate (FLR) and the Packet Loss Rate (PLR) have been taken into account

4.5.3.1 Frame Loss Rate and Packet Loss Rate Evaluation

Similarly to the afore-described FLR evaluation test, in the Forward Link Chain, E-SSA packets have been sent from the SATURN Terminal toward the satellite. The comparison between the received E-SSA packets and the total amount of transmitted packets provides the estimation of the PLR on the Return Link channel. It is expected that the PLR on the return link has an order of 10^{-3} . Indeed, this parameter mainly depends on the characteristics of the ESSA Modulator that has been assessed in a laboratory environment (direct connection between the E-SSA Modulator and the E-SSA Demodulator with no white noise injection).

Again, such a parameter has been evaluated for three different antenna scenarios, both in fixed position (maximum and minimum gain) or moving state (sea-state 4). Results are collected in Table 13.

TABLE 13
MEASURED PLR ON THE RETURN LINK

Working Condition		Measured PLR
Cable Connection	No White Noise Injection	3.9×10^{-3}
Satellite Link	Max Gain Condition	6.3×10^{-3}
Satellite Link	Min Gain condition	7.8×10^{-3}
Satellite Link	Sea State 4 Profile	6.4×10^{-3}

Moreover, in the E-SSA standard [102] an RLE Encapsulator (as shown in Fig.15) is foreseen, and a single IP packet longer than 150 Bytes could be divided in two or more fragments. Thus, also the Packet Loss Rate has been evaluated in order to verify the proper functioning of the RLE Encapsulator.

The Frame Loss Rate and the Packet Loss Rate are correlated. In particular, indicating with M the number of fragments by which a packet is divided by the E-SSA Convergence Layer, the relation between the PLR and the FLR is the following [110]:

$$FLR = 1 - (1 - PLR)^{M+1} \quad (1)$$

By implementing ad-hoc scripts it was possible to get both the sent fragment ID (at the SATURN Device) and the received fragments ID (at the SATURN Hub). A comparison between them, provides the estimation of the Packet Loss Ratio (PLR).

The performances in terms of FLR are summarized in Table 14, for all the considered scenarios. The comparison between the Expected Value (as estimated from the above equation using data collected during the PLR evaluation) and the measured value is depicted.

TABLE 14
MEASURED FLR ON THE RETURN LINK

	Expected FLR	Measured FLR
Max Gain Condition	18.8×10^{-3}	16.2×10^{-3}
Min Gain Condition	23.2×10^{-3}	22.1×10^{-3}
Sea State 4 Profile	19.1×10^{-3}	26.6×10^{-3}

Both the measured FLR and the PLR are compliant with the expected value. The FLR value that has been measured when the antenna was performing a movement along a Sea State 4 profile is higher than the expected value.

This greater loss of packets has appeared because when the antenna goes to the transmitting state, no beam switching can be performed. In this situation the active beam could not be the best beam (it doesn't point correctly to the satellite), so the transmission is performed with an antenna gain that is below the minimum antenna gain needed for the satellite transmission.

4.5.4 SATURN Services Evaluation

Between all the possible services that could be implemented on the SATURN system, three of them have been selected as Pilot Services:

- Sea Weather;
- Sea Alarm;
- Audio/Video streaming.

These three services have been chosen because of their distinctive features. Indeed, the Sea Weather represents the possibility of broadcasting several information to all the SATURN users which can be periodically updated. The Sea Alarm represents the possibility to have interaction with the Satellite hub. Finally, the Audio/Video streaming represents the possibility to have a real time streaming contents.

4.5.4.1 Sea Weather Service Evaluation

The Sea Weather service is used for having information about the weather forecast. These information are periodically broadcasted to all the SATURN user. The aim of this test was to check if the information were correctly received after an update.

The weather update has been sent every 5 minutes. With this interval between two different updates it should be expected that all the updates would be correctly received and displayed on the plotter.

The results are depicted in Table 15 and all the Weather Updates have been correctly received (Figure 84).

TABLE 15
SEA WEATHER STATISTICS

Condition	Weather Update Received
Max Gain condition	100%
Min Gain condition	100%
Sea State 4 Profile	100%



Figure 84 - Example of Sea Weather Update Correctly Displayed on the SATURN Plotter

4.5.4.2 Sea Alarm

The Sea Alarm service permits to the end user to send an alarm message in case of a particularly emergency. (e.g. man over board, fire on board, engine failure).

The message sent to the hub contains information about the position of the vessel and the type of emergency.

Because of its emergency nature, the device should be sure that the message has been correctly received by the Hub, thus the SATURN system performs a packet retransmission every 30 seconds until the reception of an ACK message.

In this test a total number of 50 alarm messages have been sent when the antenna was in a fixed position and when it was performing a movement along a sea state 4 profile (Figure 85).

The main results are here collected in Table 16.

TABLE 16
SEA WEATHER STATISTICS

Condition	Sea Alarm Messages Received
Max Gain condition	100%
Min Gain condition	100%
Sea State 4 Profile	100%

All the Sea Alarm messages have been received during the tests. In particular when the antenna was in a fixed position every ACK messages have been received without a retransmission. When the antenna was performing a sea state 4 profile, 7 Sea Alarm Messages have been lost over a total number of 50. Several Alarm Messages has been lost because the antenna was performing a movement along a sea state 4 profile. Indeed, in such scenario several switches from an element to the adjacent are expected and during these events messages could be lost. It is worth noting that the ACK protocol implemented at the application level (performing a retransmission if no ACK message has been received after 30 seconds from a transmission of a Sea Alarm Message) can assure the total reception of all the sent Alarm Messages.



Figure 85 - Example of Sea Alarm Message Correctly sent to the Hub

4.5.4.3 Audio/Video Streaming

The Audio/Video streaming represents the possibility to receive a stream of contents from the Satellite Hub. These contents could be either Free Contents or Premium Contents. The difference between these two kinds of traffic is only that Premium Contents could offer On-Demand Contents (e.g. Sport Event, Film on request).

The aim of this test is to check the correct reception of the streaming at the eye of the user. This service has been evaluated in a normal working condition during the sailing, so the antenna was moved along a sea state 4 profile. On this stream of data an MPE-iFEC protection [110] was present. This protection would permit no loss of contents in case of DVB-SH signal loss for a short period of time. During the movement of the antenna no interruption of the Audio/Video signal has been

observed even if several packets have been lost (as observed during the test on the Forward Link). This means that the MPE-iFEC protection is able to compensate losses of packets assuring a good quality of the Audio/Video Streaming contents.

4.6 Conclusion

In this chapter, the main measured performance results of the ARTES 5.2 European Space Agency (ESA) SATURN (Smart mAritime saTellite terminal for mUltimedia seRvices and conteNts) project system have been presented. Several tests have been carried out in order to assess the SATURN Terminal Performance (received Signal Power, Frame Loss Rate, Packet Loss Rate and Service Availability). Moreover, the three services implemented in the SATURN system (Sea Weather, Sea Alarm and Audio/Video Streaming) have been described and tested. At the end of the Performance Analysis it is possible to conclude that:

- The high-gain, compact smart antenna SATURN Antenna is able to select the proper radiating element on the basis of the data measured by the Sensor Suite (GPS, gyrocompass, inclinometers).
- The SATURN System is able to receive data (e.g. weather forecasts, Audio/Video streaming) from the satellite (EUTELSAT 10A) using well-known DVB-SH (2170-2200 MHz) technology and packets losses due to the beam changing doesn't substantially affect the Service Availability measured through the ESR5(20).
- The SATURN System is able to transmit E-SSA packets toward the EUTELSAT 10A Satellite (Return Link) are properly transmitted and received also when the antenna is moving emulating a sea-state 4 condition.
- The SATURN System is able to provide an Audio/Video Streaming Services to the end user during normal navigation with a sea state up to 4.
- The SATURN System can send an alarm message in case of emergency (man over board, fire on board, engine failure) toward the Satellite Hub that is able to correctly receive them and managed them.
- The SATURN System is able to provide to the end user the possibility to have update Sea Weather Maps during the normal navigation.

Conclusions

In this dissertation, Adaptive Antennas for Mobile Terminals of Wireless Communication Links have been analysed and proposed for Off-Body Communication in the UHF band and for satellite communication in the S-band.

In Chapter 1, a self-tuning network for a wearable Cospas-Sarsat transmitting system has been described. The realized low-cost self-tuning network is able to estimate the actual reflection coefficient and to tune a dedicated impedance network accordingly by a dedicated robust software architecture. The systems increases the probability of correct distress beacon signal transmission in harsh operating conditions by ensuring that the Cospas-Sarsat requirements remain satisfied at all time.

In Chapter 2, a wearable antenna for off-body communications has been shown. Starting from a bowtie structure, a first-order Sierpinski fractal antenna has been proposed in order to meet the requirement of low cost integration and reliability of the wireless link. The antenna's reflection coefficient and the radiating pattern were carefully studied by simulations and measurements. The realized adaptive feeding network controls the resonance frequency of the antenna, enabling operation in both the 868MHz and the 915MHz frequency bands.

In Chapter 3, the layout of a reconfigurable multi-branch meandered-like dipole has been proposed to implement a life-jacket integrated self-structuring antenna of a Cospas-Sarsat personal locator beacon. Numerical simulations have been performed with the antenna floating on the water. It has been shown that, through a proper switch configuration, it is possible to guarantee a return loss greater than 10dB even in extreme floating conditions.

Finally, in Chapter 4, the Smart mAritime saTellite terminal for mUltimedia seRvices and conteNts (SATURN) system has been presented. The realized system is able to dynamically change the active radiation pattern in order to enable the reception and the transmission of content through a geostationary satellite.

Bibliography

- [1] "International Cospas-Sarsat Programme" <http://www.cospas-sarsat.int/>
- [2] J.V. King, "Cospas-Sarsat: an international satellite system for search and rescue", *SPACE COMMUNICATIONS*, 2002 18, (3-4), pp.139-150,
- [3] Nepa, P., Manara, G.: "On the stochastic characterization of wearable antennas," *PIERS 2013 (Progress in Electromagnetics Research Symposium)*, Stockholm, Sweden, 2013, p.1
- [4] Hall, P.H., Hao, Nechayev, Y. V. I. et al.: "Antennas and Propagation for On-Body Communication Systems", *IEEE Antennas and Propagation Magazine*, 49, 3, 2007, pp. 41–58.
- [5] Nepa, P., Rogier, H. : "Wearable Antennas for Off-Body Radio Links at VHF and UHF bands (below 1 GHz): Challenges, State-of-the-Art and Future Trends," to appear on *IEEE Antennas and Propagation Magazine*, 2015
- [6] Serra, A., Nepa, P., Manara, G.: "A wearable two-antenna system on a life jacket for Cospas-Sarsat Personal Locator Beacons," *IEEE Trans. Antennas and Propagation*, 2012, 60, (2), pp. 1035-1042.
- [7] Specification for Cospas-Sarsat 406 MHz Distress Beacons <https://www.cospas-sarsat.int/images/stories/SystemDocs/Current/CS-T-001-Oct2014.pdf>
- [8] Lilja, J., Pynttari, V., Kaija, T., et al.: "Body-Worn Antennas Making a Splash: Lifejacket-Integrated Antennas for Global Search and Rescue Satellite System," *IEEE Antennas and Propagation Magazine*, 2013, 55, (2), pp.:324-341
- [9] Jia-Shiang Fu; Zhu, X.A.; Phillips, J.D.; Mortazawi, Amir, "A ferroelectric-based impedance tuner for adaptive matching applications," *Microwave Symposium Digest, 2008 IEEE MTT-S International* , June 2008 pp.955-958
- [10] Yichuang Sun; Moritz, J.; Xi Zhu, "Adaptive impedance matching and antenna tuning for green software-defined and cognitive radio," *Circuits and Systems (MWSCAS), 2011 IEEE 54th International Midwest Symposium on*, Aug. 2011 pp.1-4
- [11] Firrao, E.L., Annema, A.J., Nauta B.: "An Automatic Antenna Tuning System Using Only RF Signal Amplitudes". *IEEE Transactions on Circuits and Systems II: Express Briefs*, 2008, 55, (9), pp 833 – 837
- [12] F. Nabki, D. Deslandes "An agile matching network using phase detection for antenna tuning" *IEEE 20th International Conference on Electronics, Circuits, and Systems (ICECS)*, 2013
- [13] Qizheng Gu; De Luis, J.R.; Morris, A.S.; Hilbert, J., "An Analytical Algorithm for Pi-Network Impedance Tuners," *Circuits and Systems I: Regular Papers*, *IEEE Transactions on*, 2011, 58, (12), pp. 2894-2905
- [14] Qizheng Gu; Morris, A.S., "A New Method for Matching Network Adaptive Control," *Microwave Theory and Techniques*, *IEEE Transactions on* , 2013, 61, (1), pp.587-595
- [15] Song, H.; Oh, S.H.; Aberle, J.T.; Bakaloglu, B.; Chakrabarti, C., "Automatic antenna tuning unit for software-defined and cognitive radio," *Antennas and Propagation Society International Symposium, 2007 IEEE*, June 2007, pp.85 – 88
- [16] De Mingo, J., Valdovinos, A., Crespo, A., et al.: "An RF electronically controlled impedance tuning network design and its application to an antenna input impedance automatic matching system," *Microwave Theory and Techniques*, *IEEE Transactions on* , 2004, 52, (2), pp.489-497

- [17] Yanghong Tan, Yichuang Sun, Lauder, D.: "Automatic impedance matching and antenna tuning using quantum genetic algorithms for wireless and mobile communications," *Microwaves, Antennas & Propagation, IET* , 2013, 7, (8), pp.693-700
- [18] Sánchez, C.; de Mingo, J.; Garcia, P.; Carro, P.L.; Valdovinos, A., "Application of an Impedance Tuning Network for Mobile DVB-H Terminals," *Vehicular Technology Conference Fall (VTC 2009-Fall)*, 2009 IEEE 70th , Sept. 2009, pp.1-5
- [19] C.M. Coleman, E.J. Rothwell, J.E. Ross: "Investigation of Simulated annealing, ant-colony optimization, and genetic algorithms for selfstructuring antennas," *IEEE TAP*, 52, (4), pp.1007-1014
- [20] Yi Chen; Manteuffel, D., "Miniaturizing of a distributed MEMS impedance matching network," *Antenna Technology (iWAT)*, 2013 International Workshop on, March 2013, pp.303-306
- [21] Sharma, A.K.; Gupta, N., "Impedance matching for RF-MEMS based microstrip patch antenna," *Electrical Engineering/Electronics, Computer, Telecommunications and Information Technology (ECTI-CON)*, 2014 11th International Conference on, May 2014, pp.1-4
- [22] Huang, L.; Russer, P.: "Electrically Tunable Antenna Design Procedure for Mobile Applications," *Microwave Theory and Techniques, IEEE Transactions on*, 56, (12), pp.2789-2797
- [23] Sharma, V.; Pathak, N.P., "Continuously tunable concurrent dual-frequency impedance matching network," *Industrial and Information Systems (ICIIS)*, 2012 7th IEEE International Conference on, Aug. 2012, pp.1-3
- [24] Yi Chen; Martens, R.; Valkonen, R.; Manteuffel, D., "A varactor-based tunable matching network for a non-resonant mobile terminal antenna," *Antennas and Propagation (EuCAP)*, 2014 8th European Conference on, April 2014 pp.1877-1881
- [25] Jang, H., Son, W., Oh, K., et al.: "High-speed real-time hand effect tuning algorithm in hand-held terminal," *Intelligent Radio for Future Personal Terminals (IMWS-IRFPT)*, 2011 IEEE MTT-S International Microwave Workshop Series on, Aug. 2011, pp.1-2
- [26] ZFDC-20-5-S Directional Coupler datasheet, "<http://194.75.38.69/pdfs/ZFDC-20-5.pdf>"
- [27] ZFDC-10-5-S Directional Coupler datasheet, "<http://194.75.38.69/pdfs/ZFDC-10-5+.pdf>"
- [28] AD8302 datasheet, "<http://www.analog.com/media/en/technical-documentation/data-sheets/AD8302.pdf>"
- [29] AtMega328P datasheet, "http://www.atmel.com/Images/Atmel-8271-8-bit-AVR-Microcontroller-ATmega48A-48PA-88A-88PA-168A-168PA-328-328P_datasheet_Summary.pdf"
- [30] AD5504 datasheet, "<http://www.analog.com/media/en/technical-documentation/data-sheets/AD5504.pdf>"
- [31] 'Varicap' diode datasheet, http://www.onsemi.com/pub_link/Collateral/MMBV105GLT1-D.PDF,
- [32] Directional Coupler datasheet, <http://cdn.macom.com/datasheets/MACP-011013.pdf>,
- [33] <http://www.intec.ugent.be/>
- [34] A. Baroni, P. Nepa, H. Rogier: "A reconfigurable layout for a self-structuring life jacket-integrated antenna of a SAR system" *APS 2015*, Vancouver, Canada
- [35] P. Nepa and H. Rogier, "Wearable antennas for off-body radio links at VHF and UHF bands (below 1 GHz): challenges, state-of-the-art and future trends," to appear on *IEEE Antennas and Propagation Magazine*, 2015.
- [36] Design and implementation of Textile antennas and wearable system with high body –antenna isolation, Sam Agnessens, PhD Thesis, 2015
- [37] Salonen, P.; Hurme, L., "A novel fabric WLAN antenna for wearable applications," in *Antennas and Propagation Society International Symposium*, 2003. IEEE , vol.2, no., pp.700-703 vol.2, 22-27 June 2003
- [38] Salonen, P.; Jaehoon Kim; Rahmat-Samii, Y., "Dual-band E-shaped patch wearable textile antenna," in *Antennas and Propagation Society International Symposium*, 2005 IEEE , vol.1A, no., pp.466-469 Vol. 1A, 3-8 July 2005
- [39] Soh, P.J.; Vandenbosch, G.A.E.; Ooi, S.L.; Husna, M.R.N., "Wearable dual-band Sierpinski fractal PIFA using conductive fabric," in *Electronics Letters* , vol.47, no.6, pp.365-367, March 17 2011
- [40] Soh, P.J.; Vandenbosch, G.A.E.; Soo Liam Ooi; Rais, N.H.M., "Design of a Broadband All-Textile Slotted PIFA," in *Antennas and Propagation, IEEE Transactions on* , vol.60, no.1, pp.379-384, Jan. 2012
- [41] Shaozhen Zhu; Langley, R., "Dual-Band Wearable Textile Antenna on an EBG Substrate," in *Antennas and Propagation, IEEE Transactions on* , vol.57, no.4, pp.926-935, April 2009

- [42] Klemm, M.; Troester, G., "Textile UWB Antennas for Wireless Body Area Networks," in *Antennas and Propagation, IEEE Transactions on*, vol.54, no.11, pp.3192-3197, Nov. 2006
- [43] Samal, P.B.; Soh, P.J.; Vandenbosch, G.A.E., "UWB All-Textile Antenna With Full Ground Plane for Off-Body WBAN Communications," in *Antennas and Propagation, IEEE Transactions on*, vol.62, no.1, pp.102-108, Jan. 2014
- [44] Van Torre, P.; Vallozzi, L.; Hertleer, C.; Rogier, H.; Moeneclaey, M.; Verhaevert, J., "Indoor Off-Body Wireless MIMO Communication With Dual Polarized Textile Antennas," in *Antennas and Propagation, IEEE Transactions on*, vol.59, no.2, pp.631-642, Feb. 2011
- [45] Vallozzi, L.; Van Torre, P.; Hertleer, C.; Rogier, H.; Moeneclaey, M.; Verhaevert, J., "Wireless Communication for Firefighters Using Dual-Polarized Textile Antennas Integrated in Their Garment," in *Antennas and Propagation, IEEE Transactions on*, vol.58, no.4, pp.1357-1368, April 2010
- [46] P.Vanveerdeghem, P. Van Torre, C. Stevens, J. Knockaert, and H.Rogier, "Flexible dual-diversity wearable wireless node integrated on a dual polarized textile patch antenna", *IET Science, Measurement & Technology*, vol. 8 no.6, pp. 452-458, 2014
- [47] Dierck, A.; Rogier, H.; Declercq, F., "A Wearable Active Antenna for Global Positioning System and Satellite Phone," in *Antennas and Propagation, IEEE Transactions on*, vol.61, no.2, pp.532-538, Feb. 2013
- [48] Kaivanto, E.K.; Berg, M.; Salonen, E.; de Maagt, P., "Wearable Circularly Polarized Antenna for Personal Satellite Communication and Navigation," in *Antennas and Propagation, IEEE Transactions on*, vol.59, no.12, pp.4490-4496, Dec. 2011
- [49] Q.Bai and R.Langley, "Crumpled textile antennas", *Electronic Letters*, vol.45, no.9, pp.436-438, 2009
- [50] Salonen, P.; Fan Yang; Rahmat-Samii, Y.; Kivikoski, M., "WEBGA - wearable electromagnetic band-gap antenna," in *Antennas and Propagation Society International Symposium, 2004. IEEE*, vol.1, no., pp.451-454 Vol.1, 20-25 June 2004
- [51] Salonen, P.; Rahmat-Samii, Y.; Kivikoski, M., "Wearable antennas in the vicinity of human body," in *Antennas and Propagation Society International Symposium, 2004. IEEE*, vol.1, no., pp.467-470 Vol.1, 20-25 June 2004
- [52] F.Boeykens, L.Vallozzi and H.Rogier, "Cylindrical bending of deformable textile rectangular patch antennas", *International Journal of Antennas and Propagation*, p.170 420,2012
- [53] Boeykens, F.; Rogier, H.; Vallozzi, L., "An Efficient Technique Based on Polynomial Chaos to Model the Uncertainty in the Resonance Frequency of Textile Antennas Due to Bending," in *Antennas and Propagation, IEEE Transactions on*, vol.62, no.3, pp.1253-1260, March 2014
- [54] T.Kellomaki, J.Virkki,S.Merilampi, and L.Ukkonen, "Towards washable wearable antenna: a comparison of coating materials for screen-printed textile-based uhf rfid tags", *International Journal of Antennas and Propagation*, vol.2012, 2012
- [55] Scarpello, M.L.; Kazani, I.; Hertleer, C.; Rogier, H.; Vande Ginste, D., "Stability and Efficiency of Screen-Printed Wearable and Washable Antennas," in *Antennas and Wireless Propagation Letters, IEEE*, vol.11, no., pp.838-841, 2012
- [56] C.Hertleer, A.Van Laere, H.Rogier, and L.Langenhove "Influence of relative humidity on textile antenna performance", *Textile Research Journal*, 2009
- [57] Kaija, T.; Lilja, J.; Salonen, P., "Exposing textile antennas for harsh environment," in *MILITARY COMMUNICATIONS CONFERENCE, 2010 - MILCOM 2010*, vol., no., pp.737-742, Oct. 31 2010-Nov. 3 2010
- [58] Kaija, T.; Lilja, J.; Salonen, P., "Textile antennas: Shotgun proven performance," in *MILITARY COMMUNICATIONS CONFERENCE, 2011 - MILCOM 2011*, vol., no., pp.459-464, 7-10 Nov. 2011
- [59] Hertleer, C.; Tronquo, A.; Rogier, H.; Vallozzi, L.; Van Langenhove, L., "Aperture-Coupled Patch Antenna for Integration Into Wearable Textile Systems," in *Antennas and Wireless Propagation Letters, IEEE*, vol.6, no., pp.392-395, 2007
- [60] Hertleer, C.; Rogier, H.; Vallozzi, L.; Van Langenhove, L., "A Textile Antenna for Off-Body Communication Integrated Into Protective Clothing for Firefighters," in *Antennas and Propagation, IEEE Transactions on*, vol.57, no.4, pp.919-925, April 2009
- [61] Salonen, P.; Rahmat-Samii, Y.; Schaffrath, M.; Kivikoski, M., "Effect of textile materials on wearable antenna performance: a case study of GPS antennas," in *Antennas and Propagation Society International Symposium, 2004. IEEE*, vol.1, no., pp.459-462 Vol.1, 20-25 June 2004

- [62] Rossi, M.; Dierck, A.; Rogier, H.; Vande Ginste, D., "A Stochastic Framework for the Variability Analysis of Textile Antennas," in *Antennas and Propagation, IEEE Transactions on*, vol.62, no.12, pp.6510-6514, Dec. 2014
- [63] S.Agneessens, P.Van Torre, F.Declercq, B.Spinnewyn, G.Stockman, H.Rogier, and D. Vande Ginste "Design of a wearable, low cost, through the wall Doppler radar system", *International Journal of Antennas and Propagation*, vol.2012, p.9,2012
- [64] Declercq, F.; Rogier, H., "Active Integrated Wearable Textile Antenna With Optimized Noise Characteristics," in *Antennas and Propagation, IEEE Transactions on*, vol.58, no.9, pp.3050-3054, Sept. 2010
- [65] Dierck, A.; Rogier, H.; Declercq, F., "A Wearable Active Antenna for Global Positioning System and Satellite Phone," in *Antennas and Propagation, IEEE Transactions on*, vol.61, no.2, pp.532-538, Feb. 2013
- [66] P.Vanveerdeghem, P. Van Torre, C.Stevens, J.Knockaert, and H.Rogier, "Synchronous wearable wireless body sensor network composed of autonomous textile nodes", *Sensor*, vol.14, no.10, pp.18583-18610, 2014
- [67] Declercq, F.; Georgiadis, A.; Rogier, H., "Wearable aperture-coupled shorted solar patch antenna for remote tracking and monitoring applications," in *Antennas and Propagation (EUCAP), Proceedings of the 5th European Conference on*, vol., no., pp.2992-2996, 11-15 April 2011
- [68] N.Chanat, M.Zhabodov, L.Le Coq, and R.Sauleau, "Wearable endfire textile antenna for on body communication at 60GHz", *Antennas and Wireless Propagation Letter, IEEE Transaction on*, vol.11, pp.799-802, 2012
- [69] Conway, G.A.; Scanlon, W.G., "Antennas for Over-Body-Surface Communication at 2.45 GHz," in *Antennas and Propagation, IEEE Transactions on*, vol.57, no.4, pp.844-855, April 2009
- [70] J. Tak and J. Choi, "Circular ring patch antenna with higher order mode for on body communications", *Microwave and Optical Technology Letters*, vol.56, no.7, pp. 1543-1547, 2014
- [71] Agneessens, S.; Van Torre, P.; Tanghe, E.; Vermeeren, G.; Joseph, W.; Rogier, H., "On-Body Wearable Repeater as a Data Link Relay for In-Body Wireless Implants," in *Antennas and Wireless Propagation Letters, IEEE*, vol.11, no., pp.1714-1717, 2012
- [72] Amendola, S.; Moradi, E.; Koski, K.; Bjorninen, T.; Sydanheimo, L.; Ukkonen, L.; Rabaey, J.M.; Rahmat-Samii, Y., "Design and optimization of mm-size implantable and wearable on-body antennas for biomedical systems," in *Antennas and Propagation (EuCAP), 2014 8th European Conference on*, vol., no., pp.520-524, 6-11 April 2014
- [73] T.Castel, P.Van Torre, E.Tanghe, S.Agneessens, G. Vermeeren, W.Joseph, and H. Rogier, "Improved reception of in body signals by means of a wearable multi-antenna system", *International Journal of Antennas and Propagation*, vol. 2013, 2013
- [74] M.L.Scarpello, D.V Giste, and H.Rogier"Design of a low cost steerable textile antenna array operating in varying relative humidity condition", *Microwave and Optical Technology Letters*, vol. 54, no.1, pp.40-44,2012
- [75] M.L. Scarpello, L.Vallozzi, H.Rogier, and D.Vande Giste, "High gain textile antenna array system for off body communication", *International Journal of Antennas and Propagation*, vol.2012, 2012
- [76] Van Torre, P.; Vallozzi, L.; Rogier, H.; Verhaevert, J., "Indoor off-body wireless communication using static zero-elevation beamforming on front and back textile antenna arrays," in *Antennas and Propagation (EUCAP), 2012 6th European Conference on*, vol., no., pp.732-736, 26-30 March
- [77] Van Torre, P.; Vallozzi, L.; Jacobs, L.; Rogier, H.; Moeneclaey, M.; Verhaevert, J., "Characterization of Measured Indoor Off-Body MIMO Channels with Correlated Fading, Correlated Shadowing and Constant Path Loss," in *Wireless Communications, IEEE Transactions on*, vol.11, no.2, pp.712-721, February 2012
- [78] N.Chahat, M.Zhadobov, and R. Sauleau,"Wearable textile patch antenna for ban at 60 GHz", in *Antennas and Propagation (EuCAP), 2013 7th European Conference on, IEEE, 2013*, pp.217-219.
- [79] C. Puente-Baliarda, J. Romeu, R. Pous, A. Cardama, "On the behavior of the Sierpinski multiband fractal antenna," *IEEE Trans. on Antennas and Propag.*, vol.46, no.4, pp.517-524, Apr 1998
- [80] R. Augustine "Electromagnetic modelling of human tissues and its application on the interaction between antenna and human body in the BAN context" Ph.D. Thesis, 2009
- [81] Coleman, C.M.; Rothwell, E.J.; Ross, J.E., "Self-structuring antennas," in *Antennas and Propagation Society International Symposium, 2000. IEEE*, vol.3, no., pp.1256-1259 vol.3, 16-21 July 2000

- [82] Coleman, C.M.; Rothwell, E.J.; Ross, J.E.; Nagy, L.L., "Self-structuring antennas," in *Antennas and Propagation Magazine, IEEE* , vol.44, no.3, pp.11-23, Jun 2002
- [83] Frasc, Jonathan L.; Rothwell, Edward J., "A three dimensional extension of the self-structuring antenna to improve beam steering," in *Radio Science Meeting (Joint with AP-S Symposium), 2015 USNC-URSI* , vol., no., pp.172-172, 19-24 July 2015
- [84] Ozdemir, T., "Polarization diversity cognitive antenna for WiFi and ZigBee applications," in *Wireless and Microwave Technology Conference, 2009. WAMICON '09. IEEE 10th Annual* , vol., no., pp.1-3, 20-21 April 2009
- [85] Ozdemir, T., "A polarization diversity multi-beam antenna for ZigBee applications," in *Wireless and Microwave Technology Conference, 2009. WAMICON '09. IEEE 10th Annual* , vol., no., pp.1-4, 20-21 April 2009
- [86] Yen-Sheng Chen; Yao-Chia Chan; Hsueh-Jyh Li; Rothwell, E.J.; Ouedraogo, R.O.; Shih-Yuan Chen, "A Self-Structuring Electromagnetic Scatterer," in *Antennas and Propagation, IEEE Transactions on* , vol.60, no.4, pp.1931-1941, April 2012
- [87] Li-Yuan Fang; Yen-Sheng Chen; Yao-Chia Chan; Rothwell, E.J.; Shih-Yuan Chen, "Self-structuring electromagnetic scatterer using a conductor-backed template," in *Antennas and Propagation Society International Symposium (APSURSI), 2013 IEEE* , vol., no., pp.1066-1067, 7-13 July 2013
- [88] A White Paper on Self-Structuring Antenna Technology, by John Ross and Edward J. Rothwell, 2004 John Ross & Associates, LLC and Michigan State University
- [89] Perry, B.T.; Coleman, C.M.; Basch, B.F.; Rothwell, E.J.; Ross, J.E., "Self-structuring antenna for television reception," in *Antennas and Propagation Society International Symposium, 2001. IEEE* , vol.1, no., pp.162-165 vol.1, 8-13 July 2001
- [90] Perry, B.T.; Rothwell, E.J.; Nagy, L.L.; Ross, J.E., "Self-structuring antenna concept for FM-band automotive backlight antenna design," in *Antennas and Propagation Society International Symposium, 2005 IEEE* , vol.1B, no., pp.92-95 vol. 1B, 2005
- [91] Ross, J.E.; Rothwell, E.J.; Preschutti, S., "A complementary self-structuring antenna for use in a vehicle environment," in *Antennas and Propagation Society International Symposium, 2004. IEEE* , vol.3, no., pp.2321-2324 Vol.3, 20-25 June 2004
- [92] Yumei Guo; Yingzeng Yin; Huili Zheng; Jingli Guo, "Self-structuring antenna for multi-band operation," in *Microwave, Antenna, Propagation and EMC Technologies for Wireless Communications, 2005. MAPE 2005. IEEE International Symposium on* , vol.1, no., pp.350-353 Vol. 1, 8-12 Aug. 2005
- [93] Hongtao Zhang; Yingzeng Yin; Peng Bai, "Self-structuring Antenna with Fractal Structure," in *Microwave, Antenna, Propagation and EMC Technologies for Wireless Communications, 2007 International Symposium on* , vol., no., pp.699-702, 16-17 Aug. 2007
- [94] Greetis, L.; Ouedraogo, R.; Greetis, B.; Rothwell, E.J., "A Self-Structuring Patch Antenna: Simulation and Prototype," in *Antennas and Propagation Magazine, IEEE* , vol.52, no.1, pp.114-123, Feb. 2010
- [95] Hongtao Zhang; Yingzeng Yin; Wenbo Wei, "Experimental Investigation of Wire Ring Self-Structuring Antenna," in *Microwave Conference, 2008 China-Japan Joint* , vol., no., pp.229-231, 10-12 Sept. 2008
- [96] Ozdemir, T.; Goykhman, Y.M.; Brown, A.R.; Crowgey, B.; Rothwell, E.J.; Chahal, P., "Frequency tunable antenna for LTE (4G) handsets operating in the 2.3–2.7GHz global roaming band," in *Antennas and Propagation & USNC/URSI National Radio Science Meeting, 2015 IEEE International Symposium on* , vol., no., pp.1134-1135, 19-24 July 2015
- [97] Greetis, L.; Ouedraogo, R.; Greetis, B.; Rothwell, E.J., "A Self-Structuring Patch Antenna: Simulation and Prototype," in *Antennas and Propagation Magazine, IEEE* , vol.52, no.1, pp.114-123, Feb. 2010
- [98] Coleman, C.M.; Rothwell, E.J.; Ross, J.E., "Investigation of Simulated annealing, ant-colony optimization, and genetic algorithms for self-structuring antennas," in *Antennas and Propagation, IEEE Transactions on* , vol.52, no.4, pp.1007-1014, April 2004
- [99] I Qiuyi Wu; Licheng Jiao; Xiaoying Pan; Yifei Sun, "Quantum-Inspired Immune Memory Algorithm for Self-Structuring Antenna Optimization," in *Computer Science and Software Engineering, 2008 International Conference on* , vol.6, no., pp.513-516, 12-14 Dec. 2008
- [100] M. Pannozzo, A. Forcolin Cominotto, M. Andrenacci, S. Titomanlio, S. Granelli, and D. Zamberlan, "SATURN:Smart mAritime satellite terminal for mUltimedia seRvices and conteNts", *Satellite Telecommunications (ESTEL), 2012 IEEE First AESS European Conference on*

- [101] ETSI TS 102 585 V1.1.2 (2008-04):“Digital Video Broadcasting (DVB); System Specifications for Satellite services to Handheld devices (SH) below 3 GHz”
- [102] ETSI TS 102 721-3 Satellite Earth Stations and Systems; Air Interface for S-band Mobile Interactive Multimedia (S-MIM); V1.1.1
- [103] ETSI TS 102 721-3 V1.1.1 (2011-12), “Satellite Earth Stations and Systems; Air Interface for S-band Mobile Interactive Multimedia (S-MIM); Part 3: Physical Layer Specification, Return Link Asynchronous Access”
- [104] ETSI EN 300 744 Digital Video Broadcasting (DVB); Framing structure, channel coding and modulation for digital terrestrial television V1.6.1
- [105] ETSI TR 102 377 Digital Video Broadcasting (DVB);DVB-H Implementation Guidelines V1.4.1
- [106] https://www.ettus.com/content/files/07495_Ettus_E100-110_DS_Flyer_HR.pdf
- [107] “Ship Motion and Attitude”. US DOD Interface Standard, Interface Standard for Shipboard Systems, DOD-STD-1399 (NAVY), Section 301A, 21 July 1986.
- [108] The ESR5 Criterion for the Assessment of DVB-T Transmission Quality”, ITU WP6E, Document 6E/64-E, 8. April 2004.
- [109] O. Pulvirenti; D. Ortiz, A. Del Bianco, S. Sudler, S. ;R. Hoppe, R. ; M. Pannozzo,. “Performance assessment based on field measurements of Mobile Satellite Services over hybrid networks in S-Band”, Advanced satellite multimedia systems conference (ASMS) and the 11th signal processing for space communications workshop (SPSC), 2010
- [110] ETSI TS 102 584 V 1.2 “Digital Video Broadcasting (DVB); DVB-SH Implementation Guidelines”.